Ultrafast opto-optical control of extreme ultraviolet light pulses

Bengtsson, Samuel

2017

Document Version:
Publisher's PDF, also known as Version of record

Ultrafast opto-optical control of extreme ultraviolet light pulses

SAMUEL BENGTSSON

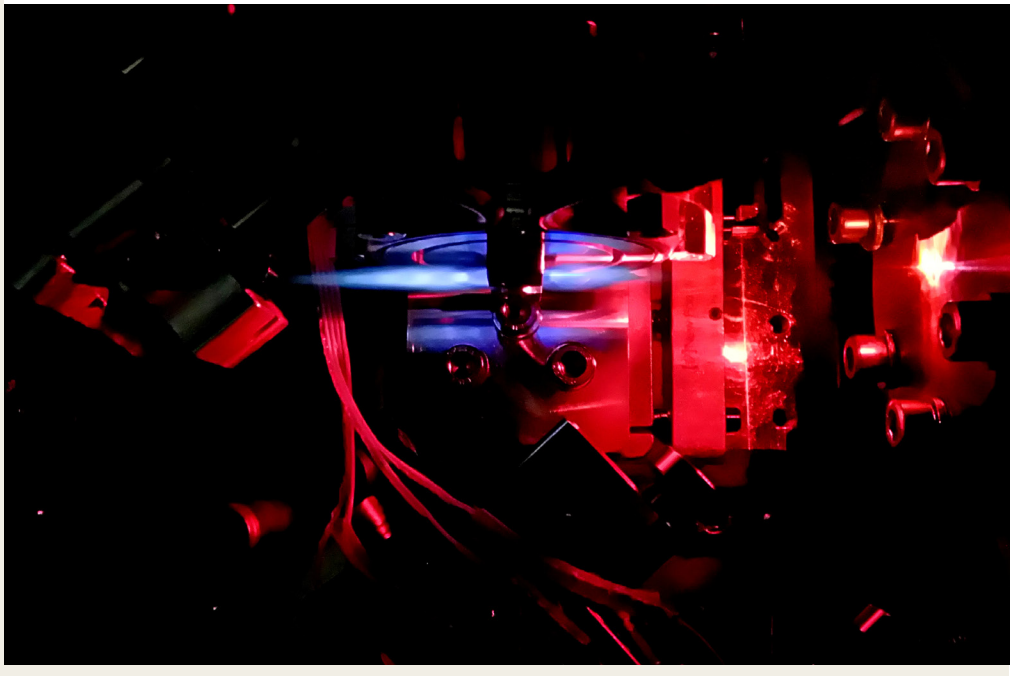

DOCTORAL DISSERTATION

Faculty of Engineering, LTH
Department of Physics
Division of Atomic Physics
Lund University

Ultrafast opto-optical control of extreme ultraviolet light pulses

Samuel Bengtsson

Doctoral Thesis
2017

Lund University

Akademisk avhandling som för avläggande av teknologie doktorsexamen vid tekniska fakulteten vid Lunds Universitet kommer att offentligen försvaras den 1 december 2017, kl 09.15 i Rydbergssalen, pä Fysiska Institutionen, Professorsgatan 1, Lund.
Fakultetsopponent: Professor Robert R. Jones, University of Virginia, USA.

Academic dissertation which, by due permission of the Faculty of Engineering at Lund University, will be publicly defended on December 1, 2017, at 09.15 a.m. in the Rydberg's hall, at the Department of Physics, Professorsgatan 1, Lund, for the degree of Doctor of Philosophy in Engineering.
Faculty opponent: Professor Robert R. Jones, University of Virginia, USA.

Ultrafast opto-optical control of extreme ultraviolet light pulses

Printed in Sweden by Media-Tryck, Lund, 2017

Division of Atomic Physics
Department of Physics
Faculty of Engineering, LTH
Lund University
P.O. Box 118
SE–221 00 Lund
Sweden

http://www.atomic.physics.lu.se

ISSN 0281-2762
Lund Reports on Atomic Physics, LRAP 540 (2017)

ISBN (print): 978-91-7753-491-4
ISBN (pdf): 978-91-7753-492-1

Soli Deo Gloria

Abstract

Extreme ultraviolet (XUV) light is a valuable frequency range for ultrafast optics experiments. The short wavelength is a requirement for ultrashort pulses, which are widely used to characterize fast dynamics. Additionally, the high photon energy enables quantum control of high frequency transitions in atoms. These transitions are of interest for ultrafast quantum control as the bandwidth of the control pulses needs to be less than the transition frequency. Presently, however, no good modulators exist for these frequencies, which significantly reduces the possible ultrafast optics experiments or applications in the XUV regime. This thesis addresses this problem and focuses on the control of XUV light in time and space.

To enable control of XUV light a method is described which modulates the phase of XUV light emitted from a gas of noble atoms. The atoms are resonantly excited with a coherent XUV pulse generated through high order harmonic generation. After the excitation pulse has passed through the gas, the atoms will emit light in the absence of an external field, known as free induction. The phase of the emitted light is changed by shifting the resonance frequencies through the AC Stark shift with a non-resonant infrared control pulse. This phase-control of the emitting atoms also translates into a control of the phase of the emitted XUV field.

With the method described in the previous paragraph, the direction of XUV light emitted from noble gases was controlled, and the temporal dynamics of the emission was studied. The redirection of the XUV emission, through the use of a spatially offset IR pulse, was found to change both with intensity of the control pulse and by changing the spatial offset between the pulses. By varying the delay between the excitation and the control pulse the time of redirection was controlled, which enabled high signal to noise study of the temporal dynamics of the emission. Furthermore, with two control pulses the emission was redirected twice, resulting in an XUV pulse shape with controlled duration emitted with a certain angle.

Hopefully the presented work will result in more research into the development of this technique, to fully realize the possibility to shape the amplitude and phase of XUV pulses. Such a development would open the door for ultrafast XUV quantum control.

Populärvetenskaplig sammanfattning

Avhandlingen som du håller i din hand handlar om att kontrollera ljus med väldigt kort våglängd, extrem-ultraviolett ljus, och att göra det ultrasnabbt. Ämnet är experimentell atomfysik, eller ultrasnabb optik för att vara ännu mer specifik. Det vi bland annat gör i det forskningsfältet, är att mäta eller kontrollera ultrasnabba processer som händer på femto (fs) (10^{-15} s)- eller ner till attosekunds-skalan (10^{-18} s).

Den första frågan när man ska börja med ultrasnabba experiment är, "Hur är det möjligt att över huvud taget mäta eller kontrollera processer som är så snabba?" Det är en mycket relevant fråga, särskilt när man försöker greppa hur snabbt det egentligen är. Under tiden som du har läst denna raden så har det passerat fler attosekunder, än mängden av sekunder sedan universums början.

Det verktyg som man använder för den här sortens experiment är korta ljuspulser. Hastigheten som ljus har i vakuum är 299 792 458 m/s, vilket i vårt universum är den högsta möjliga hastigheten så långt som vi vet. Ljus är ett eletromagnetiskt fält som svänger fram och tillbaka, och för synligt ljus är en svängning ungefär $2 \cdot 10^{-15}$ sekunder, 2 fs. Den kortaste ljuspulsen som man kan göra är en svängning av det elektriska fältet, men vi använder ungefär 10 svängningar i våra pulser. Att använda två korta ljuspulser med väldigt god kontroll över fördröjningen mellan pulserna är grundprincipen för hur ultrasnabba experiment görs.

Med synligt ljus är det möjligt att göra femtosekunds-pulser och undersöka femtosekunds-dynamik. För att göra det ännu fortare och studera attosekunds-dynamik så behöver svängningarna i det elektriska fältet för ljuset bli snabbare. Detta flyttar ljuset från synligt ljus till ultraviolett och extrem-ultraviolett (XUV) ljus.

En egenskap hos ljuset som vi använder oss av för våra experiment är att allt ljus i vår stråle, alla svängande elektriska fält, svänger i fas. Denna egenskap hos ljuset kallas för koherens. Koherent ljus har en väldefinierad riktning på ljuset och kan med optik fokuseras till mycket högre intensiteter. Skillnaden mellan okoherent ljus och koherent ljus kan man se om man jämför hur ljuset sprider sig från en glödlampa och från en laser-pekare. Att ljuset från en laser är koherent är anledningen till varför det har så många användningsområden.

Detta arbetet syftar till att öka kontrollen över koherent XUV ljus. Man kan lite grovt likna det vi gör med en analogi mellan solen och månen. Det vi gör är att kontrollera ljuset från månen, men för att vi ska få något ljus att kontrollera så

använder vi oss av en annan ljuskälla som vi inte kan styra, i detta exempel solen. I våra experiment så motsvaras månen av en gas och solen är en koherent XUV ljuskälla.

Den koherenta ljuskälla som har använts i detta arbete, bygger på generering av övertoner (High order Harmonic Generation). Kortfattat så genererar man koherent ljus med högre frekvens, snabbare svängningar, genom att fokusera ljus till hög intensitet i en gas. Svängningarna av det elektriska fältet kommer då vara så kraftiga att delar av elektroner slits ut från atomerna i gasen, för att sedan, när fältet har bytt riktning, krascha tillbaka. På liknande sätt som det kommer ut ljud med hög frekvens när man smäller till en metallstång, så kommer dessa atomer att skicka ut ljus med hög frekvens. Nackdelen är att man inte kan kontrollera riktning och amplitud av detta ljuset på något bra sätt och man får inte heller ut så mycket XUV ljus.

Med vår koherenta ljuskälla (solen, i analogin) lyser vi genom en gas (månen) som i sin tur börjar skicka ut ljus. En viktig egenskap hos atomerna i gasen vi använder är att de har resonanser med XUV strålning. En resonans som man möter i vardagslivet är när man sjunger i badrummet och plötsligt märker att rummet nästan vibrerar med en viss ton. På samma sätt börjar atomerna svänga med resonansfrekvenserna när man lyser på dem med koherent ljus. Denna svängning hos atomerna, som sker i fas, gör att de själva börjar skicka ut riktat ljus.

Hur de skickar ut ljuset kontrollerar vi genom att påverka atomerna med infrarött (IR) ljus. IR ljus har mycket lägre frekvens och det finns många bra strålkällor och mycket optik som man kan använda för detta frekvensområdet. Med hjälp av IR ljuset kan vi styra det XUV ljus som skickas ut, både i rum och tid. Att vi styr XUV ljuset i rum betyder att vi kan ändra riktningen hos ljuset och om det ska fokuseras eller spridas ut. Vi kan också kontrollera XUV ljuset i tid, så att ljuset kan skickas först i en rikning, för att efter 200 fs riktas om till en annan riktning.

Det är fortfarande långt kvar och mycket finns att göra för att bättre kunna kontrollera XUV ljus men denna avhandling är ett steg framåt. Förhoppningen är att det ska skapa nya möjligheter för ännu snabbare ultrasnabba experiment och öppna nya dörrar in till mikrokosmos. "Detta är inte slutet. Det är inte ens början på slutet. Men kanske är det slutet på början." (Winston Churchill)

List of Publications

I **Space-time control of free induction decay in the extreme ultraviolet**
S. Bengtsson*, E. W. Larsen*, D. Kroon, S. Camp, M. Miranda, C. L. Arnold, A. L'Huillier, K. J. Schafer, M. B. Gaarde, L. Rippe, and J. Mauritsson; (*Authors contributed equally).
Nat. Photon. **11**, 252-258 (2017) .

II **Noncollinear optical gating**
C. M. Heyl, S. N. Bengtsson, S. Carlström, J. Mauritsson, C. L. Arnold and A. L'Huillier.
New J. Phys. **16**, 05201 (2014) .

III **Macroscopic Effects in Noncollinear High-Order Harmonic Generation**
C. M. Heyl, P. Rudawski, F. Brizuela, S. N. Bengtsson, J. Mauritsson and A. L'Huillier.
Phys. Rev. Lett. **112**, 143902 (2014) .

IV **Gating attosecond pulses in a noncollinear geometry**
M. Louisy, C. L. Arnold, M. Miranda, E. W. Larsen, S. N. Bengtsson, D. Kroon, M. Kotur, D. Guénot, L. Rading, P. Rudawski, F. Brizuela, F. Campi, B. Kim, A. Jarnac, A. Houard, J. Mauritsson, P. Johnsson, A. L'Huillier and C. M. Heyl.
Optica **2**, 563-566 (2015).

V **Spectral phase measurement of a Fano resonance using tunable attosecond pulses**
M. Kotur, D. Guénot, Á. Jiménez-Galán, D. Kroon, E. W. Larsen, M. Louisy, S. Bengtsson, M. Miranda, J. Mauritsson, C. L. Arnold, S. E. Canton, M. Gisselbrecht, T. Carette, J. M. Dahlström, E. Lindroth, A. Maquet, L. Argenti, F. Martín and A. L'Huillier.
Nat. Commun **7**, 10566 (2016).

VI **Unexpected sensitivity of nitrogen ions superradiant emission on pump laser wavelength and duration**
Y. Liu, P. Ding, N. Ibrakovic, S. Bengtsson, S. Chen, R. Danylo, E. Simpson, E. W. Larsen, A. Houard, J. Mauritsson, A. L'Huillier, C. L. Arnold, S. Zhuang, V. Tikhonchuk and A. Mysyrowicz.
accepted in Phys. Rev. Lett. 14 September 2017.

Abbreviations

CPA	Chirped Pulse Amplification
CW	Continuous Wave
FEL	Free-Electron Laser
FID	Free Induction Decay
FWHM	Full-Width at Half-Maximum
HHG	High-order Harmonic Generation
IR	Infrared
MCP	Microchannel Plate
XUV	Extreme Ultraviolet ($10 < \hbar\omega < 120\,\mathrm{eV}$, $100 > \lambda > 10\,\mathrm{nm}$)

List of symbols

α	Polarizability
c	Speed of light in vacuum
d	Dipole moment
D	Atomic density
$\Delta\phi$	Phase change due to AC Stark shift
E	Electric field
ϵ_0	Vacuum permittivity
$g(\Delta)$	inhomogeneous line shape detuning function
Γ	Photon emission rate
h	Planck's constant
$\hbar$	Reduced Planck's constant
H	Hamiltonian
K	Wave vector
λ	Wavelength
μ	Shape dependent factor reducing superradiance
N	Number of atoms
Ω	Rabi frequency or Flopping frequency
ω	Angular frequency
p	Pressure
P	Polarization
r	Spatial position
$\hat{\sigma}$	Pauli spin matrices
t	Time
T_1	Characteristic lifetime
T_2'	Characteristic decay time from transverse homogeneous broadening
T_2^*	Characteristic decay time from inhomogeneous broadening
τ	Decay time
T_N	Characteristic decay time from superradiant process

u	Base vector of the Bloch sphere, related to "in-phase" emission
U_p	Ponderomotive energy
v	Base vector of the Bloch sphere, related to "in-quadrature" emission
V	Volume
w	Base vector of the Bloch sphere, related to the population inversion

Contents

1 Introduction **1**
- 1.1 Motivation and Objectives . . . 1
- 1.2 Publications . . . 2

2 Theory **3**
- 2.1 Historical background . . . 3
- 2.2 2-level atom . . . 4
- 2.3 Decay . . . 7
- 2.4 Macroscopic effects . . . 9
- 2.5 Propagation . . . 11
- 2.6 Superradiance . . . 12
- 2.7 Decay processes, extended . . . 15
- 2.8 AC-Stark shift . . . 15
- 2.9 Controlling the emission . . . 17

3 Methods **21**
- 3.1 The laser system used . . . 21
- 3.2 Interferometric setup . . . 23
- 3.3 Target setup . . . 26
- 3.4 XUV . . . 27
- 3.5 Target gases . . . 29
  - 3.5.1 Argon . . . 29
  - 3.5.2 Neon . . . 31
  - 3.5.3 Helium . . . 31
- 3.6 Data processing . . . 31

4 Results **35**
- 4.1 XUV spectroscopy . . . 35
  - 4.1.1 Argon . . . 36
  - 4.1.2 Neon . . . 39
  - 4.1.3 Helium . . . 43
- 4.2 Spatial control . . . 43
  - 4.2.1 Intensity . . . 44
  - 4.2.2 Lateral displacement . . . 45
- 4.3 Temporal control . . . 48
  - 4.3.1 One control pulse . . . 48
  - 4.3.2 Phase control versus four-wave mixing . . . 50
  - 4.3.3 Pressure dependence . . . 53
  - 4.3.4 Two control pulses . . . 56

5 Conclusion and Outlook **59**
- 5.1 Fundamental physics . . . 59
- 5.2 Improving Opto-Optical Modulator . . . 60
  - 5.2.1 Spatial control . . . 60
  - 5.2.2 Temporal control . . . 61

5.2.3 Full control 61
5.3 The road forward 62

Comments on the papers **63**

Acknowledgements **67**

References **73**

Papers

I	**Space-time control of free induction decay in the extreme ultraviolet**	**75**
II	**Noncollinear optical gating**	**85**
III	**Macroscopic Effects in Noncollinear High-Order Harmonic Generation**	**100**
IV	**Gating attosecond pulses in a noncollinear geometry**	**108**
V	**Spectral phase measurement of a Fano resonance using tunable attosecond pulses**	**115**
VI	**Unexpected sensitivity of nitrogen ions superradiant emission on pump laser wavelength and duration**	**123**

Chapter 1

Introduction

1.1 Motivation and Objectives

This thesis is important because it describes an essential tool for ultrafast optics, an optical modulator of extreme ultraviolet (XUV) light, which is necessary to push this field forward.

In physics, I find light-matter interaction to be the most fascinating area. Most people do not realize that light-matter interaction is something they interact with daily. We perceive the world around us mainly through this fundamental process. Furthermore, without light-matter interaction, the energy from the sun would not reach the earth and enable us to live here and so many other things would just not work.

The fact that light interacts with matter is the backbone of spectroscopy. In the early days of modern science, light from the sun was seen to be composed of many colors (Sir Isaac Newton). At the beginning of the nineteenth century, through an improvement by Fraunhofer in the tools used to see the different colors, dark absorption lines were found in the spectrum of sunlight. Later other researchers, notably Kirchhoff and Bunsen, discovered that some media emit light of the same color as they absorb. With more advanced tools, both the absorbed and the emitted spectra from different atoms and species were characterized.

All these spectra hold information about the electronic structure of the atom or molecule. Through scientists like Rydberg, Bohr and Einstein, quantum mechanics was developed and with that came the theory about the atom, which explained what information these spectra hold. All the emission and absorption lines correspond to different energy transitions that the electrons undergo in the medium. Over the years, a huge number of researchers have been devoted to measure and document the spectra and the electronic structure in a multiverse of atoms and molecules. This fundamental research has built the foundation for most of the physics, chemistry and astronomy that is pursued today.

As spectroscopy advanced to being time-resolved, temporal dynamics of electrons have been explored. This ranges from timescales of days for extremely cooled atoms in crystals, down to attoseconds for the fastest transitions. To measure fast dynamics, different types of pump-probe techniques are used, where one light pulse initiates the

process and another terminates or probes it. With short pulses and a variable delay between them, ultrafast processes in the femtosecond or attosecond regime can be measured. For the pulses to reach a duration of attoseconds, the spectral bandwidth needs to be huge and have wavelengths in the XUV. Another use of XUV in spectroscopy is to utilize the high photon energies and probe very tightly bound electrons.

Today two of the sources of coherent XUV light are high-order harmonic generation (HHG) and free electron lasers (FEL). The first is possible to fit in a room, with a high-power laser focused in a gas. This can generate high-order harmonics of the laser frequency reaching into the XUV, which results from a pulse train of sub-femtosecond-long pulses. These XUV harmonics are very difficult to shape. The way they are controlled now is through the fundamental pulse. HHG also has the drawback of low conversion efficiency, at least five orders of magnitude lower energy in the XUV pulse than in the fundamental laser pulse. The second source, FEL, requires big facilities but delivers a higher flux of XUV photons. The drawback is the control of the timing of the XUV pulses, which is inherently difficult. Today, at state-of-the-art FEL facilities, stability in delay between XUV pump and an external probe pulse can reach down to a few femtoseconds at best. To continue the ultrafast optics field, as well as control and measure electron dynamics, there is a need to better control the XUV pulses from both HHG sources and FEL sources. This thesis is a move in that direction.

1.2 Publications

The results presented in this thesis are heavily focused on the work done and published in Nature Photonics (paper I). This topic and following experiments was the aim and main focus in my PhD. In addition to this paper, other papers describe research performed with the setup detailed in the methods section (papers IV - VI). Two of the papers include theoretical Strong Field Approximation (SFA) calculations, which I performed during my first year, but is not further commented on in this thesis (papers II,III).

Chapter 2

Theory

The work leading up to this thesis uses ultra-short laser pulses in the extreme ultraviolet (XUV) spectrum and sends them through a gas of noble atoms. These XUV pulses excite an ensemble of atoms, which cause them to emit XUV light after the excitation process. The properties of this emission are controlled by an ultra-short infrared (IR) pulse. To discuss and better understand the process and the results of such coherent collective emission, this chapter will briefly review the theoretical background to the thesis.

2.1 Historical background

In the introduction to his paper about "Nuclear induction" [6], Bloch refers to two experiments performed on magnetic resonances, Gorter and Broer, [17] and Purcell with collaborators [30]. Both experiments used weak radio frequency (r-f) fields to try to detect magnetic resonance. Bloch commented that the experiments by him and his colleagues "differ rather essentially" from the others, in that they used strong r-f fields to effect change in the nuclear moments. The precession of the nuclear momentum in the field induces an electromotive force in a coil, and the voltage can be measured. What Bloch and his collaborators do in the experiment is generate forced rotation of the nuclear moment by the external field, but Bloch ends his introduction by pointing out that with a short, strong r-f pulse, a nuclear-induced field after the external pulse has passed should be quantifiable, which would then measure the free nuclear precession. This experiment was performed some years later by Erwind Hahn and the decay of this signal was measured [19].

In 1972, Brewer and Shoemaker were the first to measure free induction decay in the optical regime [7]. Their experiment used the signal from a Doppler-broadened IR transition of NH_2D. With a sudden Stark shift of the states, they were able to move the states out of resonance and measure the "free" emission. The results of this paper were further commented on by Hopf, Shea and Scully in the same volume from a theoretical point-of-view [22].

Just some years after Bloch and Hahn's seminal papers, Dicke published a theoretical paper about the coherent spontaneous emission from a group of atoms, commenting

that one cannot ignore the effect other emitting atoms have in the neighborhood of an atom [14]. He concluded that through the interaction, the individual atoms would decay faster, with a maximum decay proportional to N^2. During the 70s and 80s, much theoretical research was conducted on this topic, the coherence of a macroscopic spontaneous emission.

In a book "Two level atoms and optical resonances" by L. Allen and E.H Eberly [2], the writings of different authors are joined together to form a theoretical framework. Following is a brief review of emission from atoms and ensembles of atoms, mostly based on their work, in a way that is useful or provides insight into this thesis.

2.2 2-level atom

Simplified models are often a very useful tool for gaining insight and understanding about complicated processes. When it comes to light-atom interaction, the two-level atom is a simple model that has been used to a great extent and with much success. The two-level atom has a ground state and an excited state. They can physically represent either two different spin or electronic states. The atom can either be in the ground state, the excited state or a superposition of the two states. One set of equations that describe such a system and how it interacts with light are the Bloch equations. I will briefly discuss where these equations come from.

The Hamiltonian of a two-level system interacting with an electric field can be written [2]

$$\hat{H} = \hat{H}_0 - \hat{\mathbf{d}} \cdot \hat{\mathbf{E}}(\mathbf{r}_0), \tag{2.1}$$

where H_0 denotes the Hamiltonian without any external fields and the second term is the interaction between the atom and an electrical field, where $\hat{d}$ is the dipole operator and $\hat{E}$ is the electrical field operator.

If eq. 2.1 is evaluated in a general case for a two-level atom with one ground state and one excited state, then the energy of that system, the expectation value for the Hamiltonian, is given by

$$\langle \Phi | \hat{H} | \Phi \rangle = \begin{bmatrix} E_g & 0 \\ 0 & E_e \end{bmatrix} - \begin{bmatrix} 0 & \langle g | \hat{\mathbf{d}}\hat{\mathbf{E}} | e \rangle \\ \langle e | \hat{\mathbf{d}}\hat{\mathbf{E}} | g \rangle & 0 \end{bmatrix} \tag{2.2}$$

with

$$|\Phi\rangle = \begin{bmatrix} |g\rangle \\ |e\rangle \end{bmatrix}. \tag{2.3}$$

Here in eq. 2.2, the diagonal terms, E_g and E_e, are the energy of the eigenstates, $\langle g|$ and $\langle e|$, of the system. The off-diagonal matrix elements are in general complex, so

$$\mathbf{d}_{ge} = \langle g | \hat{\mathbf{d}} | e \rangle, \tag{2.4}$$

can be expressed as $\mathbf{d}_{ge} = \mathbf{d}_r + i\mathbf{d}_i$ and $\mathbf{d}_{eg} = \mathbf{d}_r - i\mathbf{d}_i$. Using Pauli spin matrices

$$\hat{\sigma}_1 = \begin{bmatrix} 0 & 1 \\ 1 & 0 \end{bmatrix} \quad \hat{\sigma}_2 = \begin{bmatrix} 0 & -i \\ i & 0 \end{bmatrix} \quad \hat{\sigma}_3 = \begin{bmatrix} 1 & 0 \\ 0 & -1 \end{bmatrix}, \tag{2.5}$$

eq. 2.1 for the basis $|g\rangle$ and $|e\rangle$ can then be written as

$$\hat{H} = \frac{1}{2}(E_g + E_e)\hat{I} + \frac{1}{2}(E_g - E_e)\hat{\sigma}_3 - (\mathbf{d}_r \cdot \hat{\mathbf{E}})\hat{\sigma}_1 + (\mathbf{d}_i \cdot \hat{\mathbf{E}})\hat{\sigma}_2, \tag{2.6}$$

with $\hat{I}$ being the unit operator. We are here using the so called Heisenberg picture with time dependent operators and stationary states. To express interaction between the two-level atom and a field, the temporal dynamics of the energy are needed. The time evolution of an operator where the time dependence is not explicitly implied (as it is for the electric field) is [2]

$$i\hbar\dot{\hat{O}} = [\hat{O}, \hat{H}]. \tag{2.7}$$

From this the time evolution of the Pauli matrices follows from eq. 2.6 [2]

$$\dot{\hat{\sigma}}_1 = -\omega_0\hat{\sigma}_2(t) + \frac{2}{\hbar}[\mathbf{d}_i \cdot \hat{\mathbf{E}}(t)]\hat{\sigma}_3(t), \tag{2.8a}$$

$$\dot{\hat{\sigma}}_2 = \omega_0\hat{\sigma}_1(t) + \frac{2}{\hbar}[\mathbf{d}_r \cdot \hat{\mathbf{E}}(t)]\hat{\sigma}_3(t), \tag{2.8b}$$

$$\dot{\hat{\sigma}}_3 = -\frac{2}{\hbar}[\mathbf{d}_r \cdot \hat{\mathbf{E}}(t)]\hat{\sigma}_2(t) - \frac{2}{\hbar}[\mathbf{d}_i \cdot \hat{\mathbf{E}}(t)]\hat{\sigma}_1(t), \tag{2.8c}$$

where

$$\omega_0 \equiv \frac{E_e - E_g}{\hbar}, \tag{2.9}$$

is the angular frequency between the two states of the atom. In a semi-classical approach, the quantum correlations between the electric field and the atom are set to be negligible. This assumption means that the evaluation of a product between an operator for the field, $\hat{E}$, and the atom, e.g. $\hat{\sigma}_3$, is equal to the product of their expectation values,

$$\langle\hat{E}(t)\hat{\sigma}_3\rangle = \langle\hat{E}(t)\rangle\langle\hat{\sigma}_3\rangle. \tag{2.10}$$

This can not be used, for example, to explain spontaneous emission, as that requires the atom to couple to the vacuum field, but is useful to describe many other interactions between the field and the atom.

Applying a semi-classical approach (eq. 2.10) on eq. 2.8 a pseudo-spinvector $s(t) = \langle\sigma\rangle$ can then be define to be

$$\dot{s}_1(t) = -\omega_0 s_2(t) + \frac{2}{\hbar}[\mathbf{d}_i\mathbf{E}(t, r_0)]s_3(t), \tag{2.11a}$$

$$\dot{s}_2(t) = \omega_0 s_1(t) + \frac{2}{\hbar}[\mathbf{d}_r\mathbf{E}(t, r_0)]s_3(t), \tag{2.11b}$$

$$\dot{s}_3(t) = -\frac{2}{\hbar}[\mathbf{d}_r\mathbf{E}(t, r_0)]s_2(t) - \frac{2}{\hbar}[\mathbf{d}_i\mathbf{E}(t, r_0)]s_1(t). \tag{2.11c}$$

For the three vectors, the conservation laws give the condition [2] $s_1^2 + s_2^2 + s_3^2 = 1$. This $s(t)$ vector will in the absence of an external field rotate around the s_3 vector

with the frequency ω_0. Further on, an external field will cause the vector to rotate around s_1 and/or s_2.

A more common way than using eq. 2.11 is to apply the rotating frame approximation. The electrical field with the faster oscillations separated can be written as

$$E(t) = E_0(t)(e^{i\omega t} + e^{-i\omega t}), \tag{2.12}$$

with ω being the center frequency of the field and describing the electrical field parallel to d_r and d_i. Assuming that the frequency of the applied electrical field is close to resonant with the transition, $\omega_0 \approx \omega$ the fast oscillations can be neglected with a change of frame. This means, instead of the fast oscillations ω_0 around the s_3 vector, the frame starts spinning with ω. The frequency of the new state vector, $\rho = (u, v, w)$, in the absence of an external field is then $\Delta = \omega_0 - \omega$. When performing this approximation, the second term in eq. 2.12 will instead of being slower become twice as fast and the interference on the system vector will integrate to zero. Let us further define a Rabi frequency for the interaction between the atom at the field and split it in a real and imaginary part [21],

$$\frac{2(d_r + id_i)E_0}{\hbar} = \Omega_r + i\Omega_i. \tag{2.13}$$

The Bloch equations, as they are called, then become

$$\dot{u} = -\Delta v + \Omega_i w, \tag{2.14a}$$
$$\dot{v} = +\Delta u + \Omega_r w, \tag{2.14b}$$
$$\dot{w} = -\Omega_r v - \Omega_i u. \tag{2.14c}$$

With the Bloch vector, ρ, this can also be seen as the cross product

$$\frac{d}{dt}\rho = \mathbf{\Omega} \times \rho, \tag{2.15}$$

where

$$\mathbf{\Omega} \equiv (-\Omega_r, \Omega_i, \Delta). \tag{2.16}$$

In eq. 2.15 is more explicit how the rotation of the Bloch vector, ρ, is caused by the cross product with the vector $\mathbf{\Omega}$, which depends on the detuning Δ and the interaction between the atom and the external field. The Bloch vector with a length equal to one is thus a graphical representation of the two-level atom and describes the quantum system, while the $\mathbf{\Omega}$ vector describes the external light field.

The local polarization density of the single atom is described by u and v as,

$$P(t) \propto [u\cos(\omega t + \phi_u) - v\sin(\omega t + \phi_v)], \tag{2.17}$$

where ϕ_u and ϕ_v are phases. These two terms are sometimes called the "in-phase" and the "in-quadrature" component of the polarization with respect to the driving electrical field, which is more clearly seen when the electrical field is expressed as a cosine.

2.3 Decay

For a two-level atom described by eq. 2.14, one difference from real atoms is the inability to stop and relax. If the two level-atom above is put in a superposition of the ground and excited state ($w \neq \pm 1$) the system in a stationary frame will oscillate forever and the phase of the states will always be known. In the spectral domain, this corresponds to a fully defined frequency, a delta spike.[1]

For real atoms and transitions, that is not the case. For electronic transitions, the relaxation process back to the ground state can range from days [23], in the extreme case, down to femtoseconds [5]. In this relaxation process, energy is emitted from the atom, and for atoms in a gas, this is often through radiation. For a single atom, in a full quantum description, that means emission of a photon. In the absence of external changes the probability for the atom to relax and send out a photon is constant[2]. Equation 2.14c can then be modified to

$$\dot{\hat{w}} = -\frac{w+1}{T_1} - \Omega_r v - \Omega_i u. \tag{2.18}$$

If the equilibrium point is shifted, due to different incoherent sources, the numerator in the first term is changed to $w - w_{eq}$, where w_{eq} is the equilibrium value in the system.

The extra term proportional to w gives an exponential decay in the form of e^{-t/T_1} to the energy in the system, $w(t)$. The characteristic decay parameter T_1 thus relates to the relaxation of the atom down to the ground state. Semiclassically, the relaxing atom emitts a dampening electric field originating from the atom. In a fully quantum view, rather, a dampening probability field describing the location of the photon is emitted. This is what is called fluorescence and does not have a specific direction of emission.

With the introduction of termination or decay of the signal, the signal is no longer a mono-frequency but acquires a spectral width. Fourier transforming a exponential decaying emission signal gives a Lorentzian line shape, as is expected and observed from atomic spectroscopy. In a cloud or ensemble of multiple atoms of the same kind, all of them will have the same homogeneous broadening of the frequency. This broadening of the transition frequency due to loss of energy is called longitudinal homogeneous broadening[2].

Another decay effect, or group of effects, is called transverse homogeneous broadening and is a decay of the known phase. In principle, the change in w as it decays from 1 represents an increase of uncertainty. This reaches a maximum as $w = 0$ when position of the electron is the most unknown, whether it is in the ground or excited state. The same can happen for the phase, or coherence, between the states, which is governed by u and v. Such homogeneous effects, where the probability is the same for all atoms to suddenly make a phase jump, can be collisions with other atom in a gas or spin-flips in a solid. This increase in the uncertainty about the phase is expressed

[1] This is what is wanted for an atomic clock, an atomic transition with an extremely narrow frequency width.

[2] similar as the probability to throw a 1 on a die is constant.

by a time T_2' and eq. 2.14 can then be modified to

$$\dot{u} = -\frac{u}{T_2'} - \Delta v + \Omega_i w, \tag{2.19a}$$

$$\dot{v} = -\frac{v}{T_2'} + \Delta u + \Omega_r w, \tag{2.19b}$$

$$\dot{w} = -\frac{w+1}{T_1} - \Omega_r v - \Omega_i u. \tag{2.19c}$$

One might ask why this loss of knowledge about the phase yields a decay of the signal. The answer is interference between the signal from many atoms. As the phase of the different atoms are randomly shifted, due to collision or some other event, the result after some time is a statistical mix of all phases. Described with the Bloch vectors, those that at one time were pointing in the same direction, jump to different phases, and thus different directions in the u-v plane. The resulting Bloch vector for the system then becomes shorter than one, and with an even spread of the phases, the vector is $\rho_{sum} = (0, 0, w)$. Even with energy left in the system, nothing will be emitted as the macroscopic polarization of the medium is zero.

As opposed to homogeneous broadening, where the phase-changing events have equal probability to happen for all atoms, the inhomogeneous broadening comes from differences between the various atoms in an ensemble. These differences result in non-identical resonance frequencies for the various atoms, ω_{in}, where the change from the central frequency is $\omega_0 - \omega_{in}$. If all atoms are equally excited, with time the phases will evolve differently, and the atoms drift out of phase with each other due to their different transition frequencies. Described with the Bloch vectors for the atoms, the various frequencies cause the vectors to move with different speeds around the w vector and thus spread out over time. Similar to the transverse homogeneous broadening, this causes a decay in the emitted signal. The difference is that no random event has happened to the individual atoms, which still have $w \neq -1$.

It is then possible to rephase the atoms and get them to send out signals again in what is called an echo [20]. By applying a π pulse a time t_{flip} after initiation, rotating the Bloch vectors π rad around either u or v for all atoms, the different transition frequencies of the atoms will cause the Bloch vectors to gather again. After a second time t_{flip} the vectors will again be in phase and thus the system will emit light, an echo of the first pulse.

The characteristic decay time of the inhomogeneous broadening effects is defined as T_2^*. This decay is what is referred to as free induction decay (FID) [20].

The cause of the inhomogeneous broadening for gas is typically Doppler shift, where the various atoms move with dissimilar velocities in different directions and thus acquire separate frequency shifts, with a Gaussian distribution. For gases at room temperature, the thermal Doppler broadening results in a T_2^* on the order of 100 ps.

The better description of the polarization of a one-dimensional ensemble is a mod-

ification to eq. 2.17, including multiple atoms and a line width,[3] [2]

$$P(t,z) = Dd \int g(\Delta')[u\cos(\omega t - Kz) - v\sin(\omega t - Kz)]d\Delta', \tag{2.20}$$

where D is the atomic density, d is the transition dipole moment, and $g(\Delta')$ is the inhomogeneous line shape detuning function. Thus $g(\Delta)d\Delta$ yields the fraction of dipoles with the center frequency shifted by Δ. The function thus obeys $\int g(\Delta')d\Delta' = 1$ as that would be all atoms.

2.4 Macroscopic effects

One major omission in the discussion so far is the neglect of macroscopic effects. Indeed, all interference has been described as if the atoms were positioned at the same spot. The interference of the emitted fields from atoms spread out in space is studied in this section.

To permit some phenomenological understanding about the directional shape of the emission from an ensemble, let us construct a simple model with a two-dimensional plane or surface[4]. Dipoles, or excited two-level atoms, can then be placed in this surface-model to study the interference between the emitted electrical fields for different starting phases on the emitters. This model has multiple flaws but is still useful for understanding interference effects and the direction of emission. For the l^{th} atom, the emitted electric field can be expressed as

$$E(\mathbf{r} - \mathbf{r}_l, t - t_l) = E_0 e^{i\mathbf{K}(\mathbf{r}-\mathbf{r}_l)+\omega(t-t_l))}, \tag{2.21}$$

where $\mathbf{r}_l$ denotes the position of the atom and t_l denotes when it is excited. $\mathbf{K}$ can be split in a unit vector times a value, and since the unit vector is parallel with the vector $\mathbf{r} - \mathbf{r}_l$, the value $K = 2\pi/\lambda$ can be used instead of $\mathbf{K}$.

Eq. 2.21 describes the isotropic emitted field from one atom on the surface[5], and the real part of this field exhibits similarities with the field created by the polarization described by eq. 2.17 for one atom.

To include macroscopic effects, more atoms that are at different positions on the surface are added. If we just study the interference between the different atoms with the same resonance frequency and assume no decay, the temporal variation of the field can be ignored and only the starting phase and position of the emitters are of importance. The total electrical field is then

$$E_{tot}(\mathbf{r}) = \sum_l E(\mathbf{r} - \mathbf{r}_l, \phi_l), \tag{2.22}$$

where now ϕ_l is the phase for the l^{th} atom. For the distribution of the atoms or ensemble that emit, a random position in a Gaussian distribution is used, creating a circular area with atoms on the surface to be studied. In the following results,

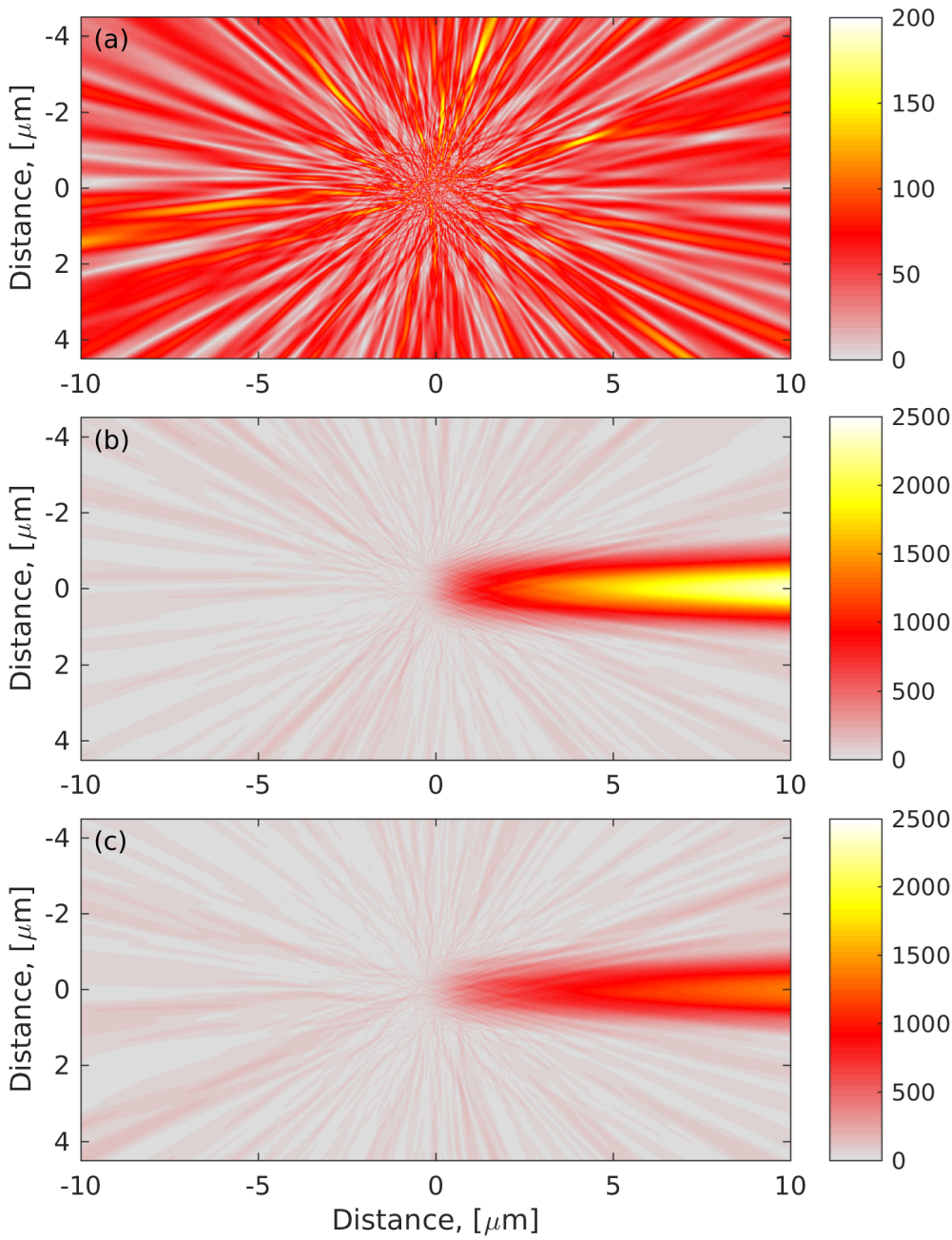

Figure 2.1: Result from a 2D surface-model. The absolute value of the electrical field from 3,500 atoms positioned on a surface within a Gaussian distribution with $\sigma = 0.5\mu$m (a) Random phase on the emitters gives a great deal of interference with similar emission in all directions. (b) A space-dependent phase on the emitters that is equal to $-Kz$, which results in a beam. Notice the changed color scale. (c) The same z-dependent phase as in (b) but with an added Gaussian-distributed random phase with $\sigma = \pi/3$ resulting in a reduction of the beam intensity.

a standard deviation of 0.5 μm was used for the spatial distribution on the surface, together with 3,500 atoms[6].

In fig. 2.1 (a) $|E_{tot}|$ is shown, calculated with ϕ_l uniformly distributed between 0 and 2π and the atomic ensemble centered at (0,0). The interference of the electrical fields can be clearly seen. This interference gives rise to a mosaic inside the ensemble and emerging rays of constructive interference. With an increasing number of atoms, broadening effects and a bigger ensemble, the ray structure is expected to turn into a more homogeneous field sent in all directions on the surface, as expected in the real world of emission from a gas without any coherence.

In fig. 2.1 (b) a phase is given to the atoms with $\phi_l = -Kr_z$ where r_z is the projection of $\mathbf{r}_l$ on the z-axis. This corresponds to the case of a pulse traveling through the ensemble in a positive z direction and exciting the atoms as it passes[7]. The coherence in the system result in a well-defined beam with an intensity proportional to N^2.

The various decaying processes will affect this emission differently. First, T_1, the decay of the inversion kills all emission from the atoms. Furthermore, T_2' and T_2^*, the decays affecting the coherence will move the emission from fig 2.1 (b) to (a). A middle step is calculated in fig 2.1 (c), where the phase added to the atoms are $\phi_l = -Kr_z + \alpha$, where α comes from a Gaussian distribution with standard deviation $\pi/3$. This adds a decaying part to the coherence of the atoms. The beam is reduced in amplitude as the coherence is reduced, without becoming more divergent. As the coherence between the atoms in an ensemble decays, the coherent emitted beam is then expected to slowly fade.

2.5 Propagation

In the previous section, the fields emitted from the atoms were not interacting with other atoms in any way. One way to incorporate that into calculations is by using the relationship between electrical fields and polarization from Maxwell's equations, together with the polarization of the atoms from Bloch equations. If the polarization density is oscillating in phase across the focus emitting plane wave fronts, one-dimensional expressions can be used[2].

$$\left[\frac{\partial^2}{\partial z^2} - \frac{1}{c^2}\frac{\partial^2}{\partial t^2}\right] E(t,z) = \frac{4\pi}{c^2}\frac{\partial^2}{\partial t^2} P(t,z), \tag{2.24}$$

[3]Here given for one dimension assuming excitation by an electrical field traveling in z direction. This gives a space-dependent phase in the polarization, Kz

[4]Imagine a water surface.

[5]Like the rings on the surface of the water created by a thrown pebble

[6]This corresponds roughly to the number of atoms from a density for 1 mbar, room temperature gas calculated from the ideal gas law

$$\frac{pN_A}{RT} = \mathrm{D}, \tag{2.23}$$

with p being the pressure in pascal, N_A, the Avogadoro constant, R, the ideal gas constant, T, the absolute temperature, and D, density in atoms/m^3 and a volume of $(2 \cdot 10^{-6})^2 \cdot 3.3 \cdot 10^{-8}$ m^3

[7]Worth noting is the difference in color scale between fig. 2.1 (a) and (b), as well as the fact that the plotted is the electrical field and not the intensity, which would increase the difference much more.

with

$$P(t,z) = Dd \int g(\Delta')[u\cos(\omega t - Kz) - v\sin(\omega t - Kz)]d\Delta', \tag{2.25}$$

and

$$E(t,z) = E_0(t,z)e^{i(\omega t - Kz)}. \tag{2.26}$$

Here D is the atomic density, d is the atomic transition dipole moment, $g(\Delta')$ is the inhomogeneous line shape detuning function, ω is the transition angular frequency and K is the wave vector. Assuming slow changes to $E_0(t,z)$ compared to the light field dynamics [3] this can be expressed as [27]

$$\frac{\partial E_0(t,z)}{\partial z} + \frac{n}{c}\frac{\partial E_0(t,z)}{\partial t} = \frac{-2\pi\omega}{nc}\int g(\Delta')v(t,z,\Delta')d\Delta', \tag{2.27}$$

where n is the index of refraction and E_0 is real. This is for the real part of the field and there is a similar expression for the imaginary part (with u instead of v).

Using eq. 2.27 the field can be propagated semi-classically through the gas, as no quantum correlation is yet included between the atoms and the field. This can be used for calculating electro-induced transparency [27] or how increased atomic density speeds up decay of the emission from an absorption resonance.

2.6 Superradiance

One case of emission from an ensemble of atoms that does require quantum correlations between the atoms and the field, is superradiance, as Dicke called it for lack of a better word [14]. This effect is of interest, even though the starting point of the effect is not the same as for the experiments performed in this thesis.

Quantum electrodynamics are needed if the atomic ensemble starts with total inversion, that is everything is in the excited state. This is possible to reach, for example with a three-level configuration, where the population is pumped from the ground state to an excited state, and the emission studied comes from a transition down to another state. To model the spontaneous emission that will start the process, the atomic state needs to couple to the vacuum fields. The assumption with eq. 2.10 is then no longer valid. A large number of papers have been written about this problem and many models and approaches have been used. In an essay by M. Gross and S. Haroche [18] different models and approaches from various authors are put together showing all the depths and subtleties there are to the effect. I will try to briefly cover the essence of superradiance.

For an ensemble of fully excited atoms, $w = 1$, within a wavelength's distance from each other, spontaneous emission happens through coupling to the vacuum states of the electrical field. This coupling is purely quantum mechanical with a probability distribution for when a spontaneous emission will happen, as well as random direction. The rate for the first photon to be emitted from the ensemble can be expressed as

$$\Gamma_{first} = \Gamma N, \tag{2.28}$$

where $\Gamma = \hbar/T_1$ is the photon emission rate for a single atom and N is the number of atoms.[8] This is the same as for non-interacting atoms. As the states of the electrical

[8] The same as when 10 persons are throwing 2 apples per minute, the total rate is $2 \cdot 10 = 20$ apples per minute.

field are populated, or photons are sent out from the atoms, the coherence between the atoms will build up. This can be expected due to the atoms being closer to each other than the wavelength of the photon. Thus, the individual atoms become entangled, as it is not possible to say which atom the photon came from.

With a laser beam traveling through a gas cloud, it is fair to assume a pencil-shaped ensemble of excited atoms. In the beginning, small clusters of entangled atoms with a common random phase direction form. As time goes on and more photons are sent out, different regions will couple with each other and create bigger ones with a common wave direction. Two criteria are crucial for the pencil shape. First, the size of the pencil need to be less than $c\tau_N$, where τ_N is the typical coherence time in the system and c is the speed of light in vacuum[9]. Second, the width of the pencil-shaped atomic ensemble needs to be much less than the length. When those two criteria are met, photons traveling in the pencil direction couple different regions and create larger ones, while those with a photon wave direction orthogonal to the pencil do not grow. Finally, the bigger regions swallow the smaller ones and the whole medium becomes one big region emitting along the pencil shape. If the shape is larger than the above criteria, photons are not able to couple the different parts of the ensemble, as the coherence has already been lost before a photon can travel from one end to the other.

A main aspect of superradiance is an increased photon emission rate for the coupled system. To obtain an expression for the photon emission rate from the system, it is possible to start instead with the rate for photons emitted into the electrical field modes. If only spontaneous emission from the ensemble of atoms is studied, only the vacuum modes are populated. Summing up the expectations for photons for all frequencies, polarizations and directions and how they change with time yield the rate of photon emission from the ensemble. This is done in ref. [2] to obtain a rate for the energy emitted from the ensemble, which is[10]

$$-\frac{d}{dt}W_N(t) = (\frac{\mu}{T_1})(\frac{N}{2}+W_N)(\frac{N}{2}-W_N+\frac{1}{\mu}). \tag{2.29}$$

Here W_N is the dimensionless energy in the system that goes from N/2 when all atoms are in the excited state, to -N/2 when they are all in the ground state. N is the number of atoms in the ensemble. T_1 is the natural lifetime of the transition. μ is a factor that depends on the shape of the ensemble. It reduces the rate of useful spontaneous photon emission. For a pencil-shaped structure, it is

$$\mu = \frac{3\lambda^2}{8\pi A}, \qquad A \gg (\frac{\lambda}{2\pi})^2, \qquad L < \frac{A}{\lambda}, \tag{2.30}$$

where A is the cross-sectional area and L is the length of the pencil shape. The physical interpretation is that not all photons emitted build up a coupled system, only the ones emitted along the pencil shape actually support the build-up of the coupling between the atoms.

In eq. 2.29 for large N values, the photon emission rate goes from being linear with N for $W_N = N/2$, to proportional to N^2 for $W_N = 0$. This means that as the

[9] It would be more correct to add the index of refraction for the media as well, however, for gases the change is minute

[10] compare with ref. [14] eq. 24. Corrections to this equation can be expected to be on the order of 1/N according to the authors.

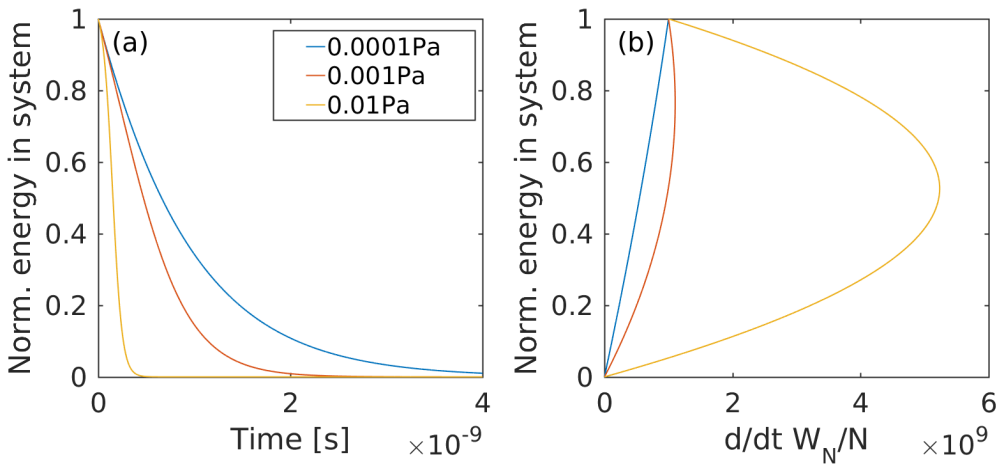

Figure 2.2: Rates and time evolution of eq. 2.29 for different pressures for a pencil-shaped ensemble with a radius of 30 μm and a length of 1 cm. (a) shows the decay of the normalized energy for a, in the beginning, non-coherent system with a natural lifetime of 1 ns for different pressures (b) shows the corresponding rate of photon emission from eq. 2.29 divided by the number of atoms, N, in the system. For low pressure and small number of atoms, the rate is linear, but with increased pressure the photon emission rate increases as the energy in the system is emitted.

system is coupled together, the photon emission rate from the atoms increases. The characteristic decay time for this process is [2]

$$T_N = \frac{T_1}{N\mu + 1}. \tag{2.31}$$

To put this in perspective, a pencil-shaped atomic ensemble with a radius of 30 μm and a length of 1 cm for a wavelength of 80 nm and a decay time of 1 ns meets the criteria in eq. 2.30 for the size. It is possible to obtain estimate of the number of atoms for a certain pressure with the ideal gas law

$$pV = n_{mol}RT, \tag{2.32}$$

and

$$n_{mol} = NN_A, \tag{2.33}$$

where p is pressure in Pa, V is volume in m^3, N is the number of atoms, N_A is the Avogadro constant, R is the gas constant, and T is the temperature in K. Using room temperature and the above values for the pencil volume together with a pressure of 0.0001, 0.001 and 0.01 Pa (100 Pa is equal to 1 mbar), result in $N = 7 \cdot 10^5$, $7 \cdot 10^6$, and $7 \cdot 10^7$ respectively.

In fig. 2.2 eq. 2.29 is calculated for a transition with a natural lifetime $T_1 = 1$ ns. The rates are then used to calculate the decay of the systems. The first feature to notice is the difference between 0.0001 Pa and the rest. The rate is linear as would be expected if the atoms are not interacting. If half of the atoms have sent out a photon such that the energy in the system is halved the photon emission rate is also halved. The decay curve, fig. 2.2 (a) for 0.0001 Pa, is also a nice exponential, similar to the

decay of a single atom. As the pressure is increased, the shape of the rates changes and for 0.01 Pa the photon emission rate, when half of the atoms have sent out a photon, is 5 times the initial rate. This is seen in the decay curve as a faster decay and a more S-shaped decay. In the model (eq. 2.29), the condition for the ensemble to form one region and become superradiant is $N\mu \gg 1$. This means that many atoms emit photons in the right direction along the pencil, which couples atoms together and forms a big region.

The limitations of the model are obvious, as the requirement that the whole ensemble is coupled, gives a time L/c limit for the dynamics, which for the example stated above is 30 ps. For faster decays, the pencil-shaped ensemble is split in different sectors which do not have time to form one big phase matched section.

2.7 Decay processes, extended

For the "pure" superradiance case described in previous section, the ensemble is prepared in a way of noncoherence to start with. If instead a weak external resonant pulse is used, an excitation pulse, all the atoms in the ensemble will be phase matched to start with. In that case the first step of the "pure" superradiance, the quantum spontaneous emission step, where the atoms start interacting with the vacuum field and obtain a random phase, is not relevant. Instead, we start with some energy in the system, which is neither zero nor full, and with a fully formed coherent ensemble.

For this ensemble, a superradiant process can be imagined that increases the photon emission rate and gives a shorter decay time in the signal than other decay processes. From eq. 2.31 the parameter μ is set by the densities where the emission starts to express superradiant behavior and the equation shows the gradual transition to shorter lifetimes. For ultra-short lifetimes, such as for auto-ionizing states, or when T_N becomes very small, the N is no longer the whole possible ensemble. The atoms are expected to have decayed a distance on the order of $c\tau$ after the pulse, where τ is the decay time. Since the increase in the photon emission rate comes from coupled atoms, the coupled atoms, N, cannot come from a region larger than that distance, $c\tau$. This effectively reduces the ensemble. For a decay time of 100 fs this length is on the order of 10 μm.

In general, we conclude that the decay process can be very fast. How fast it is depends on the gas density or the number of atoms coupled to each other, which experimentally could in principle be multiple smaller regions from a large ensemble.

2.8 AC-Stark shift

Another light-matter interaction effect by an external light pulse is the change of the resonance frequencies of an atom,

$$\omega(E_0) = \omega_0 + \delta\omega(E_0). \tag{2.34}$$

This change or shift, $\delta\omega(E_0)$, is called Stark shift and can be caused with both a static electric field and a dynamic electric field. These are referred to more commonly as DC Stark shift and AC Stark shift. The energy in the atom (or electron) is shifted due to interaction between the dipole moment and the non-resonant field (compare

the second term in eq. 2.1). With a constant dipole moment, the shift in frequency due to a DC field is given by [13]

$$\delta\omega_{nn_1m} = -\frac{d_{nn_1m}E_0}{\hbar}. \tag{2.35}$$

Here E_0 is the strength of the electrical field and d_{nn_1m} is the constant dipole moment that depends on the quantum numbers n,n_1, and m[11]. Even if the atom has zero constant dipole momentum, a dipole momentum can be induced by the electrical field

$$d_{nlm} = \alpha_{nlm}E_0, \tag{2.36}$$

where α_{nlm} is the polarizability of the atom state with corresponding quantum numbers. Thus, the shift in frequency can be expressed as [13]

$$\delta\omega = -\frac{d_{nn_1m}E_0}{\hbar} - \frac{\alpha_{nlm}E_0^2}{2\hbar}, \tag{2.37}$$

with the first term being the linear DC Stark shift, and the second term being the quadratic DC Stark shift. In general, for atoms with a constant dipole moment, the value changes proportionally to the quantum number n^2, while the polarizability changes as n^6 [13]. This is a highly simplified picture and more needs to be taken into account for the individual states, but for noble atoms, the constant dipole moment can be neglected; thus, the frequency shift is proportional to the intensity of the static field.

If instead of a static field, a dynamic electrical field, for example from a laser, is used, some part changes while much stay the same. From a practical point-of-view, it is possible to achieve much higher field strengths when focusing the beam. With the AC Stark field, it is also possible for multiphoton processes to happen when sending through a light pulse. Sometimes this AC Stark shifting field, together with the atom, is referred to as a "dressed-atom"[9]. As for the shifting of the resonance frequencies, it reduces to [13]

$$\delta\omega = -\frac{1}{4}\frac{\alpha E_0^2}{\hbar}. \tag{2.38}$$

Of interest for this thesis is the case of a noble atom and a transition between ground state and a higher state, which is embedded in many neighboring states. For an IR pulse, the ground state is not expected to shift much[12]. Furthermore, if the excited state is close to the ionization energy, polarizability comes close to the free electron in the field, and the frequency shift becomes

$$\delta\omega = \frac{U_p}{\hbar}, \tag{2.39}$$

with U_p being the ponderomotive energy.

In the case of the IR field being both low frequency (compared to the nearest transitions for the ground state) and high frequency (compared to the excited state and the neighboring states), the atom will respond to the "instantaneous" AC field[13]. The instantaneous resonance frequency for that transition can then be expressed as

$$\omega_{res}(t) = \omega_0 + \delta\omega(t), \tag{2.40}$$

[11] n_1 is the parabolic quantum number characterizing the split sublevel

[12] for more details, see [13] section 4.3

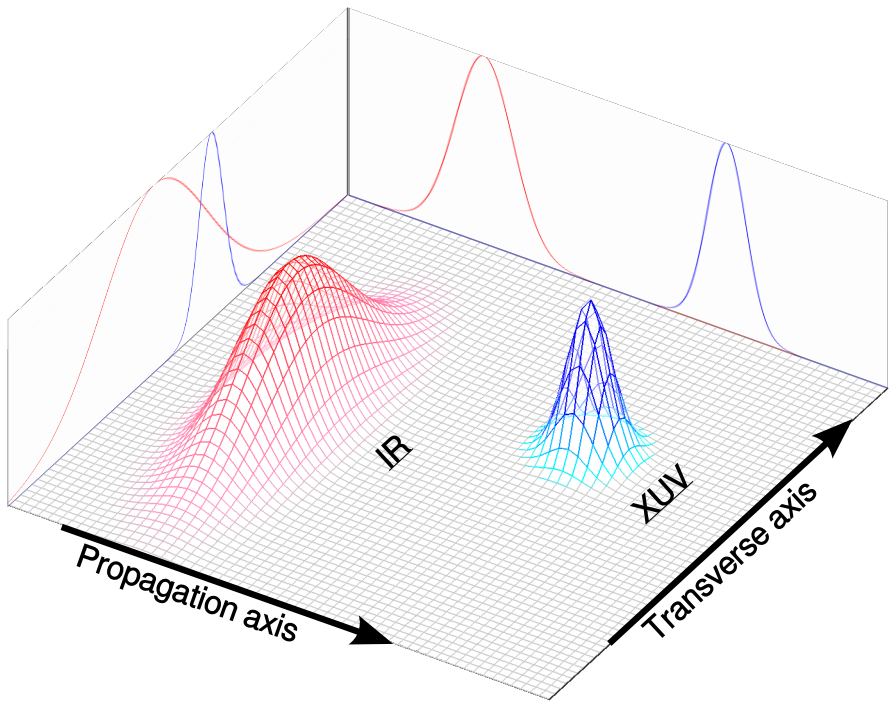

Figure 2.3: Illustration of the two light pulses used in the realization of control of XUV emission.

where

$$\delta\omega \propto E_0^2(t). \tag{2.41}$$

This means that the resonance frequency will follow the intensity shape of the IR pulse, and after interaction with the IR pulse, all states are back to the unperturbed resonance states. In the special case where a superposition exists, the shift in resonance frequency results in a phase change,

$$\Delta\phi = \int \delta\omega(t)\mathrm{d}t. \tag{2.42}$$

2.9 Controlling the emission

So far we have seen that emission from an ensemble of gas atoms, if excited by a coherent pulse, will constructively add up in one direction and send out a beam (sec. 2.4). This corresponds to plane wave fronts in the emitted field, such that the phases of the emitting atoms are the same along the wave front.

The aim is to control the XUV emission, which is the same as controlling the wave fronts of the emitted light, or similar to controlling the phase of the emitting atoms. This can be done by adding a phase to the emitting atoms in a controlled way with a non-resonant IR pulse, as the previous section shows in eq. 2.42. If this pulse has a uniform spatial intensity in the interaction with the atoms, all atoms will be AC

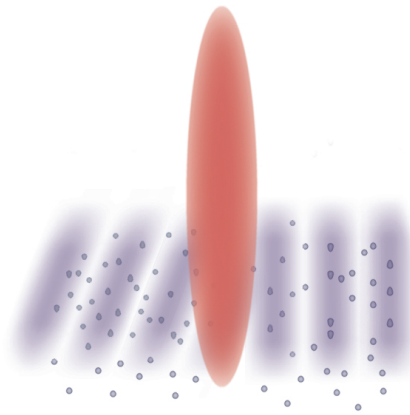

Figure 2.4: Illustration showing the IR control pulse traveling towards the right side. After the interaction with the pulse, the wave front of the emission from the gas is rotated.

Stark shifted by the same amount and the end result will be a constant phase added to the emitted light. In the case where E_0 of the Stark shifting pulse is different for emitting atoms at non-identical spatial positions, the spatial phase and wave front of the emission are changed. The phase shift of the ensemble is then spatially dependent, $\Delta\phi(x, y)$, as is the wave front of the emitted light. The shape of the wave front is thus changed by the integrated spatial intensity profile of the IR pulse. In the simplest case, rotating the wave fronts, the emitting atoms should be exposed to a linear spatial intensity gradient.

This can be accomplished in the following way. A XUV pulse and an IR pulse are sent through a gas of noble atoms (fig. 2.3). As the XUV excitation pulse passes the atoms, it ends up in a superposition between the ground state and an excited state. The IR control pulse then interacts with the atoms, AC Stark shifting them. Due to the spatial offset and the difference in the spatial width between the two pulses, the emitting atoms experience a gradient close to linear intensity. After the IR pulse, the atoms have accumulated a phase and wave fronts are rotated compared to before the IR pulse. This is illustrated in fig. 2.4. The spatially offset IR pulse travels through the gas and the atoms closer to the center of the IR pulse accumulate a larger phase, as the intensity of the pulse is higher than further out from the center. After the two pulses have passed, the wave fronts are rotated and XUV light is emitted in the new direction of the wave fronts and not along the XUV excitation pulse.

Scanning the delay between the XUV excitation pulse and the IR control pulse in principle enables an easy way to measure the decay time of the emission from resonances in atomic ensembles. After the XUV excitation pulse has passed the gas, the emission from the atomic ensemble will follow in the same direction as the excitation pulse and start decaying. Increasing the delay between the excitation pulse and control pulse thus gives the excited atoms more time to decay before redirecting the emission signal. It is also possible to study the part of the emission that is not redirected. This has been done multiple times, but instead of redirecting the emission, it was stopped [4]. Studying the on-axis emission always includes the excitation pulse

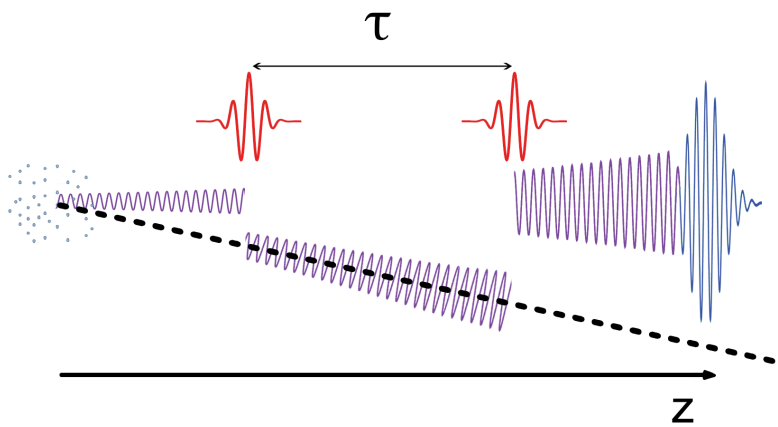

Figure 2.5: Illustration of the emission (purple) from resonance in an atomic ensemble after one XUV excitation pulse (blue) and two IR control pulses (red). The control pulses have different spatial overlaps (not shown) and redirect the emission in opposite directions. This creates a pulse shape in the emitted XUV light in the direction of the dashed black line.

as well. When redirecting the emission, one advantage is the good signal to noise and simple analysis.

Full control of the IR pulse described by $E_0(t, x, y, z)$ permits full control of the XUV emission and can arbitrarily shape the redirected XUV emission. Redirection of the emission does not need to be a single event. Increasing the number of control pulses to two similar ones also enables two redirections. This sends the emission from the atoms in three directions: not redirected, redirected once, and redirected twice. Studying only the second direction, the first control pulse redirects light into this direction, and the second control pulse redirects light out of this direction. This creates a pulse shape of the XUV emission. If the second control pulse is spatially shifted, the light can be redirected to the original direction (fig. 2.5). Increasing the number of control pulses, with every other pulse redirecting the wave front the opposite way, then creates a pulse train of emitted XUV pulses. The phase of the emitted light can also be changed with a flat intensity profile of the control field. Thus, with full control, both spatial and temporal, of the control field, the XUV emission can get an arbitrary spatial and temporal shape. This is the idea behind a opto-optical modulator in the XUV.

Chapter 3

Methods

The work in this thesis is in the research field of ultrafast optics. This research field utilizes cutting-edge laser technology to create ultra-short light pulses. With these short pulses, ultrafast processes and movements of the electrons, on the order of femtoseconds or attoseconds, can be studied in atoms or molecules. For the work presented in this thesis, ultra-short coherent XUV and IR light pulses were sent through noble atomic gases, Argon, Neon and Helium.

The aim of this thesis is to control XUV light. With a short coherent XUV excitation pulse, a polarization is created in the gas. This polarization has a longer decay time than the XUV excitation pulse and induces an AC electric field, light, that is sent out after the excitation pulse. With an IR pulse that is also ultra-short in time, the emission from the gas is controlled. To do this, the delay between the XUV excitation and IR control pulse needs to be adjustable. Furthermore, the spatial overlap between the two pulses in a target gas and the intensity of the control pulse should be controllable. After the gas target, there should be an XUV spectrometer where it is possible to measure divergence and direction of the light.

This chapter is structured as follows. The laser system that is used to deliver IR pulses is presented. Then there is a section describing the setup used for generation of XUV excitation pulses and where the overlap between the excitation and control pulses are controlled. After that, the chamber in which the pulses interact with the target gas, as well as the XUV spectrometer, are briefly described. Then follows a section about the XUV light from the setup and a section about the various target gases and the transitions of interest. This chapter ends with a section about how the data was processed.

3.1 The laser system used

One laser system at the Lund Laser Center was developed by Amplitude technologies, and the laser generates 20 fs pulses centered at 800 nm with a 1 kHz repetition rate. This is the laser system used in the experiments and a short summary of the system will be performed. A more detailed description can be found in ref. [25].

The laser system begins with a Ti:Sapphire oscillator (Rainbow v1, from Femtolaser) with a 78 KHz repetition rate. The 2 nJ output pulses are centered at 800 nm

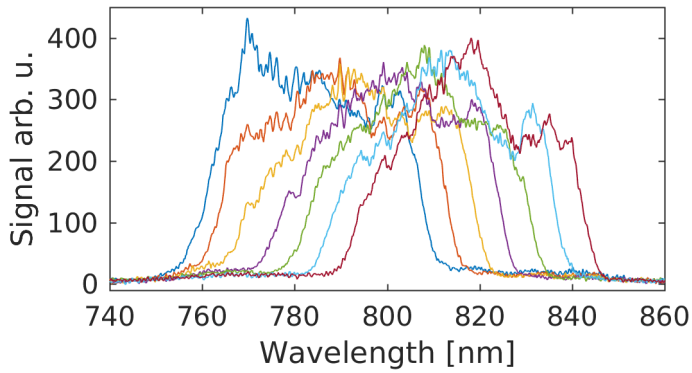

Figure 3.1: Spectrum out from the IR laser when tuning the central frequency.

with <7 fs duration, which corresponds to more than 300 nm bandwidth. This bandwidth is reduced by external mirrors to 100 nm, which also increases the duration of the pulses. The pulses are then sent to a stretcher, where they are strongly chirped, reducing the peak power by making the pulses longer. The spectral phase and amplitude of the pulses are modulated by sending them through an acusto optical modulator (AOM) (Dazzler, from Fastlite). The pulses are amplified in four steps: a preamplifier, a regenerative amplifier, and two 3-pass amplifiers. A preamplifier takes the pulse energy up to 250 nJ, followed by a regenerative amplifier that reduces the repetition rate to 1 kHz and increases the power to 0.5 mJ. A 3-pass bowtie-shaped amplifier increases the pulse to 3 mJ, and a final 3-pass cryogenic-cooled crystal amplifies the energy in the pulses up to 10 mJ. These are the optimized values, and more typically the energy after the amplifiers is 6-7 mJ. All amplifiers are Ti:Sapphire crystals pumped with 527 nm, and the first three are pumped with a frequency-doubled Nd:YLF laser by Photonics (DM 30-527). The last stage is pumped with an other Nd:YLF laser (It was Evolution 45 from coherent but was in 2016 changed to Terra from Continuum). Inside the regenerative amplifier is also an AOM, similar to the Dazzler, which reduces gain narrowing and shapes the spectrum to a tophat. The long, strongly chirped pulses are compressed with gratings after amplification, reaching the Fourier transform limited length of 20 fs. Through the compressor one-third of the power is typically lost, resulting in energy in the output pulse of 4-5 mJ. After the compressor, it is possible to measure the duration and the spectral phase of the pulses with a f-2f interferometer (Wizzler by Fastlite), which is always online. The measured phase can be used for feedback to the Dazzler to compensate for higher-order chirp in the pulse. Thus, the laser system reliably delivers Fourier transform limited pulses.

The laser system supports a bandwidth of 100 nm centered at 800 nm. Within this range, it is possible to reduce the bandwidth with the Dazzler. This results in longer output pulses but allows for tuning of the central frequency. In fig. 3.1 is the measured output spectrum when the laser is tuned to different central frequencies. The lower limit to bandwidth is set by the amplifying crystals. A narrow bandwidth will lead to shorter pulses before the compressor, since the pulse duration of the highly chirped pulse is given by the bandwidth and shorter pulses lead to higher peak power in the amplifier chain. This can easily destroy the crystals, especially the last one.

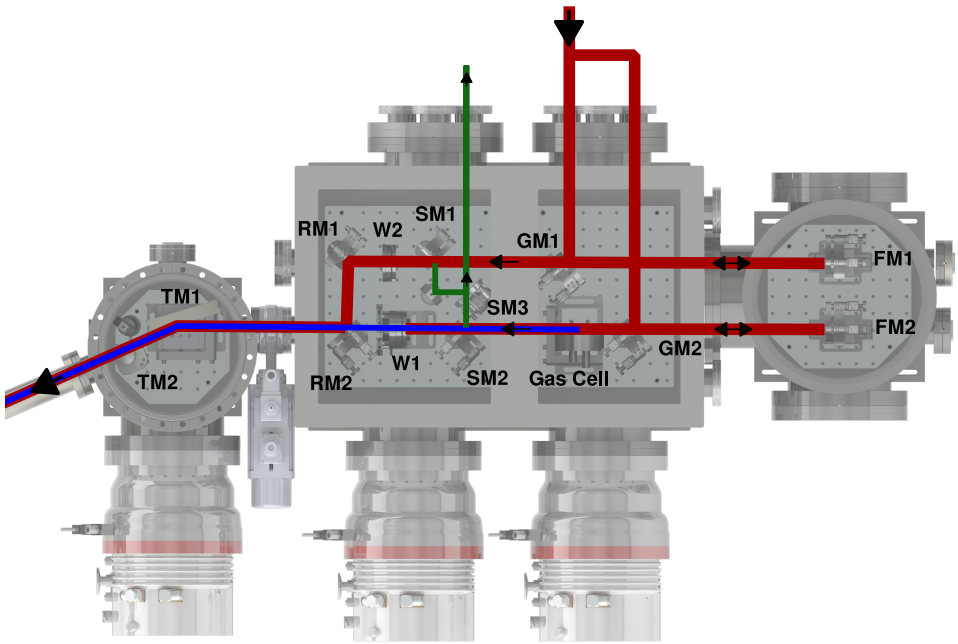

Figure 3.2: Schematic illustration of the interferometric setup. The red path is the IR beam. The blue path is the XUV beam, which is generated in the gas cell. The green path is where part of the beam is split off from the two other beam paths and used for active stabilization. All mirrors are silver-coated mirrors to allow multiple wavelengths. GM1 and GM2 are holey mirrors that reflect the beam towards FM1 and FM2. FM1 and FM2 are spherical focusing mirrors with f = 50 cm resp. 40 cm. They focus the beam back through the hole in GM. SM1 and SM2 are holey mirrors that pick off a part of the outer rim of the beam. RM1 reflects the beam to RM2, which is a holey mirror where the XUV pass through the hole and the IR reflects on the mirror to recombine the two paths. W2 is an iris. W1 has both an iris and a filter wheel. TM1 is a platinum-coated toroidal mirror with f = 30 cm. TM2 is a mirror that can be flipped in to the beam and redirect it out from the chamber through a window port.

3.2 Interferometric setup

From the main laser system, the IR beam is sent to the interferometric setup. Mirrors are used to reduce the beam diameter to 10 mm FWHM and to align the IR beam. The IR beam is made to propagate collinear with a beam from a HeNe laser (CW 632.8 nm, R-32734, Newport) through a wedged dielectric mirror, and the HeNe is used for alignment and active stability feedback. Once the IR pulses reach the setup, the power of the pulses has dropped to between 2-3 mJ.

In fig. 3.2, a schematic drawing of the setup is presented. The red lines show the IR beam and the blue the XUV. The green beam path is used for active stabilization and will be commented on later in this section. The gray parts are chambers connected to each other, sometimes with a small hole or a valve, and in the lower part of the figure are three turbomolecular pumps (HiPace700, Pfeiffer Vacuum), which keep the

pressure in the chambers down to at least $1 \cdot 10^{-6}$ mbar without any gas load.

Two beam paths are shown, starting outside the chamber. One, the pump beam path, goes through the gas cell and is used for generating an XUV beam through high-order harmonic generation (HHG) [28] [16] [10]. This process uses the oscillating strong electrical field of the generation pulse to send part of an electron out and then drag it back to collide with the parent atom and give rise to emission. As this happens every half cycle of the generating pulse, the resulting sharp amplitude peaks of the field in time corresponds to higher frequencies, that is, odd harmonics of the generating wavelength. The spectrum and the output will be presented in section, sec. 3.4.

The other, probe-beam path is later recombined with the XUV beam. From this path comes the IR pulse that is used to control the emission from the target gas. In the probe-path is a possibility of changing the delay and relative position of the XUV and the IR pulse.

The beams enters the vacuum chamber through Brewster windows, thin glass structures at the Brewster angle for the beam polarization, to retain as much of the intensity as possible. They are then reflected towards focusing mirrors with two holey mirrors (GM1, GM2). The mirrors have a 3 mm hole in the center cut with an angle of 45°to the normal of the surface. The beam thus becomes annular, unless it is small and off-center on the holey mirror. The beams are then focused with spherical mirrors (FM1, FM2) back through the hole in the holey mirrors (GM1, GM2).

At the focus of the pump beam path is a pulsed gas cell (see fig. 3.2). The gas cell used is an Attotech GR020 pulse valve with a T-shaped nozzle. Through the stem of the T, gas is added, and the laser shoots through the bar. The diameter of the tube through which the laser goes is 1 mm, and the length is 3 mm. In the gas cell noble gases are pulsed out at a 1 kHz repetition rate to match the rate of the IR laser pulses. The gas used is usually Ar with a backing pressure of 2-4 Bar. The actual gas pressure in the nozzle is not known. From this nozzle, the gas spreads out like a plume through the holes of the tube. This increases the ambient pressure in the chamber and reaches a steady state with the turbomolecular pumps. The ambient pressure is what is measured, and the typical pressure in the chamber with the gas cell is 2 μbar.

In the gas, the XUV beam is generated through the HHG process. For this process, the intensity in the generation pulse is a crucial parameter, which is controlled with an iris outside the entrance for the pump beam path to the chamber.

After the gas cell in the pump beam path, the generation IR is removed. This is normally done by passing an ultra-thin metallic filter (filter wheel in W1, custom component from Smaract). With standard metallic filters, including Aluminum, the ninth harmonic of 800 nm does not go through, and the flux of the harmonics is reduced. As a complement, in this setup an iris (SID-0-22-S-HV, Smaract) is also placed in the HHG beam path after the gas cell (W1). If the gas pressure is not too high, the annular IR beam generating the XUV preserves the shape, while the XUV is centered in the middle. It is thus possible to block the generating IR beam with the iris and let the XUV through. In a less than ideal world, however, most of IR is blocked and a very weak part can, through diffraction or reshaping of the beam in the gas, also be emitted in the center and thus pass the iris.

The IR pulse from the probe beam path is recombined with the XUV pulse with a holey mirror (RM2), where the XUV beam passes through the hole. After recombination, the beams are refocused with a platinum-coated toroidal mirror with f=30 cm. As both beam path foci are 60 cm before the toroidal mirror, this yields a 2f-2f con-

figuration such that the beams are refocused 60 cm after the toroidal mirror. This refocus spot is where the target is placed.

For configuration, measurement and stability, a couple of technical implementations are performed. The setup has two linear translation stages, one for each focusing mirror (FM1, FM2). With the linear translation stage in the pump beam path, the position of the focus in the gas cell is adjusted and the linear translation stage connected to FM1 is used to control the temporal overlap between the pulses. The translation stages (SLC-2445-S-HV, Smaract) use a stick-slip technique that permits a long range of motion but introduces a small shake every 1.5 μm, which corresponds to 10 fs in delay for the setup when scanning. Furthermore, the stages can measure the position; however, this position signal sometimes rapidly jumps while operating. This error is possibly from scattered IR light, so a later add-on was a cover, which seems to work well, over the linear stage to protect it from those stray lights.

To control the intensity of the IR probe pulse, an iris (SID-0-22-S-HV, Smaract) is placed before the recombination mirror (W2). This does introduce the additional effect of changing the beam waist of the IR pulse in focus as the intensity is scanned.

The alignment of the beam paths is set by the mirrors, and to enable changes while there is low pressure in the chamber, the key mirrors have motors controlling the horizontal and vertical tilt angle. The mirrors with motors are GM, FM, RM2 and SM2. Controlling the tilt of RM2 is the way that the spatial overlap between the two beams, the IR beam from the probe path and the XUV beam is changed. The motors used (open-loop picomotors, New focus) are piezo step types that rely on the difference between static friction and dynamic friction to rotate a screw, similar to how Smaract linear translation stages work. We found that they wore out quite fast. Thus, working with them almost always require a visible feedback.

To see the alignment inside the chamber, two cameras are used. One focuses on the gas cell nozzle, where scattered light from the IR generation beam is reflected on the sides of the hole. The other camera is positioned for imaging the focus after the toroidal mirror. With a flip mirror (TM2), the beam can be taken outside the chamber and, after intensity reduction, focused on the camera. This makes it possible to observe the focus of the IR beam and the HeNe beam but not the XUV beam. Still, for alignment purposes, that is enough since the generated XUV will keep the same beam path as the IR generation beam. The fastest way to align the setup is often to open the chamber, align and pump down. The pumping of the chambers only takes 30-60 min. As the pressure in the chambers is reduced from the atmosphere, small changes to the alignment need to be corrected for.

For high-precision experiments, the stability of both the pointing and the delay of the interferometer is crucial. To increase the temporal stability, an active feedback loop is used to remove the drift of the path lengths. This is also used for controlling the delay between the pump and probe path. This feedback is based on a fringe pattern on a camera. The fringes come from spatially overlapped HeNe beams, one from each beam path, with an angle between the beams (green beam path, SM1, SM2, SM3). This measures the change in phase between the two HeNe beams, which correspond to changes in the optical length difference between the beam paths. From the measured changes, a signal is sent either to the Smaract linear translation stage in the probe beam path, controlling FM1, or a piezo linear translation stage (PX 100 CAP vacuum, Piezosystems Jena) positioned on the same place. The response time is a magnitude slower for the Jena stage, but within the delay range of the stage, $\pm$180 fs,

there are no sudden movements. It should be noted that the actively stabilized paths do not include RM1 and RM2 but SM1, SM2, SM3 and one small mirror between SM1 and SM3. This means that the real interferometer drifts in a way that we do not compensate for. The setup is continuously improved and the mirror SM1 has recently been moved between RM1 and RM2 and the small mirror has been removed. This should increase drift stability. With the feedback and the Smaract translation stage, the fastest frequencies that can be compensated for are 15-20 Hz. No faster vibrations and changes to the beam path length are possible to stabilize and thus becomes noise. With active feedback on, the RMS for the interferometer is close to 50 as.

The setup is very versatile and multiple configurations have been used. The largest difference in the configurations is how to split the incoming IR pulse to each beam path. One possibility is to send full-sized beams and control the power sent into each path with a beam splitter. The other possibility is to split the beam with holey mirrors and either send the center part to the pump beam path and the annular part to the probe beam path, or vice versa. The main concern for the pump beam path is to have enough power for the HHG process that generates the XUV pulses. For the probe beam path, the focus after the toroidal mirror is the most important, both the beam waist and the shape. What we experienced is difficulty in ensuring proper focus from an annular IR beam in the target focus, as it acquires a strong ring structure and is easily astigmatic after the toroidal mirror. A well-shaped IR focus more similar to a Gaussian shape was found with a small non-annular beam in the probe path. This results in an increased IR beam waist.

3.3 Target setup

The target setup is a freestanding table connected to a bellow and metallic tubes to the output of the XUV source setup (fig. 3.3). It consists of a vacuum chamber on a frame with elliptical differential pressure holes at both the laser input and laser output. The chamber holds an Attotech pulsed valve gas cell, similar to the HHG gas cell. The target gas cell is mounted on a three-dimensional x-y-z translation stage. Multiple gas nozzles can be used, but the most common one is a T-shaped device with a 5 mm long cylindrical opening, 1 mm in diameter. It is also possible to attach an optical fiber to one of the nozzles. The fiber can collect sideways emission from the gas and through a fiber feed-through be connected to a fiber spectrometer. Underneath the chamber is a turbomolecular pump, similar to the ones on the interferometer setup.

The chamber is connected to a XUV flat-field spectrometer. A focusing XUV reflection grating (Hitachi grating 001-0639) is located on a rotation state (SR-3610-S-HV, Smaract). The XUV light is reflected onto a multi-channel plate(MCP), where incoming photons cause an avalanche of electrons. These electrons are accelerated onto a phosphor screen (custom product, Photonis), where a camera (Pike F-505B, Allied Vision Technologies) records an image. With the grating rotation stage, it is possible to shift the spectral region on the MCP, as well as get the zero order beam out through a window port. The grating is also positioned on a linear translation stage (SLC-2460-S-HV, Smaract), enabling movement of the grating out of the beam and allowing the beam to go out from the chamber through another window port. The higher harmonics in the XUV are absorbed in the glass, but the IR and the first few harmonics can be measured.

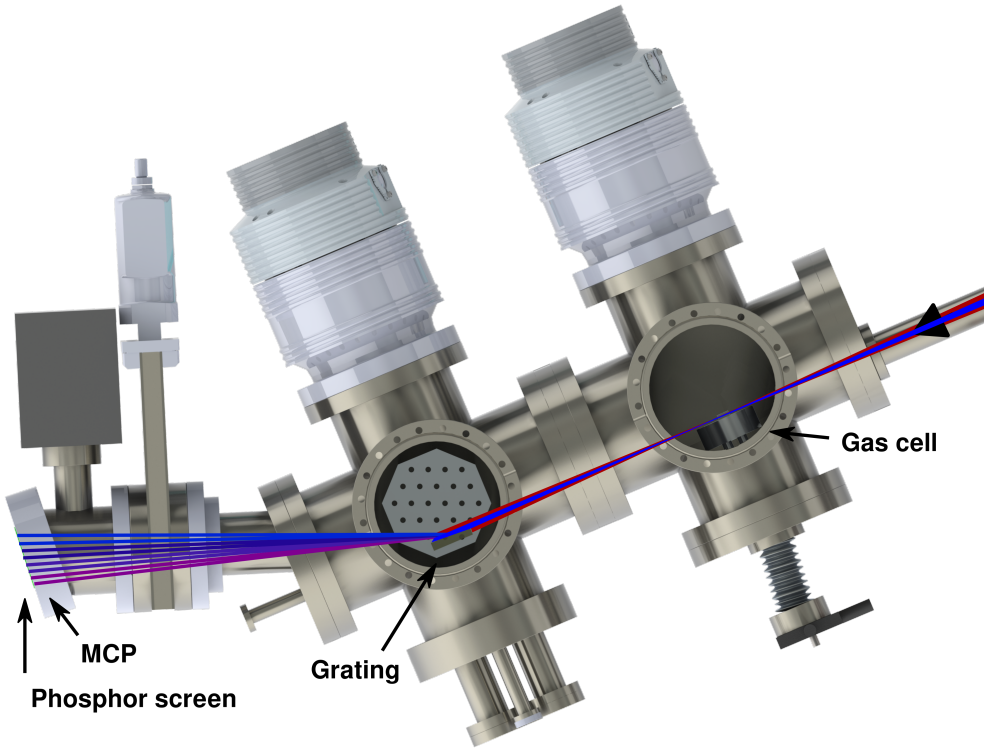

Figure 3.3: Schematic illustration of the target chamber together with the XUV spectrometer.

The MCP can be separated from the rest of the chamber with a valve. With an ion pump connected, the MCP is always at low pressure, which reduces startup time after the chamber has been ventilated. In the main chamber of the XUV spectrometer, another turbomolecular pump is used to keep the gas pressure at the MCP low when operating with high gas pressure in the target chamber. The standard during experiments in the ambient pressure in the chambers would be 10^{-3} mbar for the target chamber and 10^{-5} mbar for the XUV spectrometer chamber.

3.4 XUV

There are various sources for coherent XUV radiation, but for the setup described above, the process of HHG is used. In all the experiments, Ar was used as the generation gas in the interferometric setup. The wavelengths of interest for the experiments range from 90 to 40 nm, which corresponds to between the 9th and 19th harmonic of the 800 nm IR. Lighter noble gases, Ne or He, in which the electrons are more tightly bound, can generate much higher orders of harmonics, but reduce the photon flux[31], and heavier noble gases, Xe or Kr, do not result in harmonics that cover the desired

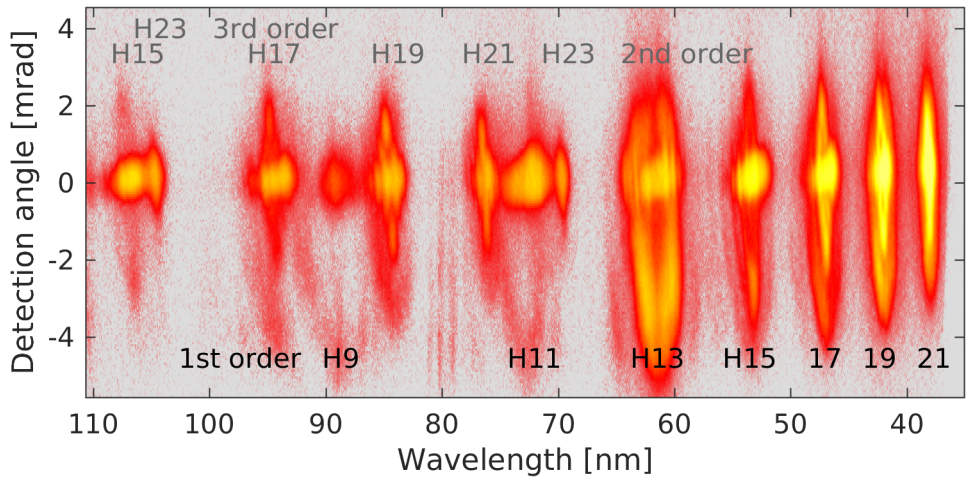

Figure 3.4: Spectrum of the light from the HHG XUV source. Ar is used as generation gas with an ambient pressure in the chamber of 3 μbar. The color scale is logarithmic. From the HHG process, harmonics of the IR are created, and they are marked with black numbers. As a grating spectrometer is used, higher diffraction orders of the harmonics from the source are also seen in gray. The emission from the short and long trajectory in the harmonics (the zero detection angle blobs and the rings around them) can easily be seen. The emission lines around 80 nm also show that the generation gas is Ar. The data was taken 2014-11-28.

spectrum[1]. Thus, Ar have been a suitable gas to use in the HHG process to deliver XUV pulses for the experiments.

Fig. 3.4 shows a spectrum of XUV signal generated from Ar and detected with the XUV spectrometer. Both of the axis are position on the MCP detection plate. This can be remapped though so the x-axis gives the wavelength and the y-axis give the direction of emission. Thus, a cone of light sent out with a given narrow band frequency will show up as a vertical line on the spectrometer[2].

The generated harmonics can be separated into two contributions with almost the same energy, one where the electron just makes a small excursion from the parent atom, a short trajectory, and one where the electron is driven further away before coming back, a long trajectory. The less intensity-dependent short trajectory harmonics are seen as small, more distinct, circular features close to zero detection angle, and the more intensity-dependent long trajectory harmonics are seen as the more divergent elliptical rings. The intensity dependence means that the spatial phase for the short trajectory is almost constant across the focus, while the long trajectory has a strong difference in the phase in the center and edge of the focus. This yields wave fronts that are flat for the short trajectory and curved for the long trajectory. Thus, the long trajectory is more divergent and interference in the harmonic signal from the atoms give a spatial modulated structure in the farfield. The strong intensity dependence is also true for the temporal shape of the generation pulse and results in strong blue and

[1] And are much more expensive.

[2] In fig. 3.4 there are some lines around 80 nm that come from emission from higher s and d states from Ar atoms in the HHG gas cell. This emission seems to be somewhat directional and not uniform in the emission direction as fluorescence should be.

red shifting of the long trajectory, which modulates the spectrum of the harmonics. This is the reason for the ring structure of the long trajectory. For the most energetic harmonics (cut-off) the separation into long and short trajectory disappears.

To separate the various wavelengths, the spectrometer uses a focusing grating. Normally the signal that is studied in these experiments is in the first diffraction order. As can be seen in fig. 3.4, however, the second diffraction order from the higher harmonics (H17 at 95 nm mark and H19 at 85 nm mark) overlap with the lower harmonics (H9 at 90 nm).

When using HHG as an XUV source in the following experiments, the more divergent emission is unwanted. Rather, a well-defined and homogeneous intensity over the XUV beam makes it easier to separate and study the emission from the target gas. Closing the iris in the pump arm (fig. 3.2 W1), the divergence of the XUV beam can be reduced, and a divergence of 1-4 mrad was used on the XUV beam in the experiments.

3.5 Target gases

The experiments were conducted with three different target gases: Ar, Ne and He. All three of them are noble gases, which means filled electron orbitals in the ground state.

3.5.1 Argon

The electronic ground configuration of Ar is $1s^2 2s^2 2p^6 3s^2 3p^6$. For the experiments in this thesis, the transitions of interest are a 3p electron to the 5s or 3d state, or a 3s electron to np states, with $n > 3$.

Excited configurations of the type $p^5 nl$ in the noble gases are usually described in the *jK* coupling scheme, rather than the more familiar *LS* coupling [11]. In a $p^5 nl$ configuration the largest energy splitting is due to the spin-orbit interaction in the p^5 ^2P parent term, described by its *j*-value, followed by the electrostatic interaction with the outer electron, described by ints *l*-value. The angular momenta $\boldsymbol{j}$ and $\boldsymbol{l}$ are then coupled to an intermediate $\boldsymbol{K}$ and finally coupled with the spin of the outer electron, which is 1/2 as it is one electron, to generate the total angular momentum $\boldsymbol{J}$. The usual notation in *jK*-coupling is $j[K]_J$.

Considering the transition rules, only 5 transitions are of interest from the 3d and 5s states to the ground state. The ground state is $^1S_0$, which yields dipole-allowed transitions from $^1P_1$ states. For Ar, as the *LS* coupling is not a good way to describe the atom, the states are mixed between the pure basis set. Thus. all states with J=1 may couple to the ground state. In tab. 3.1 are given the configurations, terms, transition wavelengths, transition energies, radiative lifetimes τ, and transition dipole moments. The transition dipole moments have been calculated from the transition probability or Einstein coefficient, A, reported in NIST [24], through [21]

$$d = \sqrt{\frac{3\epsilon_0 h c^3}{2\omega^3} A}. \tag{3.1}$$

Worth noting is that the radiative lifetime of a transition is the inverse of the Einstein A coefficient, if that is the only transition from the upper state.

elec. conf.	jK term	wavel. [nm]	energy [eV]	τ_{spon} [ns]	$d \cdot 10^{-30}$ [Cm]
$3s^2 3p^5(^2P_{3/2})3d$	$3/2[1/2]_1$	89.43	13.86	76^a	
$3s^2 3p^5(^2P_{3/2})5s$	$3/2[3/2]_1$	87.99	14.09	10.1^b	1.36
$3s^2 3p^5(^2P_{3/2})3d$	$3/2[3/2]_1$	87.61	14.15	3.48^b	2.54
$3s^2 3p^5(^2P_{1/2})5s$	$1/2[1/2]_1$	86.98	14.25	17.5^b	0.904
$3s^2 3p^5(^2P_{1/2})3d$	$1/2[3/2]_1$	86.68	14.30	3.0^b	2.69

Table 3.1: States and transitions down to the ground state in Ar. The data for lifetimes are *a*) calculated from ref. [33] and *b*) measurements by Lawrence[26]. The transition dipole moments are calculated using eq. 3.1 and values from NIST[24].

The 3d state with the lowest energy does not have a measured spontaneous lifetime, but from calculations[33] and experiments on the oscillation strength [26], it does not couple well with the ground state, having an order of magnitude lower of transition probability than the other 3d and 5s states of interest. This should mean that this state does not have much $^1P_1$ character.

The Rabi frequency, in rad/s, is given by

$$\Omega = \frac{dE}{\hbar}, \tag{3.2}$$

where E is the electric field amplitude. The Rabi frequency represents the frequency of energy transfer between two states coupled with a resonant field. Integrating the time-dependent Rabi frequency, as the electric field amplitude might change with time, thus gives the total rotation of the Bloch vector for these two states. To do one flop such that energy is transferred from one state to the other, the integral over the Rabi frequency should be π, which is set by how the amplitude of the electrical field changes.

Thus it is of interest to know how high intensity of the XUV pulse is needed to make a complete transfer from the ground state to an upper state. Assuming a Gaussian pulse with a FWHM in time of 25 fs, and using a transition dipole moment of $2.54 \cdot 10^{30}$ Cm, the peak intensity of the XUV pulse needs to be $3.2 \cdot 10^{12}$ W/cm^2.

Although the intensity of the XUV pulses has not been measured, the intensity of the generation pulse which drives the HHG process is on the order of $10^{14} - 10^{15}$ W/cm^2, and the HHG process has an efficiency on the order of 10^{-5}. Furthermore, the more divergent emission is blocked and only the intensity of one harmonic is of interest. Considering all these things together, we are far from driving the population back and forth with just the XUV pulses from the HHG source.

In tab. 3.2 is the beginning of the $3s3p^6np$ series of resonances. The line width of these states has been measured, and the lifetime is calculated from these values using $\tau = \hbar/\Gamma$ [12]. As these states have energies above the ionization level, they are called auto-ionizing and show a different behavior than other states. Much work has been done by Fano in describing their line shape [15]. As photons in this region would normally be absorbed by ionizing the atom, these resonances act as window resonances. The phase of the emitted light from these auto-ionizing states is thus, as opposed to the normal absorbing resonance, in phase with the excitation field.

elec. conf.	LS term	wavel. [nm]	energy [eV]	Γ [meV]	τ [ps]
$3s3p^6 4p$	$^1P_1$	46.58	26.62	80.3	0.0082
$3s3p^6 5p$	$^1P_1$	44.29	28.00	28.5	0.0231
$3s3p^6 6p$	$^1P_1$	43.49	28.51	12.2	0.0540
$3s3p^6 7p$	$^1P_1$	43.11	28.76	6.6	0.10
$3s3p^6 8p$	$^1P_1$	42.91	28.90	4.5	0.15
$3s3p^6 9p$	$^1P_1$	42.77	28.99	4.1	0.16

Table 3.2: States and transitions to ground state in Ar for exciting one 3s electron to np state. The line width of the states is measured [5], and the decay time calculated from that.

elec. conf.	jK term	wavel. [nm]	energy [eV]	τ_{spon} [ns]	$d \cdot 10^{-30}$ [Cm]
$2s^2 2p^5(^2P_{3/2})3s$	$3/2[3/2]_1$	74.37	16.67	23.6	0.833
$2s^2 2p^5(^2P_{1/2})3s$	$1/2[1/2]_1$	73.59	16.85	1.73	2.94
$2s^2 2p^5(^2P_{3/2})4s$	$3/2[3/2]_1$	62.97	19.69	10.4	0.652
$2s^2 2p^5(^2P_{1/2})4s$	$1/2[1/2]_1$	62.68	19.78	8.57	0.804
$2s^2 2p^5(^2P_{3/2})3d$	$3/2[1/2]_1$	61.91	20.02	12.0	0.527
$2s^2 2p^5(^2P_{3/2})3d$	$3/2[3/2]_1$	61.87	20.04	8.53	0.884
$2s^2 2p^5(^2P_{1/2})3d$	$1/2[3/2]_1$	61.56	20.14	11.9	0.561

Table 3.3: States and transitions down to ground state of Ne. Radiative lifetimes are reported by ref. [1]. The transition dipole moments are calculated using eq. 3.1 and values from NIST[24]

3.5.2 Neon

In Ne, the transitions of interest are very similar to Ar, but now it is the 3s, 4s and 3d states that can be resonant with harmonics. The ground state is $1s^2 2s^2 2p^6$ and, like the lower states in Ar, the coupling is best described by jK-coupling. The transition dipole momentum is calculated in the same way as for Ar.

3.5.3 Helium

As opposed to Ar and Ne, He transitions where one s electron is excited can be described well with LS-coupling, meaning that every n quantum number will have only one state, the singlet, that couples well to the ground state. The transition dipole moment is calculated similarly to that for Ne and Ar, based on the Einstein A coefficient. For the spontaneous lifetime, the inverse of the Einstein A coefficient was used.

3.6 Data processing

There is not much data processing done in this thesis. Most of the work has been conducting experiments, but even so, in the Results chapter (ch. 4) the decay of the time dependent signal is given some treatment. I will highlight two delay measurements and the steps taken from the raw data to the presented results.

elec. conf.	LS term	wavel. [nm]	energy [eV]	τ_{spon} [ns]	$d \cdot 10^{-30}$ [Cm]
1s2p	$^1P_1$	58.43	21.22	7.7	3.03
1s3p	$^1P_1$	53.70	23.09	17.7	1.764
1s4p	$^1P_1$	52.22	23.74	41.1	1.109
1s5p	$^1P_1$	51.56	24.05	79.5	0.782
1s6p	$^1P_1$	51.21	24.21	137	0.590
1s7p	$^1P_1$	51.00	24.31	216	0.466

Table 3.4: States and transitions down to ground state i He. The lifetimes are calculated from the inverse of the Einstein A coefficient in NIST. The transition dipole moments are calculated using eq. 3.1 and values from NIST[24]

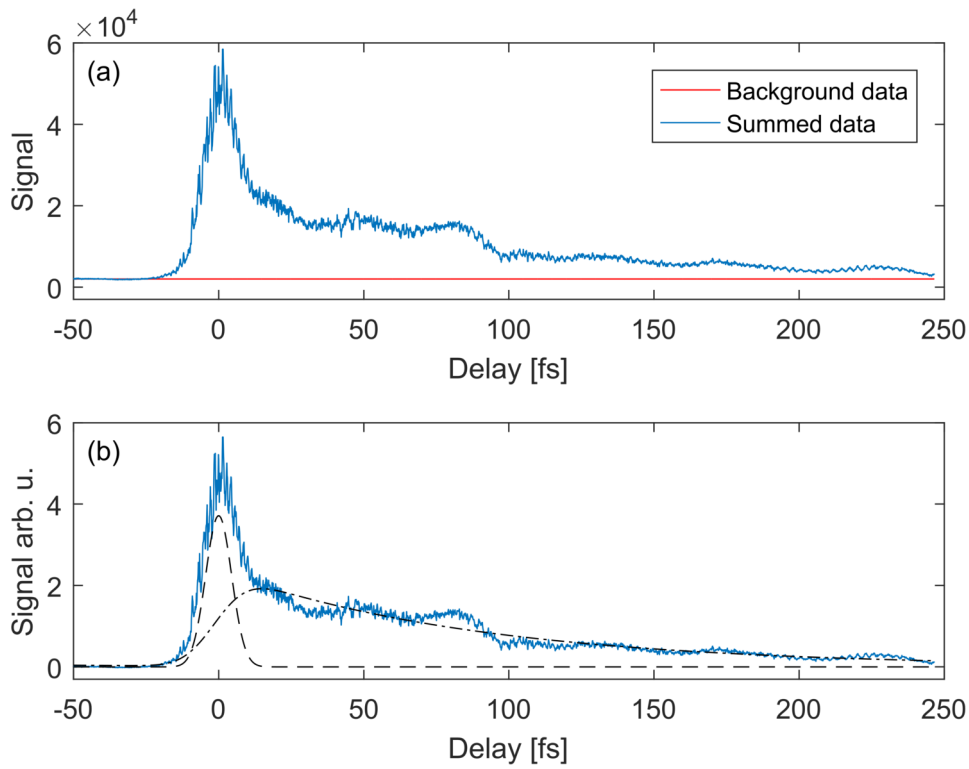

Figure 3.5: Data processing of delay scan in Ar. (a) The summed data for emission from 3d $3/2[1/2]_1$ to ground state in this experiment (blue), together with the used background (red). (b) The data with the background removed, together with the two terms of the fitted eq. 3.3. Dashed line is a Gaussian shape to account for temporal overlap effects between the XUV excitation pulse and the IR control pulse. The dash-dot line models the onset of re-directed emission and an exponential decay. See fig. 4.12 for more experimental details.

In most cases the background is very small compared to the signal. The summed signal comes from a box region in wavelength and detection angle. Since there is no re-directed emission when the control pulse precedes the excitation pulse, the signal measured for that case can be used as a background noise level and subtracted from the whole signal. A data set where this processing is used is in the first delay scan of Ar (fig. 4.12). The summed data in the experiment for the emission from 3d $3/2[1/2]_1$ to ground state is shown in fig. 3.5 (a) (compare fig. 4.12 (c)). The noise in this data is small compared to the signal, and the average value between -50 and -30 fs delay is used as a flat background and subtracted from the whole signal.

To this data is then fitted a model

$$f(t) = \left(\frac{1}{2}\left[1 + a\,\mathrm{erf}\left(\frac{t-t_0}{\sigma_1}\right)\right] + d\right) e^{-\frac{t}{\tau}} + g e^{\frac{-(t-t_0)^2}{\sigma_2}}, \tag{3.3}$$

where the last term is a temporal overlap Gaussian. The first term consist of two factors. The first of them, with the Gaussian error function inside the large parentheses, models the onset of the redirected signal, and the last factor models the exponential decay.

These three parts model physical processes. The temporal overlap Gaussian function accounts for multiphoton processes, things that happen when XUV photons from the excitation pulse and IR photons from the control pulse are together interacting with the atoms, which should then have a shape like the temporal profile of the pulse. Similar to this, the first factor of the first term, the Gaussian error function, also reflects the shape of the control pulse. For a Gaussian shaped temporal profile of the control pulse, the redirection of emission will be fastest at the peak of the intensity. Integrating the redirected light signal should thus have a onset shape which looks like the integrated Gaussian, which is given by the error function. Lastly, the exponential decay part gives the decay constant, τ, which is the desired value. In fig. 3.5 (b) is the signal, with the background removed, plotted, together with the two terms of the fitted function, the temporal overlap Gaussian (black dashed line) and the decay curve with the initial onset (black dash-dot line).

For the experiments with different pressure of Ar, the signal to noise were smaller. In fig. 3.6 is the raw data from the 3d $3/2[1/2]_1$ state (a), and from np $^1P_1$ with n>9 (b) (compare fig. 4.15). Two aspects that are different for this data set are the higher background level compared to the signal, and the lack of flat background signal when the IR control pulse precedes the excitation pulse in (a). To remove the noise and background, a nearby region with equal number of pixels of the spectrometer image with no signal was summed (red data). There are no large fluctuations in the background data and the background from both the 3d $3/2[1/2]_1$ state (a), and from np $^1P_1$ with n>9 (b), are similar.

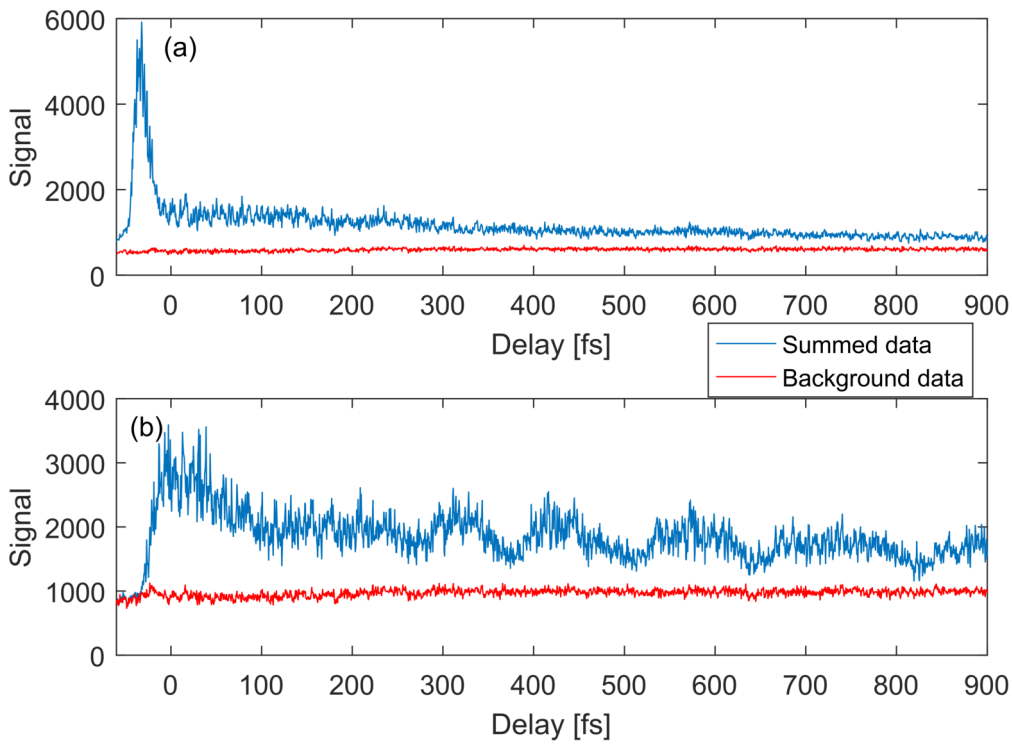

Figure 3.6: Data processing of delay scan in Ar. (a) The summed data for emission from 3d $3/2[1/2]_1$ to ground state in this experiment (blue), and background signal (red), which is summed from a slightly shifted area. (b) The summed data from high np $^1[P]_1$ states emission (blue) and a nearby background signal used (red). See fig. 4.15 for more details.

Chapter 4

Results

The results in this thesis focus on the transient absorption chamber in which XUV and IR pulses interact with clouds of noble gas atoms. Light in the XUV regime, corresponding to resonances in the atoms, is then emitted from the atoms. The control of this emitted light is the key result in this thesis.

This chapter is structured in the following way: First, spectroscopy by sending the light through different gases is described. Second is shown spatial control, where the direction of the emission is controlled. Third, temporal control is presented where the timing of the redirections is controlled,

4.1 XUV spectroscopy

In the study for this thesis, three different target gases were used: Ar, Ne and He. Through these gases a coherent XUV pulse, described in sec. 3.4, was sent. For Ar, this can be seen in fig. 4.1 (for all figures the zero level of the color scale is chosen so as to remove the background noise). Two distinct light-atom interaction effects can be noted between the spectrum recorded with no target gas, (a), and the spectrum of the radiation that has passed through a gas, (b). The first is the absorption above the ionization energy, from harmonic 11 at 72 nm, where the absorption seems to be total, and up to the higher harmonics where the absorption is reduced. This can be understood as photons being absorbed by the atoms, giving the electrons enough energy to leave and thus ionize the atom. For the high-energy photons, the probability of ionization is reduced as the cross-section is reduced. The ninth harmonic at 88 nm has a photon energy below the ionization energy and will not be absorbed by ionization of the gas.

The second distinct effect consists of the sharp lines with broader divergence than the XUV excitation pulse as seen at 87 nm for Ar in fig. 4.1 (b). These are electronic resonances in the atoms, transitions between different energy states, that match the incoming frequencies. The incoming light causes the electrons, which were initially at rest, to start oscillating[1] (see theory). After the pulse has passed, the oscillating

[1] Rather than thinking of this like a ball, the electron could rather be thought of as a cloud. At rest it has a certain, rather symmetrical probability distribution cloud around the core, and when the

electrons cause an electric field to be emitted for a time until they have relaxed and reached the at-rest state again. As the incoming light is coherent, the oscillating electrons are in phase orthogonal to the propagation direction of the XUV excitation pulse, and the interference between their emitted fields will only be constructive along the same propagation direction as that XUV excitation pulse.

4.1.1 Argon

Experimentally Ar is a good target gas for studying XUV resonances with a system that uses HHG from 800 nm. Five bound transitions are easy to reach with the XUV source. Using the default central bandwidth from the laser and not too high gas pressure or intensity in the HHG process gives a ninth harmonic that is resonant with the ground to the lowest of the 3d states, $3/2[1/2]_1$ following the notation in sec. 3.5 (in the rest of this chapter only the electron n and l values and the $\boldsymbol{K}$ value will be used in most cases). This transition is not the easiest for either seeing or finding temporal overlap between the pulses, as the coupling is weak. It is separated from the other possible transitions, making it possible to excite only that resonance.

From the bound states, the emission and coupling to the ground state from 5s[3/2] at 88 nm and the spectrally close transition from 3d[3/2] at 87.6 nm (fig. 4.2) are strong. The XUV excitation pulse is made resonant with these transitions by cutting the bandwidth of the laser and shifting the central wavelength to 790 nm. Roughly 1 nm above them are the two other 5s and 3d states with $\boldsymbol{J}$=1, which are also possible to see, although weaker and more difficult to separate with our spectrometer.

Above these transitions in energy is then, in ascending order, the rest of s and d states with $\boldsymbol{J}$=1 that can emit to the ground state (fig. 4.3). Since Ar is the gas used in the HHG gas cell as well, emission from the bound states can also excite the transitions in the target gas cell, although with different dynamics. In fig. 4.3, spatial control through an IR control pulse is used, slightly redirecting the emission from the gas. The blue lines mark where the d and s states with lowest energy and $\boldsymbol{J}$=1 have been measured, which fits well [29].

Also of great interest in Ar are the auto-ionizing $3s3p^6np$ series of states, which corresponds to excitation of the tighter-bound 3s electron to a p state. These states have potential energies in the continuum above the ionization energy for the 3p electrons and thus are auto-ionizing with very short spontaneous lifetimes. In the absence of the state, light with a wavelength corresponding to the resonance frequency would be absorbed. With the auto-ionizing state light will instead be transmitted through the gas. Through interference between the two paths to the np state, the emission gets an additional π shift in the phase. This means that the emission, instead of being out of phase is in phase with the XUV excitation pulse. The lowest energy of these transitions, the ground state to 4p, is reached with a low central wavelength around 790 nm, and the 17th harmonic (fig. 4.4). The decay of this state is very fast and we have not succeeded in controlling the emission from this state, other than making it disappear. The other auto-ionizing states in the np series have been successfully controlled though. They are reached by tuning the central wavelength up and makes harmonic 19 resonant with the states.

incoming light passes, the electron moves from the at-rest cloud state to another probability cloud state with a higher potential energy. When the electron is not entirely in either rest or excited state the cloud describing the electron will oscillate with time.

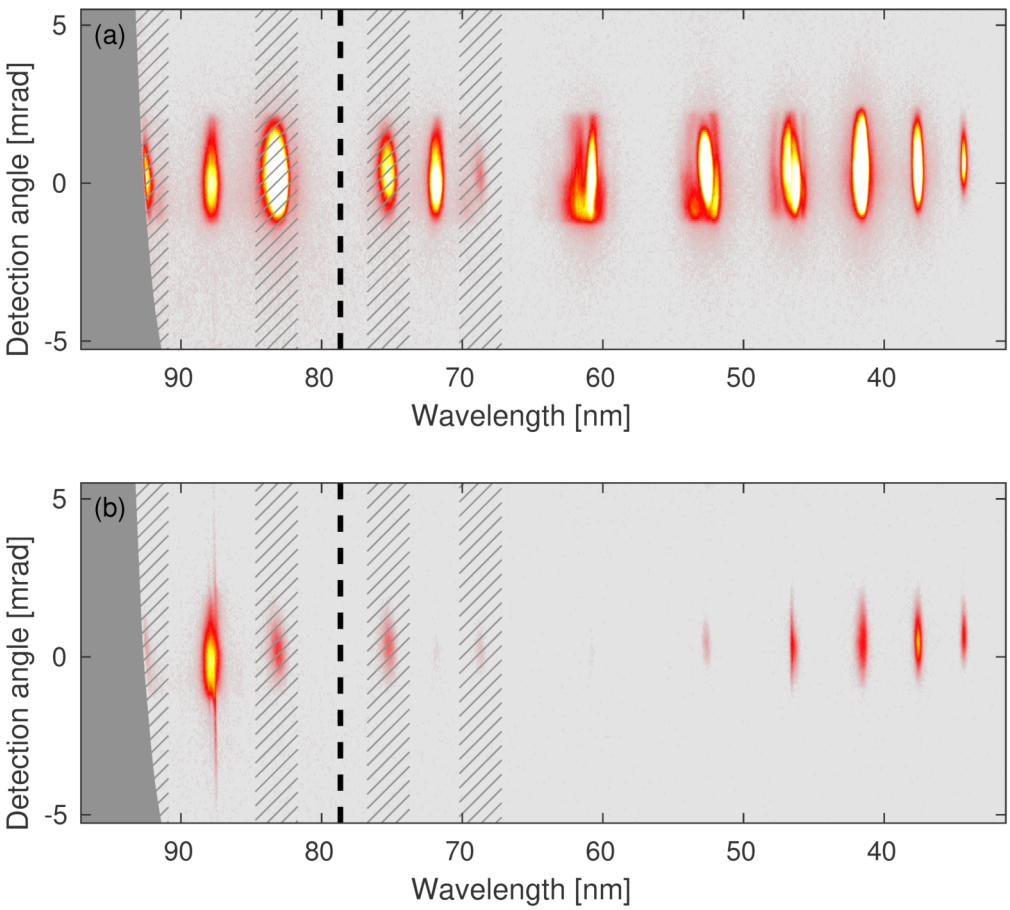

Figure 4.1: Spectroscopy of Ar. Linear color scale. (a) Spectrum from the XUV source with an iris restricting the divergence. The dark gray area shows the edge of the spectrometer screen. The second order from the grating is marked with gray hatched areas. The black dashed line marks the wavelength needed for a photon to ionize Ar. (b) Ar gas is turned on in the target gas cell with an ambient pressure of 2 μbar. The XUV with wavelengths below the ionization threshold is absorbed or reduced, and the ninth harmonic is resonant with bound states. The data were collected on 30 April 2015.

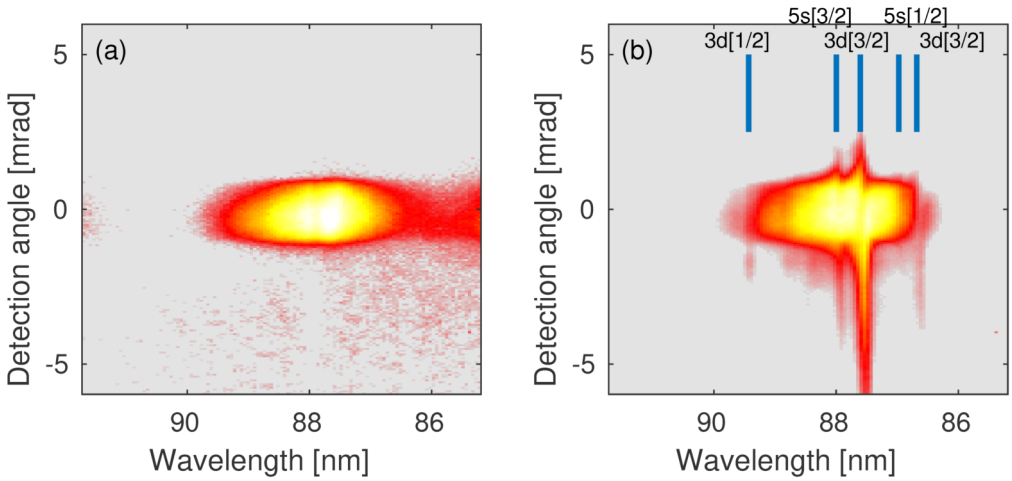

Figure 4.2: Spectroscopy of Ar. Logarithmic color scale. (a) Ninth harmonic as it comes from the XUV source without any target gas. (b) The same source but Ar as target gas with ambient pressure of 2.5 μbar. The blue lines mark the wavelength of transitions from the ground state to the 3d and 5s states with the total spin $\boldsymbol{J}$=1, which makes up the allowed transitions. The number in brackets marks the K value, the spin of the parent ion together with the angular spin for the excited electron. The two 3d[3/2] states are different in the spin of the parent ion (see sec. 3.5). The data were collected on 23 June 2015.

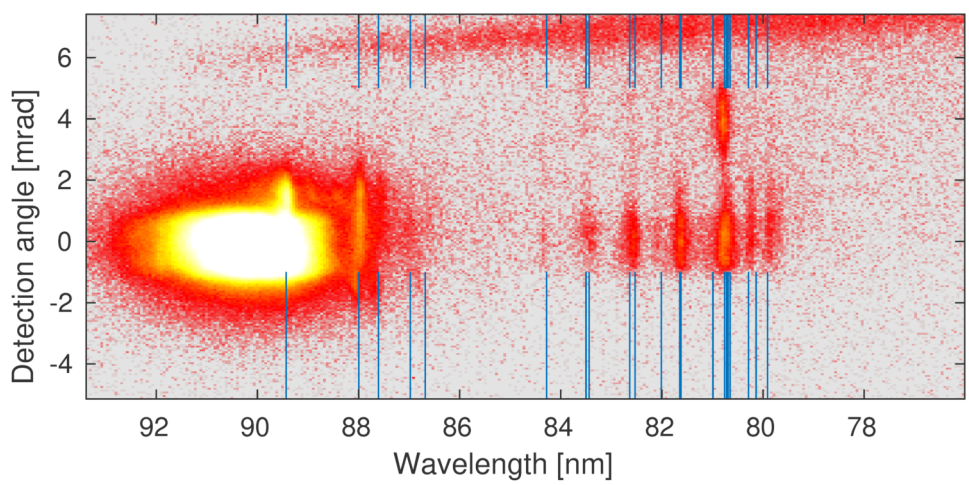

Figure 4.3: Spectroscopy of Ar. Logarithmic color scale. The blue lines mark wavelength for s and d states with $\boldsymbol{J}$=1, up to 9s and 7d. A weak IR control pulse follows the XUV pulse (see sec. 4.2). The emission lines from 84 to 80 nm originate mostly from Ar in the generation gas cell. The data were collected on 28 June 2016.

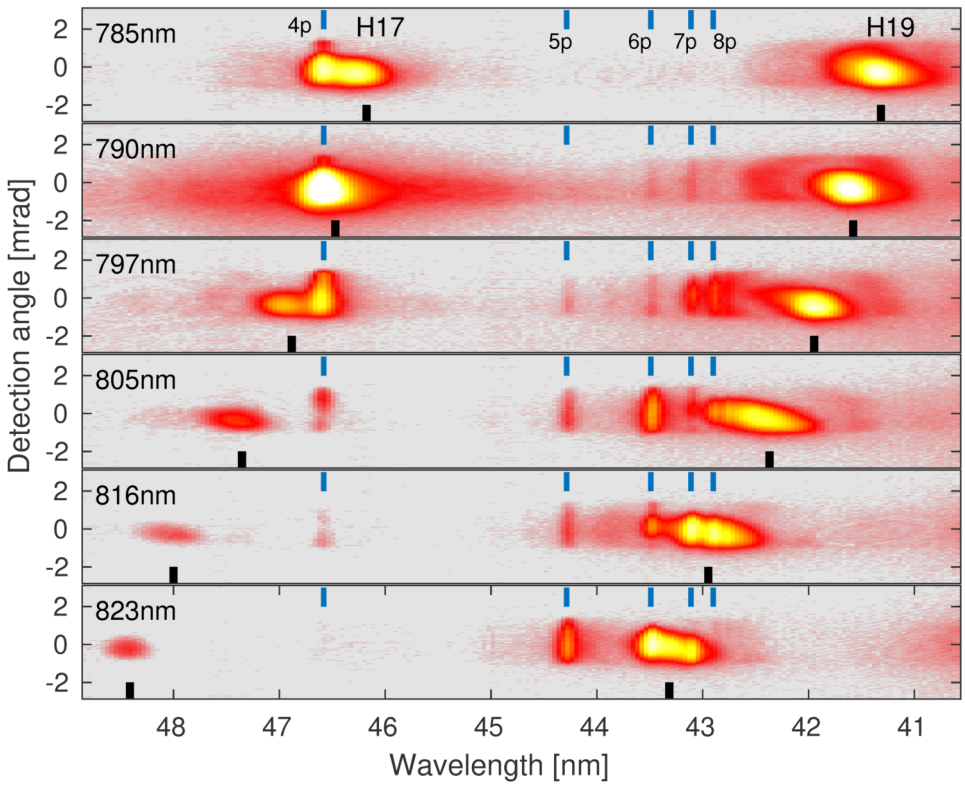

Figure 4.4: Spectroscopy of the auto-ionizing $3s3p^6np$ series of states in Ar when tuning the central wavelength generating the harmonics. Logarithmic color scale. The thick black line marks the center of the harmonics. The blue lines mark the wavelength for transitions between the ground state and corresponding auto-ionizing state (see top of figure). The ambient pressure for the target gas was 2.5 μbar. The data were collected on 16 January 2015.

4.1.2 Neon

Experimentally it turned out that Ne was the easiest target gas to obtain any signal of the emission. At full bandwidth from the laser, the edge of the 11th harmonic excites the two 3s states with $\boldsymbol{J}$=1 (fig. 4.5). Tuning the central wavelength higher to around 815 nm centers the 11th harmonic on the 3s states. These two states can be of interest, as they form a two-state system, where the emission from the two states are spectrally separable and with no other states nearby. As seen in fig. 4.5 (b), the coupling to the ground state from the 73.5 nm 3s[1/2] state is much stronger than from the 3s[3/2] state. This is seen in the stronger absorption profile, as well as in the stronger emission. This makes for an easily recognizable feature. With the harmonics tuned to a wavelength around 815 nm, the 13th harmonic excites 4s and 3d states with $\boldsymbol{J}$=1. The two 4s states can be spectrally separated and are separated in energy with roughly half of the energy difference between the two 3s states. From the three 3d states that couple to the ground state, the two with higher transition wavelengths are spectrally close together, so that we are not able to clearly separate them with our

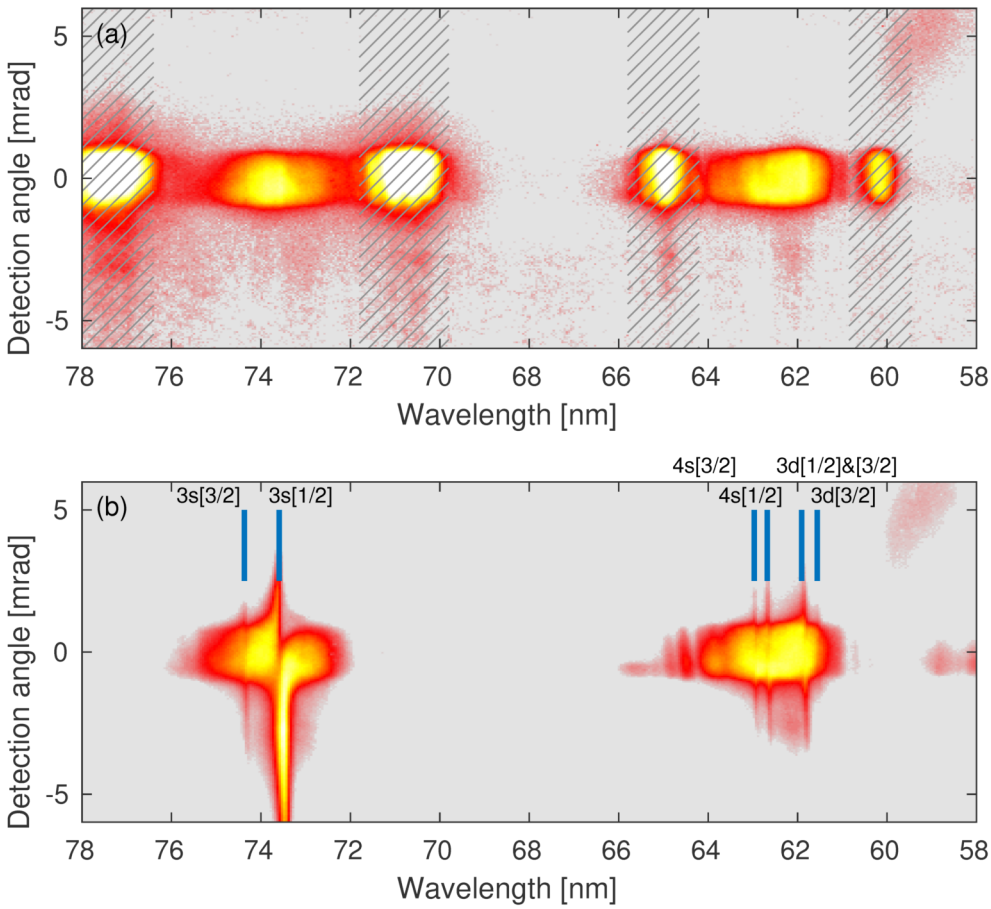

Figure 4.5: Spectroscopy of Ne. Logarithmic color scale. (a) No target gas. The fundamental IR pulse is centered at 810 nm wavelength and the 11th harmonic and the 13th harmonic from the XUV source are centered at the 74 and 62 nm wavelength. The gray hatched areas correspond to second order from the spectrometer grating. (b) Target gas of Ne with ambient pressure of 1.5 μbar. The blue lines mark wavelengths for transition between the ground and corresponding state. The two 3d states at 62 nm are not possible for us to spectrally resolve. The data were collected on 23 June 2015.

spectrometer.

In the observations of the emitted light from the atoms, it is noted that the divergence is wider than the XUV pulse. This can be experimentally used to determine when the harmonics are tuned correctly and resonant with transitions in the atom. To separate the divergence of the emission from the coupling to the ground state, the degree to which a state can be excited and emit light, a line-out of the divergence was taken from various states and normalized, assuming a Gaussian form. The same divergence was found for all states in Ne (fig. 4.6), although some of them was slightly redirected. Comparing with the divergence from Ar (not shown), the signal from 3d[1/2] state is difficult to observe, but it is possible that the states with a 3p electron

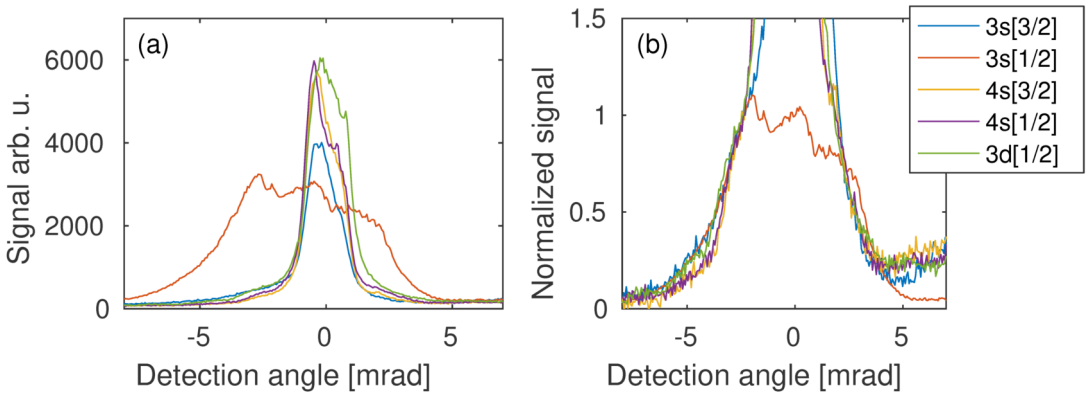

Figure 4.6: Divergence of the emission from states in Ne. The data is the same as fig. 4.5. (a) A lineout along the detected angle axis for the signal from the different states. (b) Normalized and shifted signal, to find if emission from all states share the same divergence.

excited share the same divergence as Ne. There is, however, a clear difference between that divergence and the divergence of the auto-ionizing states, which keep the same divergence as the XUV pulse (fig. 4.4). Changing the target gas pressure does not alter the divergence either, although more light is absorbed and emitted (fig. 4.7). In fig. 4.7 (g), the normalized signals all have similar divergence. As the pressure increased, however, the center of the divergence shifted to negative angles.

Even though the reason for the divergence is still unclear, it is possible to speculate. As the emitted signal is more divergent in the farfield, a change to the emission just after the excitation pulse is needed. Either a change in the spatial polarization of the atoms across the focus or in the wave front of the emitted signal.

The simplest answer is if the wave fronts became curved. If IR comes through from the HHG process, which is centered on the XUV pulse, the intensity-dependent phase shift (sec. 2.8) would have this effect. It is also likely that the phase change due to intensity is different for the long-wavelength transitions from the 3p electron and the shorter-wavelength transitions for the 3s electron to the auto-ionizing states. The other possible wave front change would be from movement of the atoms, but that would lend the same divergence to all transitions, if the difference in wavelength can be neglected. If it is not negligible, smaller wavelengths should diverge more. This does not match with observations in Ar for the lower-frequency states and auto-ionizing states.

The other possible answer is if the spatial polarization shape changes. Then the farfield signal changes as well, provided that it is given by the Fourier transformation of the spatial intensity profile of the emitted light from the target gas. With an exponential decay of the excitation, no significant change occurs in the polarization profile[2]. If, however, the decay process is not exponential the shape changes, and so does the farfield signal and thus the divergence of the emission. The smaller divergence for emission from auto-ionizing states could be explained by a different decay process for this emission.

[2]An arbitrary shape divided by a constant keeps the same shape

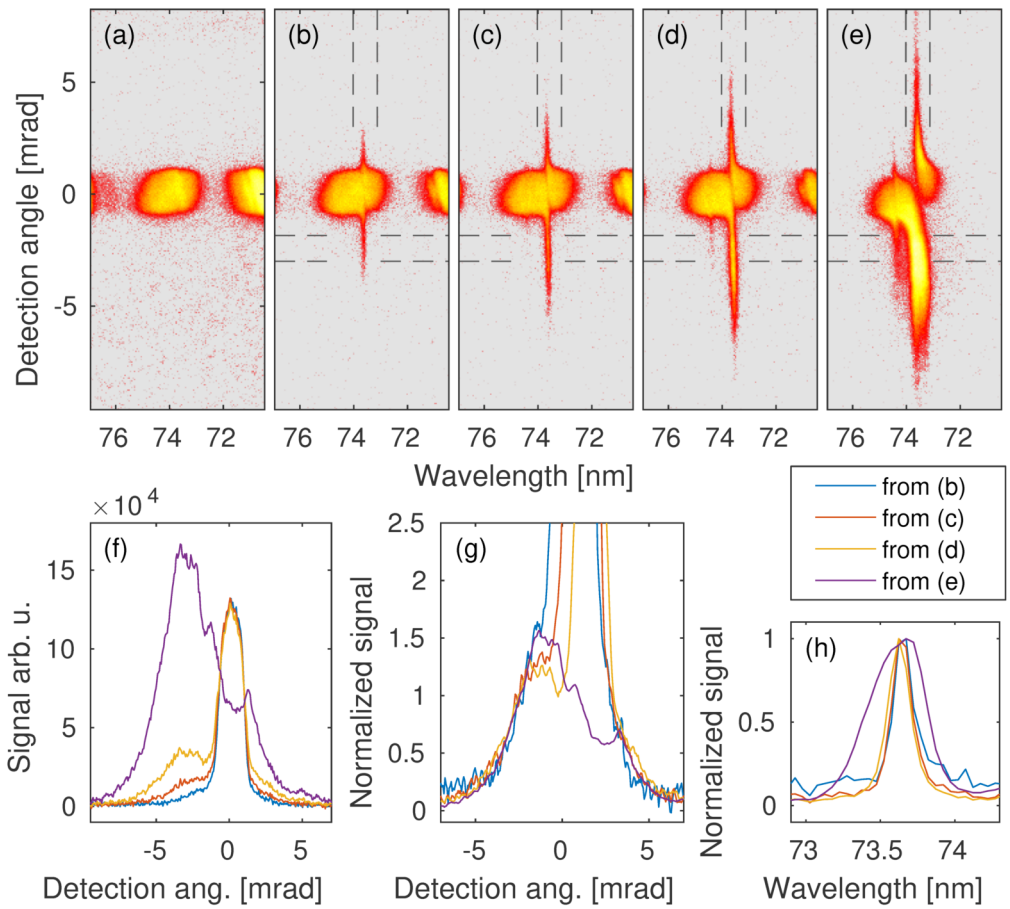

Figure 4.7: Pressure dependence of spectrum in Ne. Logarithmic color scale in (a-e). (a) No target gas, only the signal from the XUV source. (b-e) Gradually increased target gas pressure of Ne up to 8 μbar. The dashed lines show where the data in (f-h) were collected. (f) The emitted angle for different pressure. The signal is summed up between the dark dashed vertical lines. (g) Normalized and shifted data, showing no change of the divergence for different pressures. (h) Showing the normalized line width for different gas pressure. The signal is summed up between the dark dashed horizontal lines. The data were collected on 19 December 2014.

Using Ne as target gas, the effect of gas pressure on the emission is shown in fig. 4.7. The ambient pressure in the experimental chamber is increased from 0 to 8 μbar. The obvious response from more gas atoms in the beam path is additional absorption of the XUV excitation pulse, which leads to an increase in emitted light. Two observations are of interest: the divergence, as discussed earlier, and the line width. To separate out this effect, the signal for the various gas pressures is normalized. Summing up the signal for the wavelengths between the vertical dashed lines (fig. 4.7 (a-e)), the divergence of the signal is seen (fig. 4.7 (f). Shifting the center of the signal and normalizing shows that the divergence is the same (fig. 4.7 (g)). A similar approach is used for the divergence between the horizontal dashed lines, (fig. 4.7 (f)), and the line width is found to be the same for the emission in fig. 4.7 (b)-(d) but increase for the signal in (e). Most probably this is a result of propagation effects. This means that emission from atoms early in the atomic ensemble have a significant impact on emission from atoms late in the ensemble. This causes the temporal structure of the emitted signal, and thus the spectral structure, to change.

A effect of this is re-absorption of the emitted signal later in the medium. As the emission from absorbing resonances are out of phase with the excitation field, then reabsorption and consecutive emission will be π phase shifted again. For low gas pressure this second emission is negligible, however, increasing the pressure result in a stronger second emission which cancels the first emission and give a faster decay. For sufficiently high pressure the first emission will decay to zero and the second emission will be seen, which then will be reabsorbed and reemitted in a third emission and so on. This is called resonant pulse propagation and for high gas pressure the total emission acquire oscillating features. [32].

4.1.3 Helium

As the lightest noble atom, He has the highest ionization energy and is thus of great interest for electronic transitions in the XUV regime. It is also a two-electron system that theorists can solve. The first transition from the ground state is to the 2p state, corresponding to a wavelength of 58 nm (fig. 4.8). 2p is expected to Stark-shift with the opposite sign than the higher np states, which is interesting to study. Reaching this resonance would be easy with even harmonics, but for odd harmonics, it requires some tweaking. One way is to have very high intensity in the HHG process, which results in blue shifting of the harmonics. This results in a complicated HHG process and very complicated harmonics, especially the long trajectory, but as the more divergent light from the HHG process is cut with the pump iris (W2, fig. 3.2), that does not pose a problem. What might be a problem is the temporal behavior of these harmonics. This has not been measured, but so far there is no strong indication of major changes to the temporal form of the harmonics. However, this is something that should be studied.

4.2 Spatial control

So far no control has been shown, only a bit of good old spectroscopy, but with femtosecond-long XUV pulses. The fact that the atoms emit light for a long time after the XUV pulse together with the fact that the temporally short IR pulse can

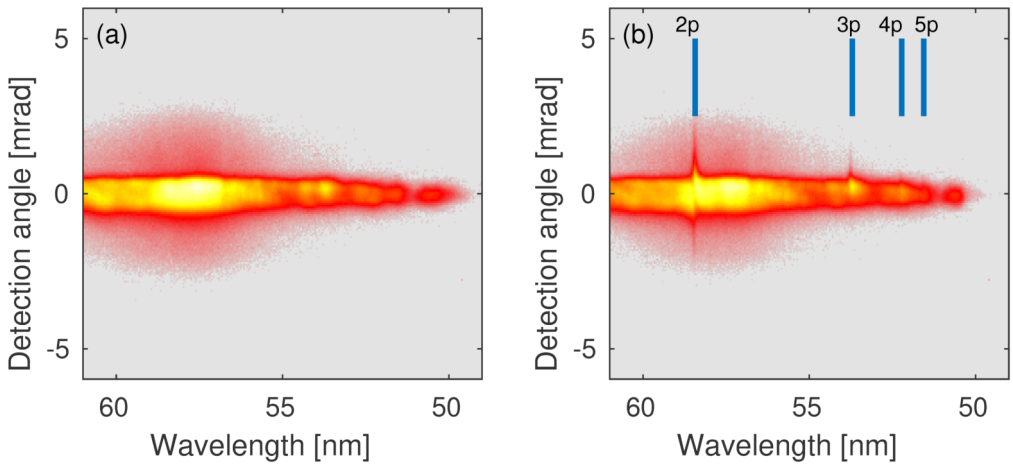

Figure 4.8: Spectroscopy of He. Logarithmic color scale. (a) No target gas. (b) He as target gas with ambient pressure of 0.56 μbar. The data were collected on 7 April 2017.

interact with the atoms and give them a phase shift (sec. 2.8), it is possible to control the spatial direction of the XUV emission from the atoms. In the following discussion, this is shown in two ways, by changing the intensity of the IR control pulse, and by changing the spatial overlap between the two beams.

4.2.1 Intensity

It is a crucial step that the intensity of the control pulse changes the phase of the emitting atoms if our understanding of the control process is correct. This should be most easily seen by applying a linear intensity gradient over the excited atoms, which then should turn the emission direction with a speed depending on the steepness of the gradient. If the applied gradient is a pulse instead, the rotation of the emission happens while the pulse interacts with the atoms, and the atoms will continue to emit in the final direction after the pulse has passed. Experimentally, Gaussian-like focus of the control pulse can be used, with a beam waist bigger than the XUV focus in the target gas. Spatially shifting the beam such that the peak of the XUV pulse is at the steepest gradient of the IR pulse, an almost linear intensity gradient is created for the excited atoms (see sec. 2.9).

This is done in fig. 4.9 for Ar. The IR beam and the XUV beam are slightly non-collinear, with an angle of 14 mrad, which can be seen in fig. 4.9 (d-e), where the intensity in the IR pulse is high enough to generate the ninth harmonic in the target gas. In the sequence of images, the emission from 3d[1/2] and 5s[3/2] states is seen at a different angle for larger intensities of the IR control pulse. Interestingly, the emission can be controlled and emitted, even though the IR pulse is intense enough to create harmonics. On the other hand, for the emission from these states to be redirected with 10 mrad from a 20 fs IR pulse, the control pulse needs an intensity of high 10^{13} W/cm^2.

In fig. 4.10, a similar experiment can be seen for He. Fig. 4.10 (b)-(e) shows a smaller part of the whole spectrum for different intensities of the IR control pulse.

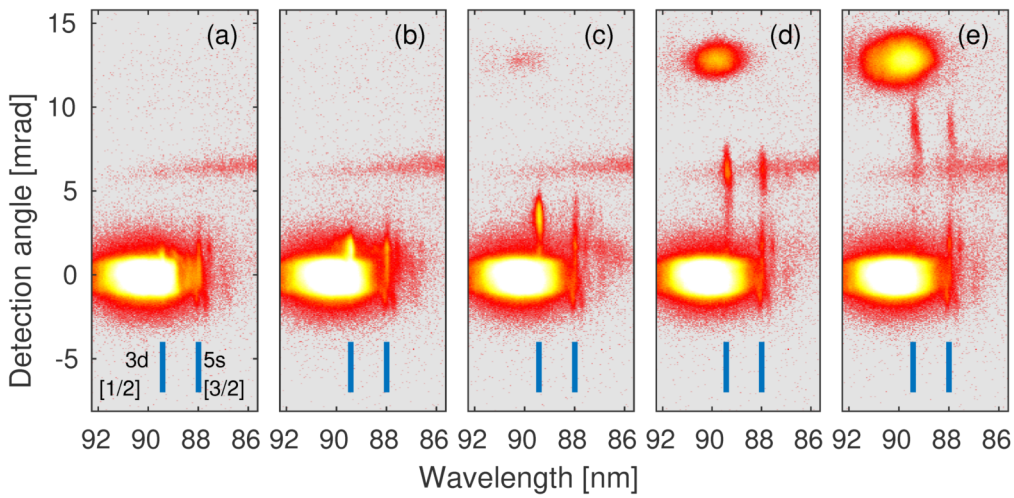

Figure 4.9: Control of direction of emitted light from Ar through change in the intensity of the IR control pulse. Logarithmic color scale. (a-e) Increased intensity of IR control pulse through opening of an iris. The blue lines mark the wavelength for 3d[1/2], and s5[3/2]. The signal at 14 mrad for (d-e) is the generation of the ninth harmonic by the probe in the target gas. The data were collected on 28 June 2016.

Most striking is the intense emission from the high np states at 50.5 nm, which for the highest intensity is both redirected and emitted with a wide divergence. If the ratio in beam waist between the XUV pulse and the IR pulse comes close to 1:2 or less, the phase change can no longer be approximated as coming from a spatial linear intensity gradient. Instead, the ensemble of excited atoms can be separated into small spatial groups, each of which experiences a slightly different intensity gradient, resulting in more divergent emission.

4.2.2 Lateral displacement

Redirection of the emission will be maximized when the ensemble of excited atoms is exposed to the steepest gradient of the control pulse. For a Gaussian-like focus of the IR control pulse, the steepest gradient is at FWHM. As the excited ensemble is created from a XUV excitation pulse, the maximum redirection of the emission happens when the IR control beam focus is spatially offset from the XUV excitation beam focus, placing the XUV beam at the steepest gradient of the control pulse.

It can be worth noting that this offset between the center of the two beams is only relevant in the target gas. If the target gas has the shape of a thin gas curtain, only the offset between the two beams at that curtain would matter for the redirection of the emission. When the gas target is thick, it is still possible to think of thin gas curtains orthogonal to the XUV excitation pulse. If the control beam and the excitation beam are non-collinear, the various gas curtains also have different offsets between the two beams, resulting in different redirection from various parts of the target gas and possibly not the desired result. Similarly, even with collinear beams but a gas target that is longer than the Rayleigh range such that the beams change

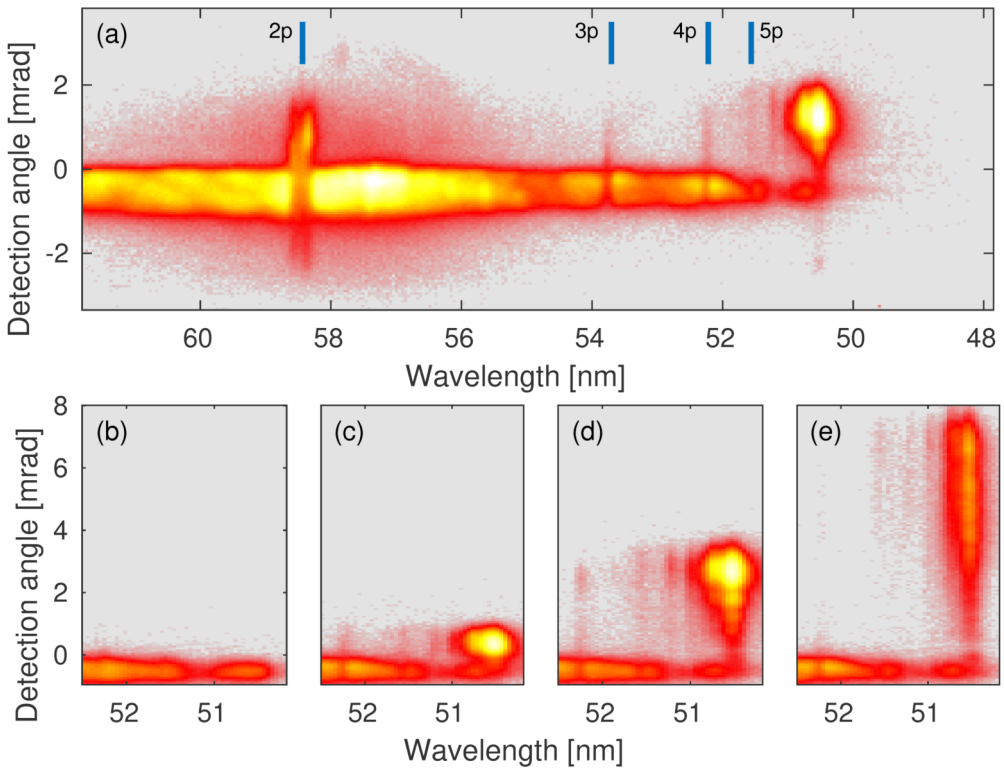

Figure 4.10: Control of direction of emitted light from He through change in the intensity of the IR control pulse. Logarithmic color scale. (a) The spectrum for He for a certain intensity on the IR control pulse. The blue lines mark the wavelength for corresponding state. (b-e) The spectrum for the states above 4p as the intensity of the IR control pulse is increased by opening an iris. The data were collected on 7 April 2017.

in size, the result is different directions of the redirected emission from various parts of the gas.

Changing this offset also alters the redirection of the emission from the atoms. In the simplest case, a scan of the offset between the beams, from one side to the other, results in a redirection of the emission that maps the intensity gradient of the control pulse, or more correctly, the integral in time of the spatial intensity gradients.

In fig. 4.11, such a scan was done in He where the motor controlling the lateral direction of the recombination mirror was scanned and thus also the position of the control pulse focus. Fig. 4.11 (a) shows the image from the spectrometer when the redirection of the emission is greatest. The signal for the np state, with n$>$ 8, between the dashed dark lines was summed up and plotted in fig. 4.11 (b) as a function of time running the motor. As the offset is scanned, the emission is redirected to one side, reaching a minimum of -5 mrad and almost disappearing until re-emerging at 5 mrad, followed by a reduced redirection. A part of the excitation pulse is not absorbed by the gas and show up at zero detection angle.

A simple model to show the redirection of the emission was developed. Atoms on a string were given a Gaussian shaped intensity, modeling the impact of the XUV

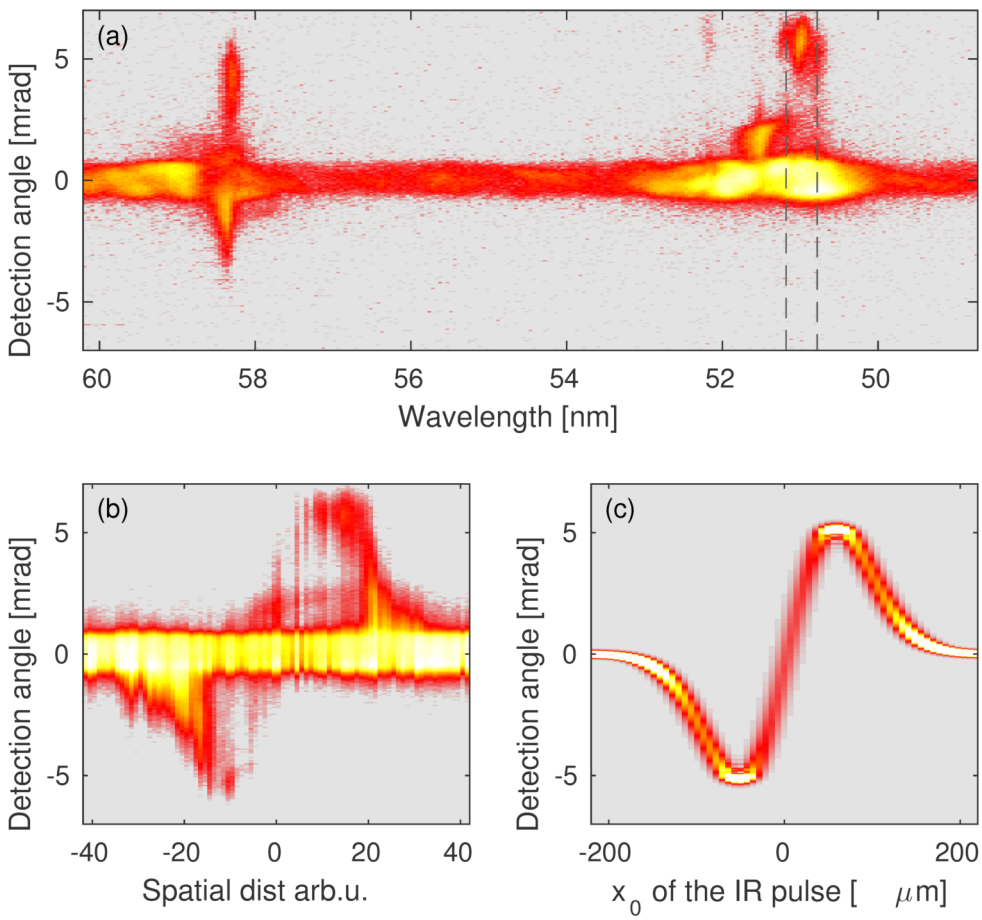

Figure 4.11: The effect on the direction of emission when shifting the offset between the beams. Logarithmic color scale. (a) The spectrum of He when the emission is redirected the most. The emission from np states that are unavailable to spectrally resolve between the dark dashed lines is summed up and shown in (b) for different spatial offsets. This is done by scanning a motor that controls the tilt of the recombination mirror, and thus the direction of the IR control pulse. The data were collected on 15 December 2016. (c) Result from a theoretical model when a control pulse with a Gaussian intensity profile is scanned spatially from one side of the XUV excitation pulse to the other. An AC Stark-shift equal to the ponderomotive energy was assumed, and the peak intensity was $1.5 \cdot 10^{14}\,\mathrm{W/cm^2}$

excitation pulse on the atoms, and then given a phase from a larger Gaussian shaped profile, modeling the IR control pulse. This was then Fourier transformed into the farfield. The results in fig. 4.11 (b) was simulated and fig. 4.11 (c) was obtained by scanning the offset between the two Gaussians, the XUV with a FWHM of 20 μm and the IR control pulse with 130 μm, .

It might be obvious but is worth mentioning again that the redirection of the light comes from change in the phase of the emitting atoms. More correctly, the phase is always connected to a specific superposition between two states. This phase of the superposition is controlled through the intensity of a control pulse. The connection between those two, the phase of the superposition and the intensity of the control pulse is the AC Stark shift, how the resonance frequency for the specific state changes with intensity in the AC field. From the exact same experiment, emissions from various states might be redirected to one degree or another as they are stark shifted differently. An effect of this is also seen for 2p in fig. 4.11 (a), where a part of the emission is shifted in the opposite direction, due to 2p shifting to lower energy as the intensity is slightly increased.

In the model for fig. 4.11 (c) a ponderomotive, linear, shift of the energy level as a function of IR intensity was assumed. This assumption should be fairly good for the high np states. To obtain a value from the theory similar to what we measure for the maximum and minimum redirection, the peak intensity of the IR control pulse in the model is $1.5 \cdot 10^{14}\,\mathrm{W/cm^2}$. As this is a very high intensity, it is not difficult to understand that the signal is reduced or gone when the peak of the IR control pulse spatially overlaps with the excited atoms. The S-shaped curve means that two different spatial offsets will give the same redirection, as the intensity gradient is the same[3]. Fig. 4.11 (b) shows that even though the redirection is the same for two spatial offsets between the beams, the higher background intensity or average intensity causes a reduction in the signal, either by ionization of the atoms or by other effects. The measurement also seems to confirm the focus of the experimental IR pulse as being Gaussian-like.

4.3 Temporal control

For full control of the emission, not just spatial but also temporal control is needed. Most of the work in this part has been done by changing the delay between the XUV excitation pulse and one IR control pulse, but a preliminary experiment with two control pulses has also been performed.

4.3.1 One control pulse

When looking into the temporal control of the emission from the atoms with one pulse, the border between control and study becomes blurred. Using a spatial overlap between the pulses that gives a clear redirection of the emission, the temporal behavior of the system is probed by scanning the delay between the XUV pulse and the IR pulse. The intensity of the redirected light is then the measured quantity. With but one control pulse, the direction of the emission changes only once. As a result, the

[3] E.g. for -3 mrad there is two possible x-values. The two spatial offsets result in the same spatial intensity gradient for the excited atoms but the one closer to zero give much higher intensity.

measured intensity is the integrated emission from the time the atoms interact with the control pulse until the end of time, which is roughly 1 ms for these transitions. If thus the energy in the atoms, or the probability of excitation in the system, is described by $\Psi(t)$, where $t = 0$ is when the XUV excitation pulse interacts with the atoms, then the emitted energy is the change of the stored energy, the time derivative $d/dt\Psi(t)$. What we measure is the integral

$$\Upsilon(\tau) = \int_{\tau}^{\infty} \frac{d}{dt}\Psi(t)dt, \tag{4.1}$$

where $\Upsilon(\tau)$ is the measured delay dependent signal. For all $\Psi(t)$ that go to zero at $t = \infty$ this equation reduces to $\Upsilon(\tau) = \Psi(\tau)$. This means that for a single transition, the perfect two-level atoms, scanning and measuring how the intensity of the redirected light changes with delay, yield the decay of the system. The signal can then be fitted with an exponential decay curve and the information extracted.

For most transitions and states, the perfect two-level atom is not the case. The physical phenomena that arise are coupling and transfer of energy between different states through the control pulse. This results in a change in energy, or probability of excitation, for the various states that not only depend on the time since excitation, but also the delay to the control pulse, $\Psi(t, \tau)$. It is then no longer possible to exactly retrieve the temporal evolution of Ψ with our measurement. If, however, the coupling to other states is cyclical and weak, then it is possible to retrieve a decay that is slower than the oscillation period by comparing the ways the (slow) amplitude change.

As the delay is increased, the superpositions evolve in time, both with the phase and with the emission, or de-excitation (compare eq. 2.19). It is the evolution of the phase of the superposition that gives the oscillatory behavior of the IR control pulse interaction. With two states that are closer than the bandwidth of the IR pulse, the IR can act as a mediator and transfer energy from one state to the other through a two-photon process. The end result of this type of Raman process, which way the energy flows, depends on the phase difference between the two states that are involved and the phase difference of the two photons that couple them. As time goes by, the phase difference between the two photons does not change, as they are from the same pulse, but the phase difference between the states changes, due to difference in transition frequency down to ground state for the two states. This system can be expressed by

$$|\alpha\rangle\, e^{i2\pi\nu_\alpha t} + |\beta\rangle\, e^{i2\pi\nu_\beta t}, \tag{4.2}$$

where ν_α and ν_β is the state specific frequencies. Changing the phase difference with π transfers the energy in the opposite direction when interacting with the IR pulse, and this process is repeated after the time it takes for the two states to differ by 2π. This time is thus given by

$$T_{period} = \frac{1}{(\nu_\alpha - \nu_\beta)}. \tag{4.3}$$

This will result in out-of-phase oscillatory behavior in the intensity of the emitted light as a function of delay between the pulses, with an oscillation period that is inversely related to the difference in frequency between the states. If there is a third state that is approximately resonant with the other two states through the IR field, energy can be transferred to that state. Tuning the resonance frequency of this third state slightly changes the way that energy is transferred. In the extreme case, energy is transferred

only between the two lower states and the third upper state, causing the oscillations in the intensity of the emission from the lower states to be in phase with each other.

In fig. 4.12 a delay scan of Ar is shown. The intensity and spatial offset of the IR control pulse was chosen to give a clear redirection of the emission, without too high losses in the intensity (see sec. 4.2.2). In fig. 4.12 (b), the signal emitted with a detection angle between the dashed lines in (a) is summed up and displayed as a function of the delay between the pulses.

The sum of the signal for the three lowest transitions, at 89.4 nm (3d[1/2]), 88 nm (5s[3/2]) and 87.6 nm (3d[3/2]), is plotted in fig. 4.12 (c-d). The oscillations in the intensity between the 5s[3/2] and the 3d[3/2] state is clear. They are not entirely out of phase and have a period time of about 80 fs. This corresponds to a frequency difference that is slightly less than the expected value for the states but may be within error bars (13 THz vs. 15 THz).

When the two pulses, the XUV excitation pulse and the IR control pulse, overlap in time, the signal is further complicated. More states are Stark-shifted into resonance and emit light while the resonance frequency is changing, on top of multiphoton transitions. In fig. 4.12 (b) at zero delay, strong emission can be seen almost continuously from 88 to 90 nm, even for this off-axis angle. The off-resonant emission signal, for example at 90 nm, has a 1.35 fs modulated signal which corresponds to a 2ω modulation, with a temporal FWHM of about 20 fs (not shown explicitly). Temporal overlap effects are also seen in the signal from 3d[1/2] (fig. 4.12 (c)) which shows a Gaussian peak at zero delay.

The measured decay curves are fitted with the model described in sec. 3.6. As the uncertainty of the fit is quite high, due to the other interactions from the control pulse as discussed above, it is better to discuss the decays in terms of either order of magnitude or comparison. That said, all emissions from the atoms that we measure decay on the timescale of femtoseconds. The decay of the 3d[1/2] state (fig. 4.12 (c)) is also much faster than the decay for 5s[3/2] and 3d[3/2] (90 fs versus 200 fs in this experiment).

4.3.2 Phase control versus four-wave mixing

Multiphoton effects occur when more than one photon is involved in a light-matter interaction, such as absorption of light, or emission of light. One such effect is four-wave mixing, where the momentum and energy are conserved and three photons give rise to a fourth. In the type of experiments in this thesis, such a mix could be between one XUV photon and two IR photons in different ways. This has been observed by Cao *et al.* [8], where they have a non-collinear setup with a IR pulse and a XUV pulse, similar to our setup. They observe emission from resonant states in the XUV that occurs through four-wave mixing, both with the initial emitted XUV photon plus two IR photons resulting in a higher frequency XUV photon and with the initial emitted XUV photon minus two IR photons resulting in a lower frequency XUV photon. As the momenta are conserved, the angle between the beams gives the direction of the four-wave mixed emission.

In fig. 4.13, a delay scan with Ne is shown. The resonant 3s and 4s states have a frequency difference corresponding to roughly two IR photons and are thus possible to target with one harmonic each, the 11th and 13th harmonic (see fig. 4.5). In fig. 4.13 (a) the spectrum of the 11th harmonic is shown and the blue lines mark the wavelength

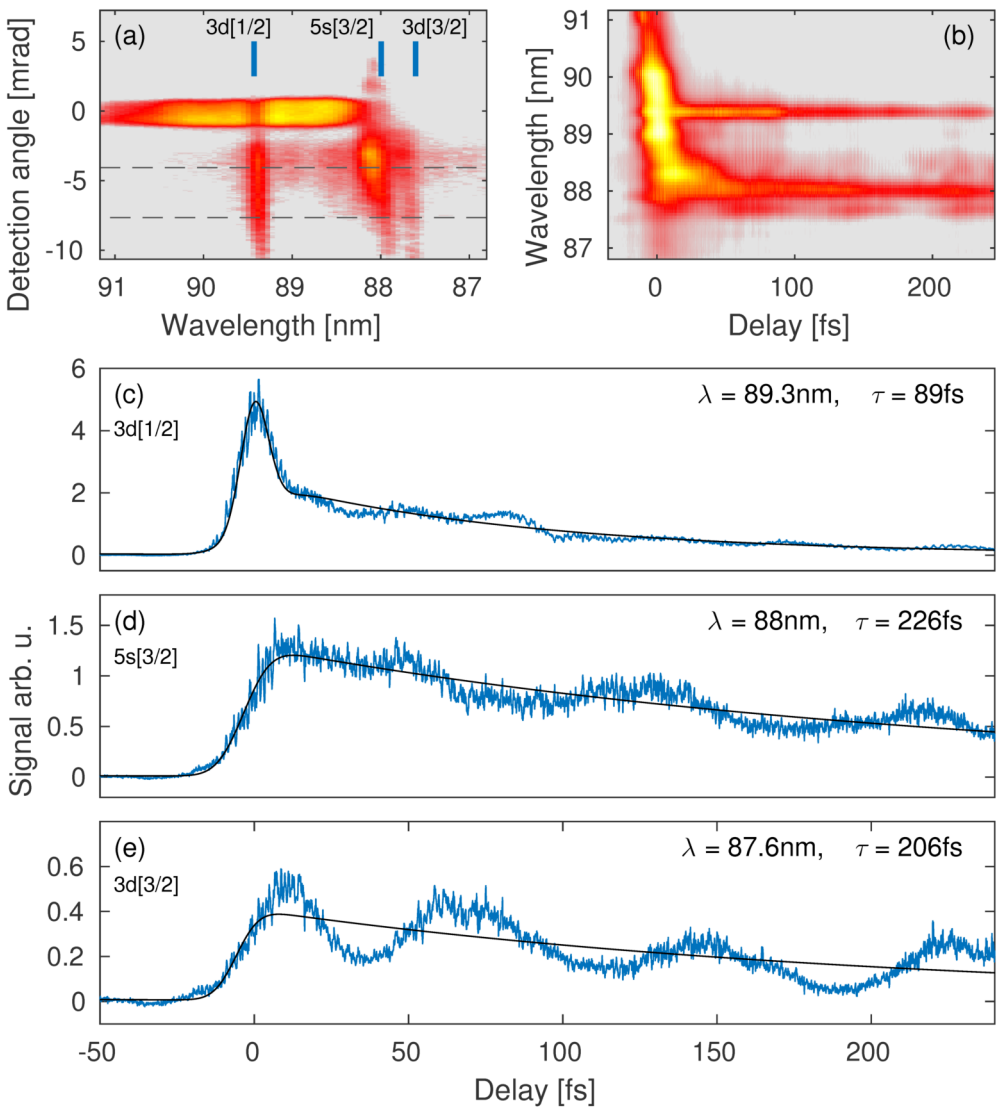

Figure 4.12: Delay scan in Ar. Logarithmic color scale. (a) Spectrum of Ar with the blue lines marking the states and the dark dashed lines where the signal was summed up for (b). (b) shows off-axis signal as a function of delay between the two pulses. (c-e) Line-outs from the data in (b) for the three states. The signal is also fitted and the decay time for that fit, τ, is given. The ambient pressure in the target chamber was 2.5 μbar. The data were collected o 23 June 2015.

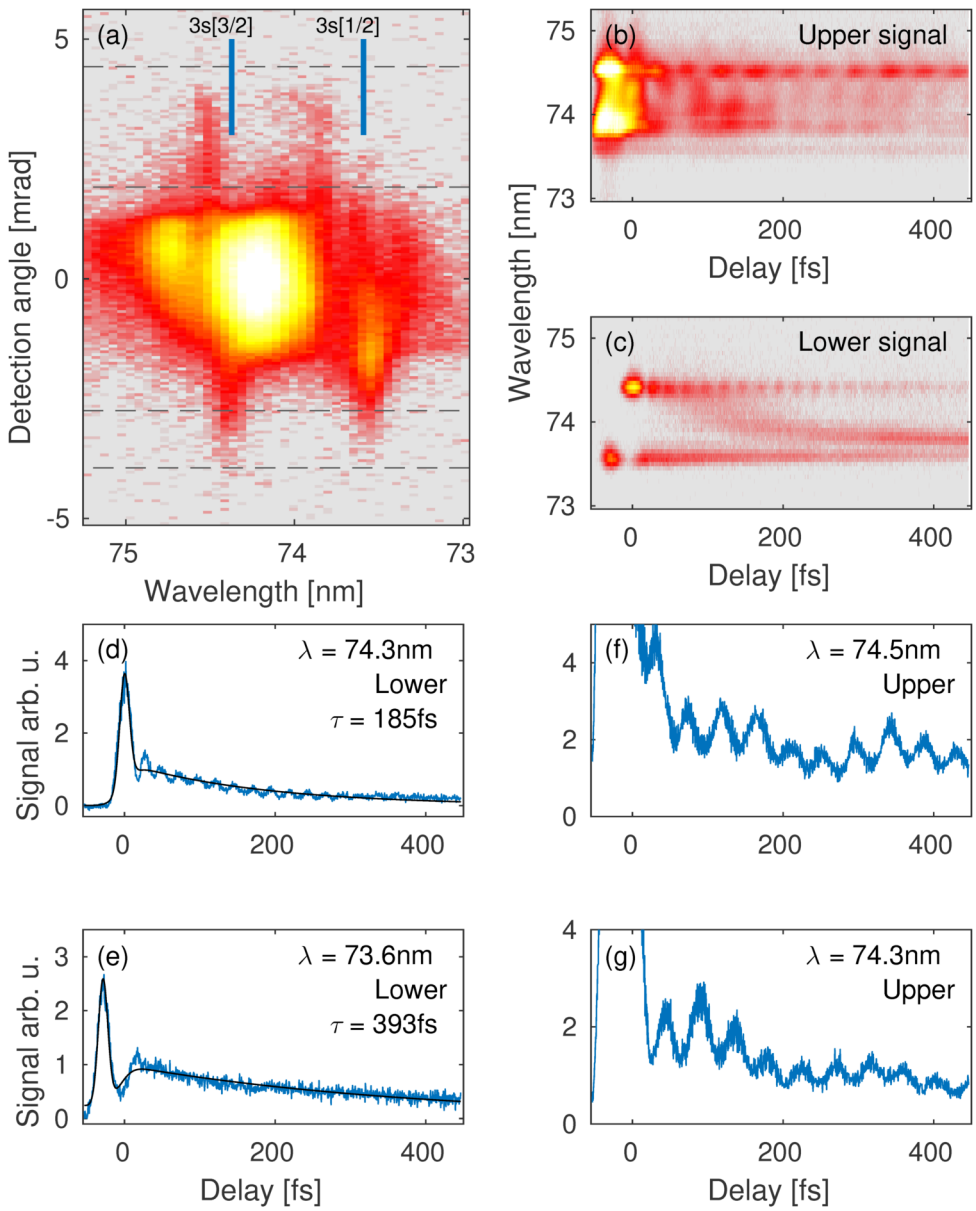

Figure 4.13: Delay scan for Ne. Logarithmic color scale. (a)The spectrum for Ne centered at the 11th harmonic. The blue lines mark the wavelength for the corresponding state. The two upper dark dashed lines mark the region where the signal for (b) was taken. The lower two dark dashed lines mark where the signal in (c) comes from. (b-c) Signal as a function of delay between the pulses. (d-e) Line-outs from (c) for the specified wavelengths. This corresponds to the wavelengths of the states. (f-g) Line-outs from (b) for the specified wavelengths. The ambient pressure was 1 μbar. The data were collected on 8 July 2016

of the two 3s states. The spectrum is taken with a delay of 23 fs, the IR control pulse just after the XUV excitation pulse. From the bright harmonic around 0 detection angle, signals seem to be emitted, both above and below. In fig. 4.13 (b) the signal with an emission angle between the two upper dashed lines is summed up and shown as a function of delay between the pulses, and the same is done for fig. 4.13 (c) and the two lower dashed lines. The two plots show large differences in how the emission varies with delay. In fig. 4.13 (d)-(g) two line-outs from the lower signal, (c), and two line-outs from the upper signal, (b), are plotted. In both of the upper, an oscillation can be seen that shows two states coupled together through the control pulse. The period time is about 45 fs, which corresponds to two states with a frequency difference of 22 THz and the signal is out of phase between the two line-outs. For the lower signal, the oscillation is faster with the period time of around 24 fs, which corresponds to a frequency difference of 41.5 THz between two states; however, no corresponding oscillation is found to the $\lambda = 74.3$ nm signal.

The difference in frequency between the two 3s states is 42.85 THz. Thus, the lower signal is expected to be the redirection of the emission from these states through the intensity-dependent phase shift of the atoms. What about the upper signal? The difference in frequency between the two 4s states is 22.15 THz, roughly half the difference between the 3s states, which matches the period time of the upper signal. As a result, the upper signal comes from four-wave mixing between a photon from 4s and maybe 3d states minus two IR photons from the control pulse, resulting in an emitted wavelength almost at the 3s states. Another way to experimentally separate the two effects is by changing the intensity of the control pulse. The signal from four-wave mixing then changes in intensity, but not in the emitted direction, while the intensity-dependent redirected emission changes direction. Nor will moving the offset between the beams give any S-curve for the four-wave mixing signal.

4.3.3 Pressure dependence

Continuing the emission of higher energy states, fig. 4.14 shows control of the emission from the auto-ionizing $3s3p^6np$ states in Ar. The laser is tuned such that the 19th harmonic is resonant with the 7p transition. The bright redirected window resonance is clearly seen in the spectrum in fig. 4.14 (a). This depicts the emission from the 7p (43.1 nm) state when the IR control pulse follows the XUV pulse and the emission from 6p and 8p is vaguely seen on each side of 7p.

Shown in fig. 4.14 (b) is the 43.1 nm emission, the wavelength of 7p resonance, and the way that the direction of emission changes with delay between the IR pulse and the XUV pulse. Most of the light at this wavelength is redirected with the control pulse (the shift from 0 mrad to −2 mrad). In fig. 4.14 (c) the same delay experiment is performed, but with lower target gas pressure. The result is that most of the light is not redirected.

This can be understood in the following way. When the coherent state of the XUV excitation pulse goes through the gas, all atoms have a small probability to be excited. With N times more atoms in the way, N times more energy is lost from the excitation pulse. The energy absorbed by the atoms is then emitted, and this is the light that is controlled and redirected. What is seen for the lower gas pressure in fig. 4.14 (c), is that most of the energy is left in the excitation pulse.

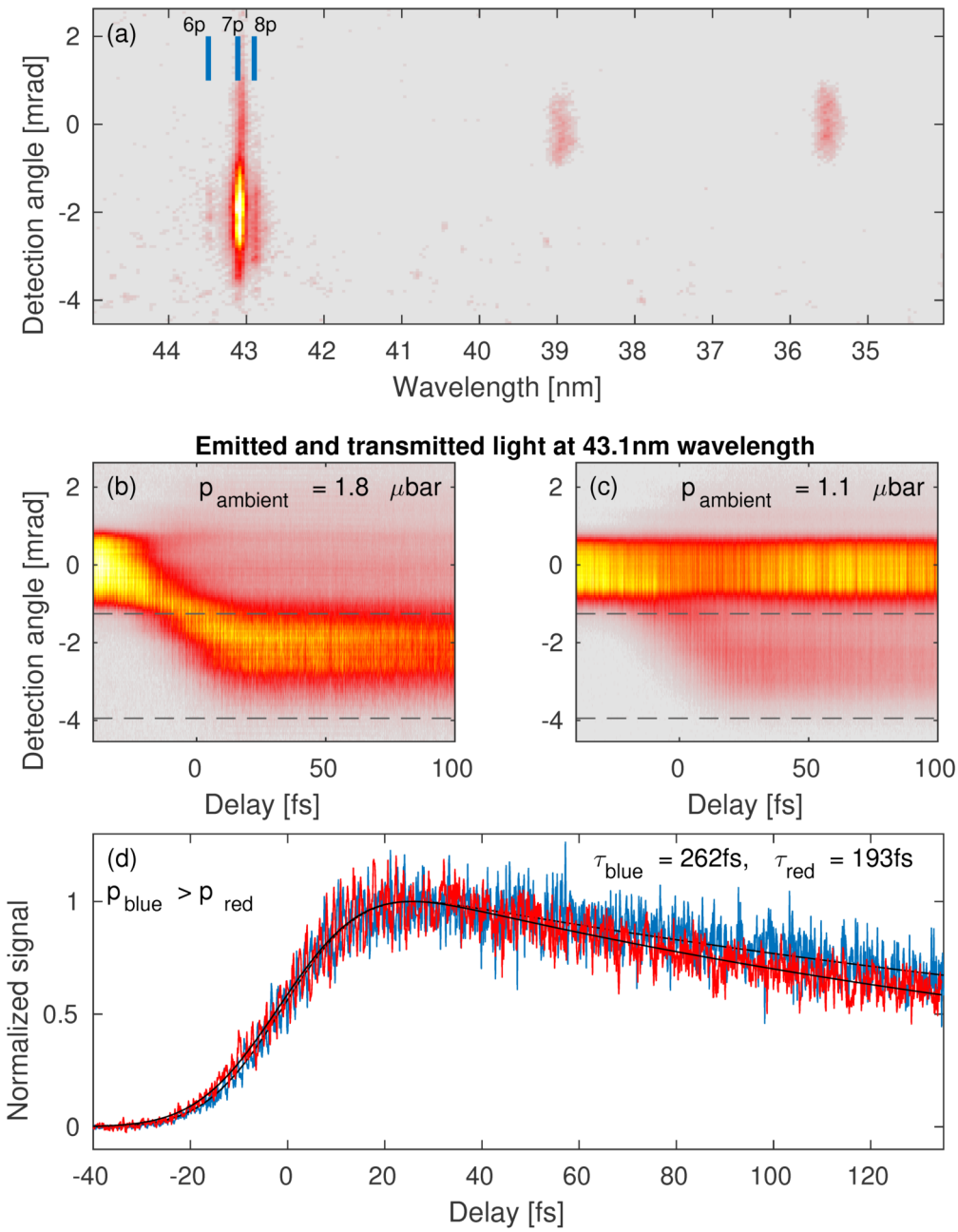

Figure 4.14: Delay scan for $3s3p^6 7p$ state in Ar. Linear color scale. (a) Spectrum from Ar with the IR control pulse 50 fs after XUV excitation pulse. The blue lines mark the wavelengths of corresponding state. 21st and 23rd harmonic can vague be seen at 39 nm and 35.5 nm, being mostly absorbed by the gas. (b-c) Emitted and transmitted light at $\lambda = 43.1$ nm as a function of delay between the pulses. (d) Normalized lineouts, summing up the signal between the dark dashed lines in (b-c). The blue curve is from (b). The data were collected on 25 June 2015.

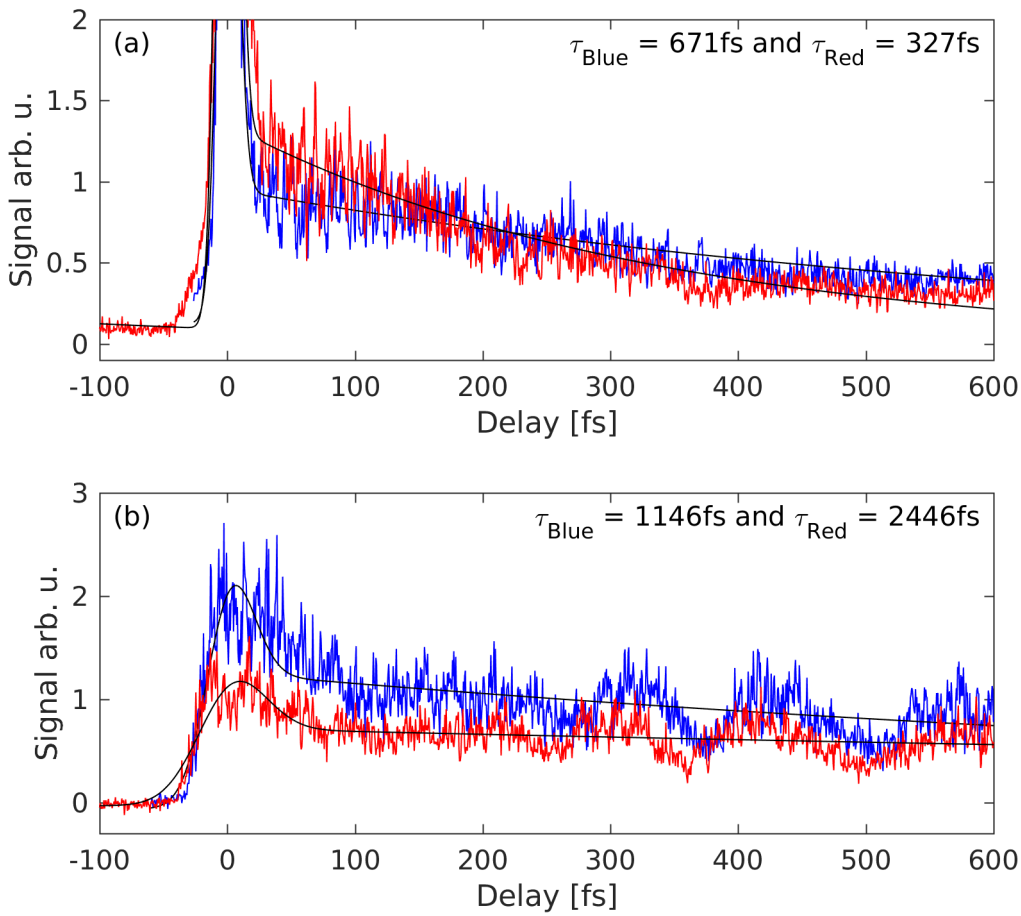

Figure 4.15: Line-outs from delay scans in Ar with two different pressures. Blue curves have an ambient pressure in the chamber of 1.9 μbar, and red curves have 2.9 μbar. (a) Signal as a function of delay for 3d[1/2] state. (b) Signal as a function of delay for a sum of high np auto-ionizing states. The data were collected on 30 October 2015.

The decay of the off-axis signal is seen in fig. 4.14 (d). Here, the light emitted with a detection angle between the dashed lines in fig. 4.14 (b) and (c) is summed up and the background remove and the signal is then normalized for the highest value. The blue curve corresponds to the higher target gas pressure. The most striking feature, after observing the other delay scans, might be the absence of oscillations and other interactions from the control pulse. Fitting the curves gives decay times with 260 fs for the blue curve and 190 fs for the red curve, but the uncertainty is high. Still, there is a small indication that higher gas pressures gives longer decay times for this state.

This is further explored in fig. 4.15, where two consecutive delay scans with Ar for various target gas pressures are shown. The summed-up off-axis signal for 3d[1/2] with the background removed are shown in fig. 4.15 (a) and similarly in (b) for high np auto-ionizing states that were not spectrally separable. The data were treated equally, with the only difference being varying pressures. For the blue curves, the

ambient pressure in the chamber was measured to 1.9 μbar, and for the red curves, the pressure was 2.9 μbar. In the experiment with the lower pressure the delay jumped back once -140 fs in the middle of the scan. The overlapping part was removed before plotting.

This experiment is not as unaffected by the control pulse as fig. 4.14. In fig. 4.15 (a), it also seems as if the decay changes with time and is faster in the beginning than the end. As the delay scans are much shorter than the decay, together with energy transfer, it is difficult to draw any conclusions. Even with the high uncertainty about the decays, the data seem to indicate that for the low bound state in Ar, increased pressure reduces the decay time, while the opposite happens for the auto-ionizing resonances. This needs to be researched more.

4.3.4 Two control pulses

To increase the control of the redirected light, a natural step is to increase the number of control pulses. As a first step, a preliminary experiment was conducted with two control pulses to create a 200 fs long XUV pulse of the emission. Two control pulses were created by delaying half of the IR control pulse with a 130 μm thick glass plate. This resulted in two control pulses with about 250 fs between them. The delay scan is shown in fig. 4.16 with Ar as target gas. In fig. 4.16 (a) a spectrum image with the two IR control pulses before the XUV pulse is shown. The ninth harmonic goes through the gas and nothing is redirected. At a later delay, one control pulse is before and one is after the XUV pulse, resulting in the redirection of the emission from 3d[1/2] with about 2 mrad (fig. 4.16 (b)). In fig. 4.16 (c), both control pulses follows the XUV pulse, one just after, redirecting the light a bit less than 2 mrad, and another after 250 fs, redirecting the emission further, with a bit less than 2 mrad. The two-phase changes add up and result in a signal redirected with 3-4 mrad. The signal from 89.3 nm as a function of delay between the XUV pulse and the two IR control pulses is shown in fig. 4.16 (d). Much of the XUV excitation pulse is transmitted through the gas. When both control pulses follow the XUV excitation pulse, an oscillatory behavior is also seen in the signal around 4 mrad, but it is unknown where this comes from.

The signal with a direction of the emission between the dashed lines is summed-up and shown in fig. 4.16 (e). Into this direction the emission is redirected with the first control pulse, and as the second control pulse hits the ensemble, the emission is sent in another direction. Thus, when both control pulses arrive after the XUV excitation pulse, a XUV emitted pulse is sent in this direction. As the measured signal is the integrated emitted light, together with some energy transfer from IR control pulse coupling, the created pulse and its temporal structure are not easily seen. Ideally, however, both the temporal structure of the emission and the total energy in the pulse are measured in the data.

The temporal structure of the emission from the atoms during the first 250 fs should, in the case of no interaction between the IR control pulse and the population in the states, be given by the derivative of the signal between 0 and 250 fs. However, some modulation to the emitted intensity clearly happens, making the fit of an exponential decay very uncertain.

When both IR control pulses are following the XUV excitation pulse, for delays longer than 250 fs, the signal detected at this detection angle is the integrated emitted

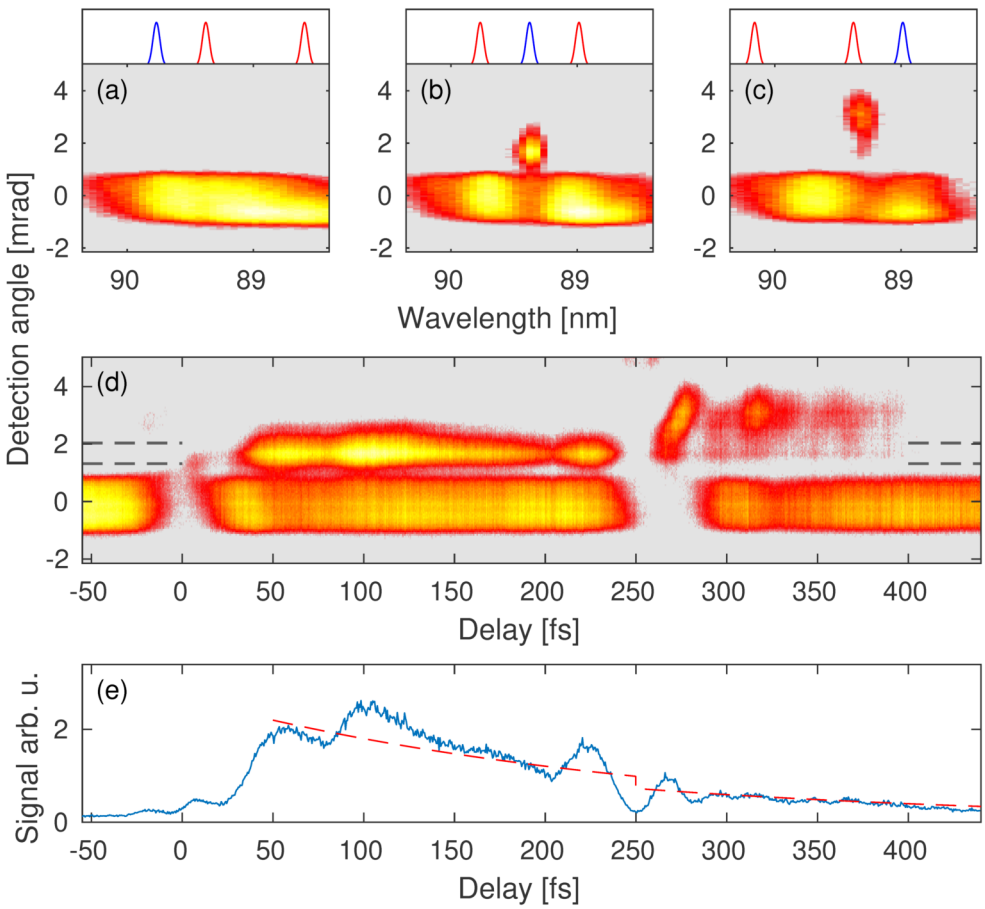

Figure 4.16: Delay scan in Ar with two control pulses. Logarithmic color scale. The ambient pressure in the chamber was 7 μbar. The spectrum when the XUV pulse comes (a) after, (b) between , and (c) before the two IR control pulses are shown (the small inset above illustrating the order of the pulses). (d) The emission at 89.3 nm as a function of delay between the two pulses and the XUV excitation pulse. (e) A line-out from the summed up signal with a emissioin direction between the dark dashed lines. The red dashed line shows a possible shape of the signal for the delay scan of two control pulses that create an XUV emission pulse from an ensemble decaying exponentially with a decay time of 250 fs.

pulse energy. Increasing the delay between the excitation pulse and the two control pulses gives more time for the atoms to decay and lose energy. Thus the amount of energy sent from the atoms during the first 200 fs after excitation will be more than the energy during 200 fs later after excitation. This assumes that the decay is exponential.

In 4.16 (e), the red dashed line is given as assistance to understand the data. Between 50 and 250 fs, it shows the shape of integrating an exponentially decaying signal with a decay time constant of 250 fs from τ and to infinity. After 250 fs, the red line shows the integral of the same exponentially decaying signal from $\tau - 200$ and to τ. For the red dashed line to fit better, the signal was reduced by 40% after the 250 fs mark. Why the intensity in the created pulses should be reduced is unclear but not unthinkable.

The shape of the data and the red dashed lines show similarities. For the experimental conditions, a delay between the two control pulses of 250 fs results in almost as much energy in the emitted pulse shown in (e), as in the emission redirected to 3-4 mrad. With less delay between the two control pulses, the step at 250 fs is thus expected to be larger as the pulses have less energy.

To conclude this chapter, we are able to control the XUV emission from an ensemble of atoms and have been able to form a 200 fs XUV pulse.

Chapter 5

Conclusion and Outlook

In this thesis we have demonstrated a method to control XUV light in both space and time and present some initial experiments on temporal dynamics on the emission from noble atoms. Based on the results in this thesis, two paths forward can be discerned where further research is needed. One focuses on fundamental physics and characterization of emission, and the other focuses on the technical challenges to improve control of coherent XUV light. The first path is possible with the present setup, while the second path pushes more towards future use and research, with for example a well-timed XUV-IR pump-probe with FELs, or two XUV pulses with controllable delay between them.

5.1 Fundamental physics

With the tools that we have developed, in particular two properties of the atomic states can be well characterized. The first is the temporal dynamics of the emission. The second is the AC Stark shift, the way that the resonance frequency of different states changes with the intensity of an AC field.

Two questions concerning fundamental physics and time-resolved spectroscopy are "How fast does the emission decay?" and "What is the underlying physical process?" These questions have been raised in this thesis and research on some transitions in noble gases has been performed. The delay scans made possible with the setup presented in the methods chapter fulfills what is needed to measure the decay time from many transitions, with the possibility of long range, up to a couple of picoseconds, and a possible precision of less than 100 attoseconds. The use of a redirected emission also results in good signal to noise. This should also be seen as another possible way to measure emission and lifetimes from more complicated atoms and molecules than the noble gases.

As for the continuation of the temporal dynamics measured in this work, the auto-ionizing $3s3p^5np$ series would be straightforward to study more, as they show no coupling effects between the control pulse and the population in the states. A detailed study of temporal dynamics and how they depend on pressure to confirm whether the indication from the presented results, increased decay time for greater pressure,

is correct. Similar states in Ne should also be fairly straightforward to measure the decay times for.

When characterizing the dynamics of lower bound states, the dynamic measured is the sum from the decay process and coupling to other states with the IR control pulse. Both of these processes are interesting to characterize further. For the decay process, the pressure dependence would be of interest, and for coupling to other states, control of the phase and characterization of the process might offer the possibility of controlling superposition between the states.

The other property of the atoms that our measurements are sensitive to is the AC Stark shift of the resonance frequency for different intensities. In the more specific cases with stronger bound electric states, this is not at all a trivial thing to calculate. For He, the shift of the lowest state does not behave at all like a polarization of a free electron, and measuring this effect enables a comparison with theoretical calculations. The measurement of this property for different states is performed by determining how much the emission is redirected as a function of intensity.

5.2 Improving Opto-Optical Modulator

We have shown that with a Gaussian focus of the IR control pulse, the beam direction can be controlled. The direction of emission depends on the spatial intensity gradient over the excited ensemble. By changing the delay between the excitation and control pulse, the time of redirection of the emission is controlled. Furthermore, the last thing in the results chapter was increasing the number of control pulses to two and shape an emitted XUV pulse. What is the next step toward controlling XUV light with an opto-optical modulator?

5.2.1 Spatial control

As we saw in sec. 2.9, the spatial control can be seen as an imprint of the integrated spatial intensity such that for atoms at $z = 0$ the change in the phase is

$$\Delta\phi(x, y, 0) \propto \int E_0(t, x, y, 0)^2 dt. \tag{5.1}$$

Thus, improving control of the intensity profile of the IR control pulse in the gas improves spatial control of the XUV emission. There are probably a number of good methods, but I will mention only one, which can be implemented in various ways.

One method to shape the intensity profile of the IR pulse in the focus is by controlling the spatial phase of the beam. If various spatial components of the beam before focus have different controllable phases, the intensity profile in the focus will be controlled as well.

In the simplest case, the control beam is split in two. Changing the phase such that they are out of phase with each other[1] does not affect the intensity profile of the beam before focusing. At the focus, however, the two fields overlap at a small angle and create an interference pattern. With the two fields out of phase, the intensity in the center will be cancelled, leading to an intensity profile that is the opposite of the Gaussian focus in the middle, a valley instead of a hill.

[1] For example with two thin glass plates, one for each part of the beam, set at different angles.

Increasing the complexity by splitting the beam into smaller spatial components with individual phases increases the ability to shape the intensity profile. As they become smaller, one problem might be diffraction. The way to ensure different phases of the beam is to change the optical path length for various parts in a controllable way. These devices are generally called spatial light modulators (SLMs) and can be divided into two groups: reflective and transmissive. The reflective group seems to enable better phase control in our wavelength regime and would be of great interest to implement in our setup.

5.2.2 Temporal control

With the temporal control demonstrated so far, we are able to decide when in time to redirect the decaying emission. Furthermore, a preliminary experiment was performed with two control pulses, which created a 200 fs XUV pulse of the emission. With one XUV pulse, XUV pump - IR probe with high temporal control is made possible. With two XUV pulses that can be shaped with both phase and amplitude, the step to ultrafast quantum optics is not very far.

Since the delay between different control pulses is in the range of femtoseconds, all control pulses need to originate from the same pulse. The preliminary experiment was performed by delaying half of the IR control beam with a higher index of refraction material (glass), but for further experiments, the delay between the IR pulses should be adjustable. This can be done either in an inline configuration, where the various beams co-propagate, or with spatially separated paths. The inline method works very well for fixed delays and should give better stability, but the problem is to adjust delay. With spatially separated beams, the delay can be adjusted with linear translation stages, and individual adjustments to the polarization state of the beams can be made.

Splitting the short control pulse into multiple ones with tunable delay between them is a first step towards temporal control. The pulses can be split using normal beam splitters. A drawback is that during recombination of the different paths, half of the power is lost. A better way is to split the pulse with a half-wave plate and a polarization beam splitter. The pulses then retain the beam shape and no pulse energy need be lost, as well as enabling adjustment of the energy ratio between the split beams.

To control the phase of the XUV emission at a later stage, the phase control pulse needs to cover the same duration as the emitted XUV pulse. For example, if the XUV emission should have a pulse shape 100 fs long, with arbitrary phase, phase control for the whole XUV pulse requires an IR control pulse to have at least the same duration. The temporal shape of the phase control pulse, and thus the changes in the phase of the XUV pulse, can be sculpted, for example, with an SLM in an optical chicane with prisms, which strongly chirps the pulse, making it longer.

5.2.3 Full control

Full control, mixing spatial with temporal control over XUV emission, is what this second part of the outlook is intended for. To reach this point, I believe many incremental improvements will be necessary. Thus, a modular view of the control part fits quite well.

To clarify what I mean, I think the full control calls for two different spatial modulators to shape the intensity profile in the target. One that redirects the XUV emission to the desired direction, and one that redirects the XUV emission out. These "on" and "off" intensity shapes would then complement each other. The third type of control sequence, controlling or shaping the amplitude of the emission, calls for a flat intensity profile and could be realized from the combination of the first two intensity profiles. To control which pulse goes to "on" or "off" shaper, a polarization beam splitter can be used, with a quarter-wave-plate before a reflective SLM in the two arms. The reflected beams go through the polarization beam splitter again, now with flipped polarization, and come out in the fourth direction. This is a module that could be used from the start. As time goes on, more temporal shaping of the control pulses can be added in modules in front of the spatial shaper.

5.3 The road forward

In the distant future, I believe that full control of phase and amplitude of XUV pulses will open the door to the combination of attosecond physics and quantum information. Instead of relying on cryo-cooling to keep the coherence, everything can be done ultrafast[2]. Maybe there will be ultrafast XUV quantum information conferences in 50 years.

In principle, I think that if this is going to succeed such that OOM becomes widely used, the key is in the community. There are so many potential faults and mistakes, what target to use and so on, but with many different people conducting research and working toward a common goal, the chance that solutions will be found is higher. This is as it has always been in research: many individual steps, some greater than others, but never alone. Those that were alone are forgotten[3].

[2]This might even be done with a turn-key laser system, in combination with a small and neat HHG setup.

[3]or called Newton.

Comments on the papers

I **Space-time control of free induction decay in the extreme ultraviolet**
S. Bengtsson*, E. W. Larsen*, D. Kroon, S. Camp, M. Miranda, C. L. Arnold, A. L'Huillier, K. J. Schafer, M. B. Gaarde, L. Rippe, and J. Mauritsson; (*Authors contributed equally).
Nat. Photon. **11**, 252-258 (2017) .
In this paper we demonstrate both spatial and temporal control of XUV emission from a gas. I built major part of the experimental setup, and was the first to observe the effect and I had a major part in planning and conducting the experiments. I also had a major role in analysis and interpretation of the experimental data, and in writing the manuscript.

II **Noncollinear optical gating**
C. M. Heyl, S. N. Bengtsson, S. Carlström, J. Mauritsson, C. L. Arnold and A. L'Huillier.
New J. Phys. **16**, 05201 (2014) .
In this paper we describe the concept how two noncollinear pulses can be used to generate spatially separated, single attosecond pulses through high order harmonic generation (HHG). We support the concept with simulations of the HHG process. In HHG part of a electron tunnels from the atom, follows an excursion in the neighbourhood, and are recombined with the parent ion. An approximation for solving the time-dependent Schrödinger equation is called the strong field approximation (SFA), in which the excursion of the electron is solved classical. This has been demonstrated by others to well recreate the temporal profile of the emission from HHG. I developed a one atom SFA code into a code with multiple atoms,taking macroscopic effects into account and calculating the far-field signal, and with this code I did the SFA simulations confirming the concept in the paper. I prepared some of the figures and participated in the writing of the manuscript.

III **Macroscopic Effects in Noncollinear High-Order Harmonic Generation**

C. M. Heyl, P. Rudawski, F. Brizuela, S. N. Bengtsson, J. Mauritsson and A. L'Huillier.

Phys. Rev. Lett. **112**, 143902 (2014) .

In this paper we study the macroscopic effect when generating harmonics with ω and 2ω, and how phase matching affect the spatial emission of harmonics. Using the code described in paper II, I simulated the emitted field from the HHG process which supports the claim. I prepared some of the figures and participated in the writing of the manuscript.

IV **Gating attosecond pulses in a noncollinear geometry**

M. Louisy, C. L. Arnold, M. Miranda, E. W. Larsen, S. N. Bengtsson, D. Kroon, M. Kotur, D. Guénot, L. Rading, P. Rudawski, F. Brizuela, F. Campi, B. Kim, A. Jarnac, A. Houard, J. Mauritsson, P. Johnsson, A. L'Huillier and C. M. Heyl.

Optica **2**, 563-566 (2015).

In this paper we experimentally show noncollinear optical gating. I did a major part in building the beam line where the experiments were conducted. I commented on the manuscript.

V **Spectral phase measurement of a Fano resonance using tunable attosecond pulses**

M. Kotur, D. Guénot, Á. Jiménez-Galán, D. Kroon, E. W. Larsen, M. Louisy, S. Bengtsson, M. Miranda, J. Mauritsson, C. L. Arnold, S. E. Canton, M. Gisselbrecht, T. Carette, J. M. Dahlström, E. Lindroth, A. Maquet, L. Argenti, F. Martín and A. L'Huillier.

Nat. Commun **7**, 10566 (2016).

In this paper we measured the phase of the photoionization probability amplitude across $3s^2 3p^6 \rightarrow 3s^1 3p^6 4p$ autoionizing resonance in argon by tuning the central wavelength of the laser and measuring the RABBITT trace, which is a method to characterize attosecond pulse trains. I did a major part in building the beam line where the experiment took place. I commented on the manuscript.

VI **Unexpected sensitivity of nitrogen ions superradiant emission on pump laser wavelength and duration**

Y. Liu, P. Ding, N. Ibrakovic, S. Bengtsson, S. Chen, R. Danylo, E. Simpson, E. W. Larsen, A. Houard, J. Mauritsson, A. L'Huillier, C. L. Arnold, S. Zhuang, V. Tikhonchuk and A. Mysyrowicz.

accepted in Phys. Rev. Lett. 14 September 2017.

In this paper we measured the emission of 391 nm from nitrogen as a function of central wavelength of a strongly focused IR laser. This was a european collaboration where the mechanism behind lasing in nitrogen was examined, where both the forward emission and the sideways emission was recorded for different central wavelengths on the laser. I built major part of the experimental setup, participated in the experiments and in the analysis of the experimental results. I commented on the manuscript.

Acknowledgements

There are, as always, a multitude of persons to thank. To start I would like to thank my late father. He wanted to see this book, even though he would not understand very much of it. All the days working together with him in the fruit orchard and the beehives, even though I was quite reluctant in the beginning, is today a big part of who I am. He had a joy when working, a kind of deeper joy stemming from using what you have got and being glad that you can work. This joy, which in the end is a joy in living life, is something that I hope to always have as well. He never really retired, even though he turned 88.

The other most important person is my mother. Thank you for all the warmth that you spread around you. That you care for each and every one that you see. Thank you for being spontaneous, even though it sometimes is slightly too much. I think I am very much like you in that regard. Thank you for all the good food. Thank you for all the love.

Many other people guided me to where I am today. My first math teacher was in some sense Michael, who while we were working in the orchard answered all kinds of weird questions (like "How much is 2^{10}?", which for me as a kid was beyond cool) and opened the amazing world of math. I might not have been the most efficient in picking apples while I tried to figure out the equation fitting the points given. Thank you for taking your time with a small kid with many questions and for being a role model.

I owe a tremendous gratitude to my supervisor Johan for letting me be who I am, even allowing a lot of time and money on the Storm generator among many other things. Thank you for always being generous! Thanks also to my co-supervisor Lars. You did your best to drown me in underwater rugby, but I wish you better luck with Neven. Thanks for all the nice discussions over the years. Thanks to both of you for trying to mix your fields and giving me the opportunity to do the PhD. We did not reach all the way to what we talked about that winter day at the library, where the ultrafast quantum computer was mentioned, but maybe eventually we will get there.

During my time at atomic physics I have met many wonderful people. My greatest gratitude goes to those I worked most with. Esben, without you this thesis would not have been possible. Your characteristic of not letting go of physics problems that you want to understand is something that I look up to. Neven, the second Nesben, thank you for the friendship and talks and that you actually managed to get me to the gym. Emma, that you became a postdoc in our group is absolutely super fab! Thank you for continuously spreading joy and happiness around you, and cheering up people that

are feeling down writing their thesis. Thank you all for the amazing nights together in the lab doing awesome physics!

I need to also especially thank all the people I shared office with. So many nice talks and laughs we shared together. Continue to grow a warm and happy atmosphere in the office and don't forget to water the plants!

Many big hugs go to Gustav and the student dorm Akuten. To just relax and hang around in the kitchen is amazing, when coming home after a long day in the lab or when writing the thesis. You guys are the best!

I can not mention everyone, because then the book would double in size, but you, my friends and family, are all very dear to me and I thank you for all the support.

At last, thanks to God for everything.

References

1. Y. M. Aleksandrov, P. F. Gruzdev, M. G. Kozlov, A. V. Loginov, V. N. Makhov, R. V. Fedorchuk, and M. N. Yakimenko. Oscillator strengths of lines in the 20-80-nm range of the neon absorption spectrum. *Optics and Spectroscopy*, 54:4–7, Jan. 1983.

2. L. Allen and J. H. Eberly. *Optical resonance and two-level atoms*. Dover publications, 1987.

3. F. T. Arecci and R. Bonifacio. Theory of optical maser amplifiers. *IEEE Journal of Quantum Electronics*, QE-1(4):169–178, July 1965.

4. A. R. Beck, D. M. Neumark, and S. R. Leone. Probing ultrafast dynamics with attosecond transient absorption. *Chemical Physics Letters*, 624:119 – 130, 2015.

5. N. Berrah, B. Langer, J. Bozek, T. W. Gorczyca, O. Hemmers, D. W. Lindle, and O. Toader. Angular-distribution parameters and r -matrix calculations of ar. *Journal of Physics B: Atomic, Molecular and Optical Physics*, 29(22):5351, 1996.

6. F. Bloch. Nuclear induction. *Phys. Rev.*, 70:460–474, Oct 1946.

7. R. G. Brewer and R. L. Shoemaker. Optical free induction decay. *Phys. Rev. A*, 6:2001–2007, Dec 1972.

8. W. Cao, E. R. Warrick, A. Fidler, S. R. Leone, and D. M. Neumark. Near-resonant four-wave mixing of attosecond extreme-ultraviolet pulses with near-infrared pulses in neon: Detection of electronic coherences. *Phys. Rev. A*, 94:021802, Aug 2016.

9. C. Cohen-Tannoudji, J. Dupont-Rocand, and G. Grynberg. *Atom-Photon Interactions: Basic Processes and Applications*. Wiley-VCH, 1998.

10. P. B. Corkum. Plasma perspective on strong-field multiphoton ionization. *Phys. Rev. Lett.*, **71**:1994–1997, 1993.

11. R. D. Cowan. *The Theory of Atomic Structure and Spectra*. University of California Press, 1981.

12. S. Croft, J. R. D. McElroy, A. Nicholson, and T. Guzzardo. On the relationship between the natural line width and lifetime of x-ray transitions. In *Proceeding of the 56th Annual Meeting of the Institute of Nuclear Materials Management, 12-16 July 2015, Indian Wells, California, USA.*, 2015.

13. N. B. Delone and V. P. Krainov. Ac stark shift of atomic energy levels. *Physics-Uspekhi*, 42(7):669, 1999.

14. R. H. Dicke. Coherence in spontaneous radiation processes. *Phys. Rev.*, 93:99–110, Jan 1954.

15. U. Fano. Effects of configuration interaction on intensities and phase shifts. *Phys. Rev.*, 124:1866–1878, Dec 1961.

16. M. Ferray, A. L'Huillier, X. F. Li, L. A. Lompre, G. Mainfray, and C. Manus. Multiple-harmonic conversion of 1064 nm radiation in rare gases. *Journal of Physics B: Atomic, Molecular and Optical Physics*, 21(3):L31, 1988.

17. C. Gorter and L. Broer. Negative result of an attempt to observe nuclear magnetic resonance in solids. *Physica*, 9(6):591 – 596, 1942.

18. M. Gross and S. Haroche. Superradiance: An essay on the theory of collective spontaneous emission. *Physics Reports*, 93(5):301 – 396, 1982.

19. E. L. Hahn. Nuclear induction due to free larmor precession. *Phys. Rev.*, 77:297–298, Jan 1950.

20. E. L. Hahn. Spin echoes. *Phys. Rev.*, 80:580–594, Nov 1950.

21. R. C. Hilborn. Einstein coefficients, cross sections, f values, dipole moments, and all that. *American Journal of Physics*, 50(11):982–986, 1982.

22. F. A. Hopf, R. F. Shea, and M. O. Scully. Theory of optical free-induction decay and two-photon superradiance. *Phys. Rev. A*, 7:2105–2110, Jun 1973.

23. F. Könz, Y. Sun, C. W. Thiel, R. L. Cone, R. W. Equall, R. L. Hutcheson, and R. M. Macfarlane. Temperature and concentration dependence of optical dephasing, spectral-hole lifetime, and anisotropic absorption in eu^{3+}: Y_2sio_5. *Phys. Rev. B*, 68:085109, Aug 2003.

24. A. Kramida, Yu. Ralchenko, J. Reader, and and NIST ASD Team. NIST Atomic Spectra Database (ver. 5.3), [Online]. Available: http://physics.nist.gov/asd [2017, October 19]. National Institute of Standards and Technology, Gaithersburg, MD., 2015.

25. E. W. Larsen. *Attosecond Sources and Interferometers - Development and Applications*. PhD thesis, Lund University, 2016.

26. G. M. Lawrence. Radiance lifetimes in the resonance series of ar i. *Phys. Rev.*, 175:40–44, Nov 1968.

27. S. L. McCall and E. L. Hahn. Self-induced transparency by pulsed coherent light. *Phys. Rev. Lett.*, 18:908–911, May 1967.

28. A. McPherson, G. Gibson, H. Jara, U. Johann, T. S. Luk, I. A. McIntyre, K. Boyer, and C. K. Rhodes. Studies of multiphoton production of vacuum-ultraviolet radiation in the rare gases. *J. Opt. Soc. Am. B*, 4(4):595–601, Apr 1987.

29. L. Minnhagen. Spectrum and the energy levels of neutral argon, ar i. *J. Opt. Soc. Am.*, 63(10):1185–1198, Oct 1973.

30. E. M. Purcell, H. C. Torrey, and R. V. Pound. Resonance absorption by nuclear magnetic moments in a solid. *Phys. Rev.*, 69:37–38, Jan 1946.

31. P. Rudawski. *Second-generation High-Order Harmonic Sources*. PhD thesis, Lund University, 2014.

32. U. van Bürck. Coherent pulse propagation through resonant media. *Hyperfine Interactions*, 123(1):483–509, Mar 1999.

33. O. Zatsarinny and K. Bartschat. B -spline calculations of oscillator strengths in neutral argon. *Journal of Physics B: Atomic, Molecular and Optical Physics*, 39(9):2145, 2006.

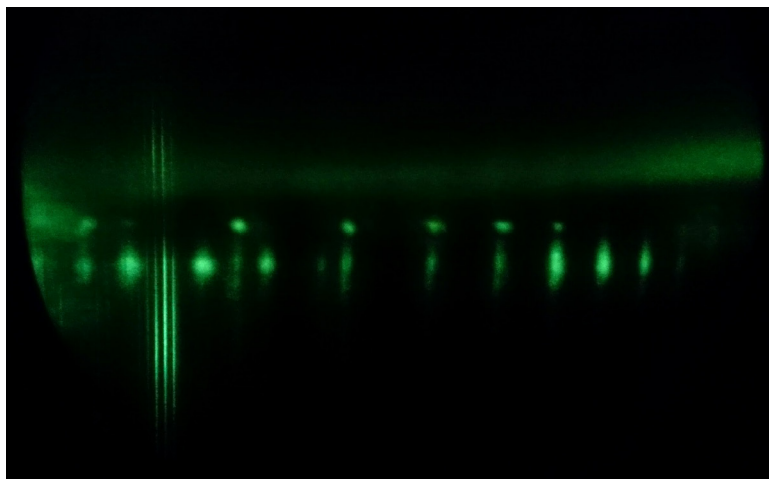

The results in this thesis were all observed on this phosphor screen. So many hours spent staring at this screen.

Printed by Media-Tryck, Lund 2017 NORDIC ECOLABEL, 3041 0903

LUND UNIVERSITY
Faculty of Engineering, LTH
Department of Physics
Division of Atomic Physics

ISBN: 978-91-7753-491-4 (print)
ISBN: 978-91-7753-492-1 (pdf)
ISSN 0281-2762
Lund Reports on Atomic Physics, LRAP 540 (2017)